



**Politecnico
di Torino**



**von KARMAN INSTITUTE
FOR FLUID DYNAMICS**

Master of Science in Aerospace Engineering

Mechanical and Aerospace Engineering department
Aero-gas dynamics

Master's Thesis: Development of Thermal Wall Functions through Direct Numerical Simulation

Von Karman Institute

Supervisors:

Dr. Lilla Koloszar

Dr. Jure Oder

Politecnico di Torino

Supervisors:

Prof. Gioacchino Cafiero

Prof. Sandra Pieraccini

Candidate:

Ioana Gocea

April 2025

Acknowledgments

I would like to begin by expressing my deepest gratitude to my supervisors. A special thank you to Jure Oder, whose patience in guiding me through an entirely new topic, coupled with his vast knowledge and insightful advice, made what initially seemed like a complex and intricate research area feel like an intriguing and playful challenge. I would also like to extend my thanks to Lilla Koloszar for providing her expertise and invaluable insights, and to my supervisors at Politecnico di Torino for their involvement.

I am thankful to my parents, whose support has been the foundation of all my accomplishments. To my sister, whose ambitious spirit surpasses even my own will (and for keeping me on my toes!), and to my brother, for constantly reminding me of the difficulty of reaching that 9th engineer position in his hypothetical company — you really brought a whole new level of humor to this journey!

A heartfelt thank you to all my friends. To those who always endured my loudness and laughter through the years, to those who started this journey with me, to the ones I played briscola with every morning on the train, to the friends I made on the other side of the world, and to my friends at VKI — thank you for being the amazing people you are.

A special thank you to Lorenzo, for always patiently handling my overthinking and stubbornness, to the Gruppo Pino, for sharing in my wildest ideas, to that bunch of falsinei for the infinite nights playing board games, and to all the *pnuts* that made my stay in Belgium an incredible one.

Abstract

This study performs a direct numerical simulation (DNS) of a turbulent boundary layer that develops spatially on a flat plate under a zero pressure gradient. The investigation focuses on the influence of Prandtl numbers on passive scalar transport. The Navier-Stokes equations and scalar transport equations are solved using a spectral element method (SEM). Various molecular Prandtl numbers are analyzed, mainly in the liquid metals range, to observe their impact on scalar behavior, particularly in the outer region of the boundary layer. The results reveal significant insights into the statistical behavior of scalars, highlighting differences in near-wall streak spacing and coherence between velocity and scalar fields based on Prandtl number variations. Probabilistic methods further identify intermittency near the wall and in the outer region, providing a comprehensive view of the scalar-field dynamics influenced by Prandtl numbers.

Contents

Abstract	ii
List of Figures	x
List of Tables	xi
List of Symbols	xii
1 Introduction	1
1.1 Accelerator Driven Systems (ADS)	1
1.2 Overview of the MYRRHA Reactor	1
1.2.1 Liquid Metal Coolants	2
1.3 Supporting the design and certification process through numerical modeling	5
2 Literature Review	6
2.1 Historical milestones in Turbulence Research	6
2.1.1 Visualization of Laminar to Turbulent Flow Transition: Osborne Reynolds	6
2.1.2 Boundary layer theory	7
2.1.3 The Meandering of Cigarette Smoke	7
2.1.4 Experimental Approach in Turbulence Research	8
2.1.5 Computational Approach in Turbulence Research	8
2.2 DNS of a Turbulent Boundary Layer	10
2.2.1 Main Challenges	10
3 Theoretical Formulation	12
3.1 Governing Equations	12
3.1.1 Velocity Field	12
3.1.2 Scalar Field	15
3.2 Turbulent Boundary Layer	18
3.3 Equations	18
3.3.1 Scalings	19
4 Direct Numerical Simulation	24
4.1 Non-Dimensional Form of the Navier-Stokes and Scalar Transport Equations	24
4.2 Boundary Conditions	25

4.2.1	Boundary Conditions for Flow Field	25
4.2.2	Boundary Conditions for Scalar Field	27
4.3	Computational Domain	28
4.4	Numerical Method	30
4.4.1	Numerical scheme	30
4.4.2	Random Volumetric Force	31
5	Results	33
5.1	Flow Field	35
5.1.1	Kolmogorov Length Scale	35
5.1.2	Boundary Layer Thickness	37
5.1.3	Outer Layer	39
5.1.4	Inner Layer	41
5.1.5	Skin Friction	44
5.1.6	Probability Density Function	45
5.1.7	Energy Spectrum of Turbulence	49
5.1.8	Reynolds Stress Anisotropy	50
5.2	Scalar Field	52
5.2.1	Boundary Layer Thickness	52
5.2.2	Inner Layer	56
5.2.3	Turbulent Prandtl Number	64
5.2.4	Stanton Number	67
5.2.5	Probability Density Function	69
5.3	Comparative Analysis of Velocity and Scalar Fields	73
5.3.1	Energy Spectrum	73
5.3.2	Joint Probability Density Function	75
5.4	Visualization of Instantaneous Fields	77
5.4.1	Plane x-z	77
5.4.2	Plane x-y	79
6	Conclusion	84
A	Accelerator Driven System	86
A.1	Main Process	86
A.1.1	Advantages of ADS	87
A.1.2	Materials and Configurations	88
B	Liquid Metals in Nuclear Reactors	89
B.1	Lithium	89
B.2	Mercury	89
B.3	Sodium	90
B.4	Sodium-Potassium Alloy (Na-K)	90
B.5	Lead	90
B.6	Lead-Bismuth Eutectic (LBE)	91
B.7	Galinstan	91
C	Additional Proofs and Demonstrations	92
C.1	Efficiency of Power-of-Two Polynomials in SEM	92

Bibliography

100

List of Figures

1.1	3-D Schematic view of the MYRRHA sub-critical reactor(Ait Abderahim [1])	2
2.1	Original sketch from Reynolds [6] where <i>the mass of colour resolved itself into a mass of more or less distinct curls, showing eddies.</i>	6
2.2	Original sketch from Prandtl [7] that shows <i>flow separation in a boundary layer.</i>	7
2.3	Original Photo from Libby [8] <i>Free convection from a cigarette.</i>	8
4.1	<i>Illustration of the time-dependent components of the tripping function. The resulting function has a continuous time derivative</i> Massaro et al. [52]	31
5.1	Mean velocity components over time, where each component is integrated over the entire volume and normalized by the volume itself. . . .	34
5.2	Dissipation rate of turbulent kinetic energy	34
5.3	Variation of the free-stream velocity U_∞ and β with downstream positions.	35
5.4	Kolmogorov length scale divided by the mesh size in the entire domain. Note: the value is above η only in the region where the influence of the tripping force is high and within the boundary layer.	36
5.5	Resolution check: Wall-normal resolution Δy^+ , Kolmogorov length scale η^+ in the simulation and from Li et al. [28]. Note: Δy and η are divided by $\frac{u_\tau}{\nu}$ to make the variables dimensionless	37
5.6	Displacement thickness and momentum thickness, measures of the boundary layer thickness versus the downstream positions.	38
5.7	Reynolds number based on displacement Re_{δ^*} and momentum thickness Re_θ versus Reynolds number based on downstream positions Re_x	39
5.8	Variation of the shape factor with the downstream positions.	39
5.9	Mean streamwise velocity profile at different downstream positions in outer scaling.	40
5.10	RMS values of the velocity, pressure fluctuations and Reynolds shear stress versus downstream positions in outer scaling.	41
5.11	Mean streamwise velocity profile at different downstream positions in outer scaling.	42
5.12	Mean streamwise velocity profile at different downstream positions in outer scaling.	42
5.13	RMS values of the velocity, pressure fluctuations and Reynolds shear stress versus downstream positions in inner scaling.	43

5.14	Skin friction coefficient c_f versus the Reynolds number based on the momentum thickness Re_θ	44
5.15	PDF of u' at different y^+ position: (a) $y^+ = 1.57$ $S(u') = 1.01$, (b) $y^+ = 4.86$ $S(u') = 0.58$, (c) $y^+ = 9.72$ $S(u') = 0.15$, (d) $y^+ = 30.2$ $S(u') = -0.50$, (e) $y^+ = 48.5$ $S(u') = -0.86$, (f) $y^+ = 95.3$ $S(u') = -1.98$	46
5.16	PDF of v' at different y^+ position: (a) $y^+ = 1.57$ $S(v') = -0.25$, (b) $y^+ = 4.86$ $S(v') = -0.32$, (c) $y^+ = 9.72$ $S(v') = -0.34$, (d) $y^+ = 30.2$ $S(v') = 0.31$, (e) $y^+ = 48.5$ $S(v') = 0.62$, (f) $y^+ = 95.3$ $S(v') = 0.43$	47
5.17	PDF of w' at different y^+ position: (a) $y^+ = 1.57$ $S(w') = -0.16$, (b) $y^+ = 4.86$ $S(w') = -0.077$, (c) $y^+ = 9.72$ $S(w') = -0.071$, (d) $y^+ = 30.2$ $S(w') = -0.03$, (e) $y^+ = 48.5$ $S(w') = 0.17$, (f) $y^+ = 95.3$ $S(w') = -0.08$	48
5.18	Energy spectra for two spanwise positions at $Re_\theta = 396$ and (a) $y^+ = 2.5$ (b) $y^+ = 154.5$	49
5.19	Comparison of energy spectra for at $Re_\theta = 308$, $Re_\theta = 351$ and $Re_\theta = 396$ for $y^+ = 154.5$	50
5.20	Anisotropy invariant map at $Re_\theta = 596$ against wall normal position y^+	51
5.21	Comparison of boundary layer thickness for different scalars at $Re_\theta = 596$ (a) Displacement thickness δ_θ^* (b) Momentum thickness θ_θ	53
5.22	Different measures of the scalar boundary layer thickness versus the downstream positions for (a) $Pr = 1$, (b) $Pr = 0.71$, (c) $Pr = 0.30$, (d) $Pr = 0.20$, (e) $Pr = 0.0237$, (f) $Pr = 0.0232$ with isothermal boundary conditions.	54
5.23	Different measures of the scalar boundary layer thickness versus the downstream positions for (a) $Pr = 1$, (b) $Pr = 0.71$, (c) $Pr = 0.30$, (d) $Pr = 0.20$, (e) $Pr = 0.0237$, (f) $Pr = 0.0232$ with isoflux boundary conditions.	55
5.24	Comparison of mean scalar profile for various Prandtl numbers at $Re_\theta = 596$	56
5.25	Mean scalar profiles at different downstream positions for (a) $Pr = 1$, (b) $Pr = 0.30$, (c) $Pr = 0.20$, (d) $Pr = 0.0232$ with isothermal wall-boundary conditions.	57
5.26	Comparison of scalars with different wall-boundary conditions, highlighting the behavior at the wall.	58
5.27	RMS values of the scalar fluctuation at different downstream positions for (a) $Pr = 1$, (b) 0.71 , (c) $Pr = 0.30$, (d) $Pr = 0.20$, (e) $Pr = 0.0237$, (f) $Pr = 0.0232$ with isothermal wall-boundary conditions.	59
5.28	RMS values of the scalar fluctuation at different downstream positions for (a) $Pr = 1$, (b) 0.71 , (c) $Pr = 0.30$, (d) $Pr = 0.20$, (e) $Pr = 0.0237$, (f) $Pr = 0.0232$ with isoflux wall-boundary conditions.	60
5.29	Comparison of streamwise scalar flux at $Re_\theta = 596$ for various Prandtl numbers.	61
5.30	Streamwise scalar flux fluctuations at different downstream positions for (a) $Pr = 1$, (b) 0.71 , (c) $Pr = 0.30$, (d) $Pr = 0.20$, with isothermal wall-boundary conditions.	62

5.31	Wall-normal scalar flux fluctuations at different downstream positions for (a) $Pr = 1$, (b) 0.30, (c) $Pr = 0.20$, (d) $Pr = 0.0237$, with isothermal wall-boundary conditions.	63
5.32	Streamwise scalar flux fluctuations at different downstream positions for (a) $Pr = 1$, (b) 0.20 with isoflux wall-boundary conditions.	63
5.33	Wall-normal scalar flux fluctuations at different downstream positions for (a) $Pr = 1$, (b) 0.71, (c) $Pr = 0.30$, (d) $Pr = 0.20$, (e) $Pr = 0.0237$, (f) $Pr = 0.0232$ with isoflux wall-boundary conditions.	64
5.34	Comparison of turbulent Pr with different wall-boundary conditions at $Re_\theta = 596$ for (a) $Pr = 1$ and $Pr = 0.71$, (b) $Pr = 1$ and $Pr = 0.0232$ (LBE).	66
5.35	Low Pr effect at $Re_\theta = 596$ depending on the wall-boundary conditions.	66
5.36	Turbulent Pr with different wall-boundary conditions at $Re_\theta = 596$ for a wide range of Prandtl number.	66
5.37	Reynolds Analogy: Stanton number for both isothermal and isoflux wall-boundary conditions at $Pr = 1$ and friction coefficient C_f	67
5.38	Comparison with the data from Li et al. [28] of Stanton number for (a) $Pr = 0.71$ (b) $Pr = 0.2$	68
5.39	Stanton Number at different downstream position for $pr = 0.0232$ (LBE).	69
5.40	PDF of θ' at $y^+ \approx 1.57$ with isoflux wall-boundary condition of the following Prandtl numbers and respective skewness of the distribution: (a) $Pr = 1$, (b) $Pr = 0.71$, (c) $Pr = 0.5$, (d) $Pr = 0.3$	70
5.41	PDF of θ' at $y^+ \approx 1.57$ with isoflux wall-boundary condition of the following Prandtl numbers and respective skewness of the distribution: (a) $Pr = 0.2$, (b) $Pr = 0.0237$, (c) $Pr = 0.0232$, (d) $Pr = 0.0058$	71
5.42	PDF of θ' at $y^+ \approx 1.57$ with isoscalar wall-boundary condition of the following Prandtl numbers and respective skewness of the distribution: (a) $Pr = 0.0232$, (b) $Pr = 0.0058$	71
5.43	PDF of θ' at $y^+ \approx 1.57$ with isoscalar wall-boundary condition of the following Prandtl numbers and respective skewness of the distribution: (a) $Pr = 1$, (b) $Pr = 0.71$, (c) $Pr = 0.5$, (d) $Pr = 0.3$, (e) $Pr = 0.2$, (f) $Pr = 0.0237$	72
5.44	Comparison of energy spectra of flow and scalar fields at $y^+ \approx 2.5$ with isotehrmal wall-boundary condition of the following Prandtl numbers: (a) $Pr = 1$, (b) $Pr = 0.2$, (c) $Pr = 0.0232$	73
5.45	Comparison of energy spectra of flow and scalar fields with isotehrmal wall-boundary condition of the following Prandtl numbers and wall normal position: (a) $Pr = 1$ $y^+ = 22.8$, (b) $Pr = 0.2$ $y^+ = 22.8$, (c) $Pr = 0.0232$ $y^+ = 22.8$ (d) $Pr = 1$ $y^+ = 154.5$, (e) $Pr = 0.2$ $y^+ = 154.5$, (f) $Pr = 0.0232$ $y^+ = 154.5$	74
5.46	JPDF of (u', θ') with isoflux wall-boundary conditions of the following Prandtl numbers: (a) $Pr = 1$, (b) $Pr = 0.0232$	75
5.47	JPDF of (u', θ') with isoscalar wall/boundary condition of the following Prandtl numbers: (a) $Pr = 2$, (b) $Pr = 1$, (c) $Pr = 0.71$, (d) $Pr = 0.5$, (e) $Pr = 0.2$, (f) $Pr = 0.0232$	76

5.48	Instantaneous contour plot of the fluctuating scalar fields, with isothermal boundary condition at the wall, in the x—z plane at $y^+ = 1.57$, starting from $Re_\theta = 175$ to $Re_\theta = 596$. The plots are in order of the following Prandtl numbers: (a) $Pr = 1$, (b) $Pr = 0.71$, (c) $Pr = 0.3$, (d) $Pr = 0.2$, (e) $Pr = 0.0232$, (f) $Pr = 0.0058$	78
5.49	Instantaneous contour plot of the flow fields in the x—z plane for $y^+ = 1.57$, starting from $Re_\theta = 175$ to $Re_\theta = 596$	79
5.50	Instantaneous contour plot of the fluctuating scalar fields, with isoflux boundary condition at the wall, in the x—z plane at $y^+ = 1.57$, starting from $Re_\theta = 175$ to $Re_\theta = 596$. The plots are in order of the following Prandtl numbers: (a) $Pr = 1$, (b) $Pr = 0.71$, (c) $Pr = 0.3$, (d) $Pr = 0.2$, (e) $Pr = 0.0232$, (f) $Pr = 0.0058$	80
5.51	Instantaneous contour plot of the fluctuating scalar fields, with isothermal boundary condition at the wall, in a x—y plane, starting from $Re_\theta = 175$ to $Re_\theta = 596$. The plots are in order of the following Prandtl numbers: (a) $Pr = 1$, (b) $Pr = 0.71$, (c) $Pr = 0.3$, (d) $Pr = 0.2$, (e) $Pr = 0.0232$, (f) $Pr = 0.0058$	81
5.52	Instantaneous contour plot of the flow field in a x—y plane, starting from $Re_\theta = 175$ to $Re_\theta = 596$	82
5.53	Instantaneous contour plot of the fluctuating scalar fields, with isoflux boundary condition at the wall, in a x—y plane, starting from $Re_\theta = 175$ to $Re_\theta = 596$. The plots are in order of the following Prandtl numbers: (a) $Pr = 1$, (b) $Pr = 0.71$, (c) $Pr = 0.3$, (d) $Pr = 0.2$, (e) $Pr = 0.0232$, (f) $Pr = 0.0058$	83
6.1	Turbulent Pr with isothermal wall-boundary conditions at $Re_\theta = 596$ across a wide range of Prandtl numbers: (a) logarithmic scale, (b) linear scale	85
A.1	Schematics of a two-stage spallation reaction from Gnanasekaran [3]	87

List of Tables

1.1	Passive scalars and respective Prandlt numbers in the simulation	4
1.2	Thermal properties of liquid metals	4
4.1	Reynolds numbers with respect to the downstream location x	29
4.2	Parameters set in the simulation	32

List of Symbols

u	Streamwise velocity component
v	Wall-normal velocity component
w	Spanwise velocity component
u_τ	Friction velocity
U_∞	Free-stream velocity
T	Temperature
T_w	Wall temperature
T_∞	Free-stream temperature
Pr	Prandtl number
Pr_t	Turbulent Prandtl number
Pe	Péclet number = $Re \cdot Pr$
Re	Reynolds number
Re_τ	Friction Reynolds number
Re_{δ_0}	Reynolds number based on the inlet displacement thickness δ_0
Re_θ	Reynolds number based on the momentum thickness θ
St	Stanton number
k	Turbulent kinetic energy
c_p	Specific scalar capacity
H_{12}	Shape factor
k	Scalar conductivity
p	Pressure
q_w	Rate of scalar transfer from the wall to the flow
t	Time
x_i, x, y, z	Cartesian coordinates
y_L	Height of the domain
P_{ij}	Production of turbulent stress
Π_{ij}	Redistribution of turbulent kinetic energy
D_{ij}	Spatial transport of turbulent stress by diffusion
ε_{ij}	Dissipation term of turbulent kinetic energy
P_k	Production of turbulent energy
Π_k	Pressure diffusion term
D_k	Turbulent and viscous diffusion
ε_k	True viscous dissipation term
$P_{\theta i}$	Production term of scalar transport
$\Pi_{\theta i}$	Pressure scalar-gradient correlation term
$D_{\theta i}$	Turbulent and molecular diffusion term
$\varepsilon_{\theta i}$	Dissipation term of scalar transport
U_i	Blasius laminar base flow

Greek Symbols

α	Thermal diffusivity
α_t	Eddy diffusivity
γ	Specific heat ratio
δ	Boundary layer thickness
δ^*	Displacement thickness
δ_0^*	Inlet displacement thickness
δ_{99}	99 local scalar boundary-layer thickness
δ^θ	Momentum thickness
ν	Kinematic viscosity
ν_t	Turbulent eddy viscosity
ρ	Density
τ_w	Wall shear stress
ϵ	Turbulent dissipation rate
θ	Passive scalar concentration
θ_i	Passive scalar i
θ_s	Friction scalar
θ_w	Wall scalar concentration
θ_∞	Free-stream scalar concentration
κ	von Kármán constant
κ_h	von Kármán constant for the scalar

Subscripts

f	Properties of the fluid
w	Properties at the wall
∞	Properties in the free-stream
rms	Root-mean-square value of the quantity

Superscripts

*	Dimensional term for the variable quantity
$\bar{\cdot}$	Reynolds-averaged quantity
$\langle \cdot \rangle$	Time-averaged quantity
'	Fluctuating part
+	Scaling in viscous (wall) units
out	Scaling in outer units

Abbreviations

<i>RANS</i>	Reynolds/Averaged Navier-Stokes
<i>LES</i>	Large-Eddy simulation
<i>DNS</i>	Direct Numerical simulation
<i>PDF</i>	Probability Density Function
<i>JPDF</i>	Joint Probability Density Function

Chapter 1

Introduction

1.1 Accelerator Driven Systems (ADS)

Accelerator Driven Systems (ADS) represent a cutting-edge approach in nuclear technology, combining a subcritical nuclear reactor with a high-power particle accelerator. This innovative design aims to enhance the safety and efficiency of nuclear reactors while addressing some of the key challenges associated with traditional nuclear power.

In an ADS, a particle accelerator generates a high-energy proton beam that is directed at a heavy metal target, typically lead or lead-bismuth eutectic (LBE). This interaction produces a large number of neutrons through a process called spallation. These neutrons then sustain the nuclear fission reactions within the subcritical reactor core. Unlike conventional reactors, which rely on a critical mass of fissile material to maintain a self-sustaining chain reaction, an ADS operates in a subcritical state. This means that the reactor cannot sustain the fission process without the continuous input of neutrons from the accelerator. As a result, the reactor can be easily and safely shut down by simply turning off the accelerator. For detailed explanation, see [Appendix A](#).

1.2 Overview of the MYRRHA Reactor

The MYRRHA (Multi-purpose Hybrid Research Reactor for High-tech Applications) project is a groundbreaking initiative in nuclear technology. It is the world's first large-scale Accelerator Driven System (ADS), integrating a subcritical nuclear reactor with a high-power linear accelerator. Located at the SCK CEN site in Mol, Belgium, MYRRHA aims to tackle several critical challenges in nuclear research and waste management.

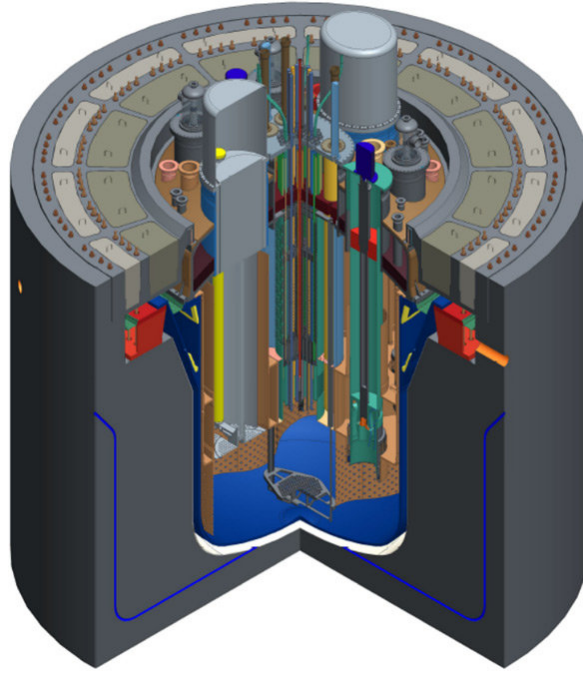


Figure 1.1: 3-D Schematic view of the MYRRHA sub-critical reactor(Ait Abderrahim [1])

MYRRHA's primary objective is to demonstrate the feasibility of ADS technology for transmuting long-lived radioactive waste into shorter-lived isotopes, thereby reducing the long-term radiotoxicity and volume of nuclear waste. The reactor is cooled by lead-bismuth eutectic (LBE) and operates with a maximum thermal power output of $100MW_{th}$. The project is being implemented in three phases, with the first phase focusing on the construction of the initial section of the linear accelerator and the Proton Target Facility (see Baeten et al. [2]).

In addition to waste transmutation, MYRRHA offers significant research opportunities in fundamental and applied physics, and materials science. The reactor will also support fusion reactor research through its dedicated fusion neutron channel.

Overall, MYRRHA represents a significant step forward in the development of sustainable and safe nuclear technologies.

1.2.1 Liquid Metal Coolants

A significant aspect of Gen IV fast nuclear reactors, such as the MYRRHA reactor, is the use of liquid metal coolants. These coolants are chosen for their excellent thermal conductivity, high boiling points at normal pressure, and low neutron absorption cross-sections. These properties make them ideal for maintaining efficient heat transfer and ensuring the reactor operates safely under both normal and emergency conditions.

Applications

Liquid metal coolants, such as LBE, offer high thermal conductivity for efficient heat transfer and serve as excellent radiation shields. They are used in various nuclear reactor systems, including fast breeder reactors and accelerator-driven systems, due to

their wide operating temperature range and ability to block gamma radiation while being transparent to neutrons.

However, LBE is not the only or main coolant used. Other metals like sodium, lithium, and NaK alloy are also employed in various nuclear reactor systems. For further explanation, see Appendix B.

Prandtl Number Range

Liquid metals are characterized by high thermal conductivity and low viscosity, which results in a low Prandtl number. The **Prandtl number (Pr)** is a dimensionless number that characterizes the relative thickness of the momentum and thermal boundary layers in a fluid. It is defined as the ratio of momentum diffusivity (kinematic viscosity) to thermal diffusivity, and is given by the formula:

$$\text{Pr} = \frac{\nu}{\alpha}$$

where:

- ν is the kinematic viscosity
- α is the thermal diffusivity

For liquid metals, the Prandtl number is typically very low, resulting in a thicker thermal boundary layer relative to the momentum boundary layer, indicating that thermal diffusivity is much greater than momentum diffusivity, which is beneficial for efficient heat transfer. The high thermal conductivity of liquid metals ensures rapid heat dissipation, reducing the risk of overheating, and improving the overall safety and performance of systems.

To achieve a comprehensive range of Prandtl numbers applicable to liquid metals, 30 temperature fields were introduced and treated as passive scalars. These fields were duplicated for two separate boundary conditions at the wall, isothermal and isoflux. Some of the scalars were introduced to compare the results with literature and in this way validate the results, while some are introduced due to lack of data in the literature. Some Prandtl numbers were added to complete the range while a dense set of scalar values was chosen within the range $Pr = 0.25 - 0.35$ to closely examine and verify the expected change in behavior within this range (see 1.1).

*Note: Data are taken from Gnanasekaran [3]

Scalar	Prandtl Number	Reason
S_0	2.0	Comparison
S_1	1.0	Range completion
S_2	0.71	Comparison
S_3	0.50	Range completion
S_4	0.35	Range completion
S_5	0.30	Range completion
S_6	0.25	Range completion
S_7	0.20	Comparison
S_8	0.10	Range completion
S_9	0.0413	Lithium
S_{10}	0.0237	Lead (at M.P.)
S_{11}	0.0232	LBE Alloy
S_{12}	0.0210	Galinstan
S_{13}	0.0107	Mercury
S_{14}	0.0085	Na-K Alloy
S_{15}	0.0058	Sodium

Table 1.1: Passive scalars and respective Prandtl numbers in the simulation

Liquid Metal	Thermal conductivity [W/mK]	Melting point [$^{\circ}C$]	Boiling point [$^{\circ}C$]
Lithium	48.6	180.5	1342
Mercury	11.69	-38.9	629.7
Sodium	77.1	97.8	883
Na-K Alloy	25.5	/	784
Lead	15.83	327.4	1749
LBE alloy	12.7	125.5	1638
Galinstan	16.5	-19	1300

Table 1.2: Thermal properties of liquid metals

1.3 Supporting the design and certification process through numerical modeling

The certification process for nuclear reactors is rigorous and multifaceted, ensuring that all safety and operational standards are met before a reactor can be commissioned. This process typically involves several stages, each designed to verify and validate the reactor's performance under various conditions. A critical aspect of this verification is the application of fluid dynamics principles to optimize coolant flow within the reactor.

Experimental Validation: Initial tests are conducted on small-scale models and prototypes to gather empirical data on the reactor's behavior. These experiments use techniques such as Particle Image Velocimetry (PIV) and Laser Doppler Anemometry (LDA) to measure flow velocities and turbulence characteristics (see Richard W. Johnson et al. [4]). These methods provide detailed insights into the flow patterns and heat transfer mechanisms within the reactor, helping to identify potential issues and validate theoretical models.

Computational Fluid Dynamics (CFD) Simulations: Advanced simulations are performed to analyze fluid flow and heat transfer within the reactor. Techniques such as Reynolds-Averaged Navier-Stokes (RANS), Large Eddy Simulation (LES), and Direct Numerical Simulation (DNS) are crucial for modeling complex physical phenomena and predicting the reactor's performance under different scenarios. RANS is used for its computational efficiency in modeling turbulent flows by averaging the effects of turbulence. LES provides a more detailed approach by resolving larger turbulent structures while modeling smaller scales. DNS offers the highest fidelity by resolving all scales of turbulence, providing detailed insights into fluid dynamics and heat transfer, albeit at a high computational cost. Sensitivity studies are conducted to assess the impact of key assumptions, such as turbulence models and grid size, on the predictions. Validation involves using properly instrumented experiments to determine whether the model selections are appropriate for the problem under consideration (see Boyd [5]). Additionally, practices and procedures are established to ensure accurate simulations, including code verification, reduction of numerical error, and quantification of numerical uncertainty (see Richard W. Johnson et al. [4]).

This simulation aims to improve the design and certification process by using DNS to generate data for refining velocity and thermal turbulence models. These models will then be applied in RANS simulations to aid in reactor design and the licensing process. Due to high computational requirements, DNS itself is unlikely to be applied to a full reactor or a particular subsystem directly.

Chapter 2

Literature Review

Turbulence, a cornerstone of fluid dynamics, remains one of the most challenging phenomena within classical physics problems. Despite its ubiquitous presence in systems ranging from planetary boundary layers to the swirling currents in rivers, it continues to elude complete understanding. The transition from laminar to turbulent flow, marked by chaotic and irregular motion, is not just a theoretical curiosity but a critical aspect of many engineering and natural systems. This intricate interplay of scales and forces drives ongoing research and innovation in the field.

2.1 Historical milestones in Turbulence Research

2.1.1 Visualization of Laminar to Turbulent Flow Transition: Osborne Reynolds

One of the most iconic experiments in fluid dynamics is Osborne Reynolds' 1883 study on the transition from laminar to turbulent flow. Reynolds used a glass tube filled with water and injected a stream of dye to visualize the flow. At low flow rates, the dye moved in a straight line, indicating laminar flow. As the flow rate increased, the dye began to mix with the water, signifying the onset of turbulence. This experiment led Reynolds to introduce the dimensionless Reynolds number, defined as

$$Re = \frac{UL}{\nu}$$

where U is the velocity scale, L is the characteristic length, and ν is the kinematic viscosity. The Reynolds number quantifies the ratio of inertial forces to viscous forces and predicts the transition to turbulence when it exceeds a critical value (see Reynolds [6]).



Figure 2.1: Original sketch from Reynolds [6] where *the mass of colour resolved itself into a mass of more or less distinct curls, showing eddies.*

2.1.2 Boundary layer theory

Prandtl introduced the concept of the boundary layer, a thin region near a solid surface where viscous forces are prominent. This theory addressed the shortcomings of potential flow theory, which could not accurately predict drag on objects. Prandtl's boundary layer theory (see Prandtl [7]) separates the flow into two distinct regions: an outer region where viscous effects are minimal and potential flow is assumed, and an inner boundary layer where viscous forces are significant. This differentiation enabled more precise predictions of drag and flow separation, as Prandtl stated " *The physical processes in the boundary layer between fluid and solid body can be calculated in a sufficiently satisfactory way*" ¹.

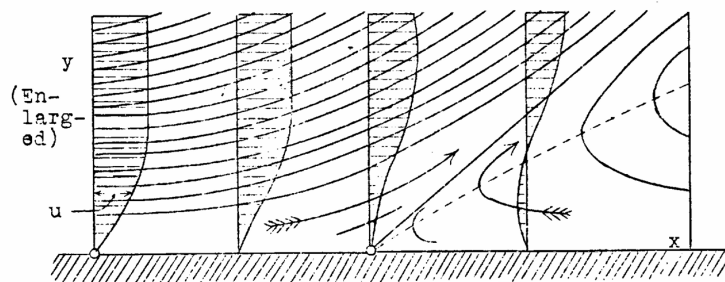


Figure 2.2: Original sketch from Prandtl [7] that shows *flow separation in a boundary layer*.

2.1.3 The Meandering of Cigarette Smoke

A passive scalar is a scalar quantity that does not actively influence the flow dynamics but is carried along by the fluid motion. These scalars, such as smoke or pollutants, are present in low concentrations and have a negligible effect on the fluid's thermophysical properties. They are used to model the propagation of substances like smoke within a fluid flow. One classic experiment that visualizes both turbulence and the behavior of passive scalars is the meandering of cigarette smoke (2.3), where cigarette smoke is released into the air, initially forming a smooth, laminar stream. As it rises, the smoke transitions into chaotic, turbulent motion, demonstrating how passive scalars are dispersed and mixed within turbulent flows. This visualization provides valuable insights into the complex dynamics of scalar transport and helps to understand the intricate behavior of passive scalars in turbulent environments (see Libby [8]).

¹L. Prandtl, 1904 " *Die physikalischen Vorgänge in der Grenzschicht zwischen Flüssigkeit und festem Körper können in genügend befriedigender Weise berechnet werden*"



Figure 2.3: Original Photo from Libby [8] *Free convection from a cigarette.*

2.1.4 Experimental Approach in Turbulence Research

Wind tunnel experiments are the starting point of study of passive scalar dispersion in turbulent flows. Early research on heat transfer was conducted by Tavoularis and Corrsin [9] and Warhaft and Lumley [10]. Later on Hishida and Nagano [11] explored turbulence transport mechanisms in fully developed pipe flow. Zhu and Antonia [12] examined temperature dissipation in turbulent channel flow, while Mosyak, Pogrebnyak, and Hetsroni [13] studied wall temperature fluctuations and thermal coherent structures.

For turbulent boundary layers, Hoffmann and Perry [14] investigated the similarity between Reynolds shear stress ($u'v'$) and scalar flux ($v'\theta'$). Iritani, Kasagi, and Hirata [15] analyzed the relationship between coherent structures and temperature fluctuations near the wall. Anselmet, Djeridi, and Fulachier [16] studied the statistical relationship between a passive scalar and its dissipation.

Experimental data still play a crucial role in validating DNS results and turbulence models.

2.1.5 Computational Approach in Turbulence Research

Direct Numerical Simulation (DNS) has become a pivotal method in turbulence research, providing detailed insights into fluid dynamics without relying on turbulence models. This technique captures all scales of turbulence by solving the Navier-Stokes equations directly. With the advancement in computational power, DNS is no longer limited by large Reynolds numbers. However, resolving the Kolmogorov viscous scales, which encompass all relevant flow structures, still requires computational resources

proportional to $R^{9/4}$ (Tiselj, Flageul, and Oder [17]).

Along with the limitations imposed by the Reynolds number, there is also a constraint based on the Prandtl number (Pr). As Pr increases, the smallest scales in scalar fluctuations decrease, making DNS more challenging. This smallest scale, known as the Obukhov-Corrsin scale, is given by $\eta_{\text{thermal}} = \eta \cdot Pr^{-3/4}$, where η is the Kolmogorov length scale (see 5.1.1). Consequently, higher Pr values result in smaller η_{thermal} , requiring finer resolution in simulations to accurately capture these fluctuations (Sagaut [18]).

Most simulations are conducted with $Pr \leq 2$. Exceptions are Kawamura et al. [19] performing DNS in periodic channel flow for Pr ranging from 0.025 to 5.0 and Na and Hanratty [20] conducting a channel flow DNS reaching $Pr = 10$.

Early DNS studies laid the groundwork for understanding turbulent flows. Rogers, Moin, and Reynolds [21] conducted one of the first DNS in homogeneous shear flow, while Kim and Moin [22] explored channel flows with various Prandtl numbers. Lyons and Hanratty [23] and Kasagi, Tomita, and Kuroda [24] extended these studies to different Reynolds and Prandtl numbers, revealing critical insights into turbulence behavior.

In more complex scenarios, keeping Pr values of 0.71 and 0.025, for instance, Abe, Kawamura, and Matsuo [25] performed DNS at higher Reynolds numbers, up to $Re_{\tau} = 1024$, Chung and Sung [26] investigated turbulent concentric annular pipe flow at $Re_{Dh} = 8900$, highlighting the challenges of simulating high Prandtl number flows.

Most DNS studies have focused on fully developed turbulent channel flows due to their simple geometry and ability to reveal convective heat transfer mechanisms. However, fewer studies have addressed thermal turbulent boundary layers. Bell and Ferziger were pioneers in this area, and later, Kong, Choi, and Lee [27] conducted DNS of thermal boundary layers at $Re_{\theta} = 300$ with $Pr = 0.71$.

Recent Direct Numerical Simulations (DNS) have explored a variety of complex geometries and conditions, leveraging increased computational power. Li et al. [28] conducted DNS of passive scalars in a spatially developing turbulent boundary layer, examining the effects of different Prandtl numbers and wall boundary conditions. Abe [29] performed DNS at high Reynolds numbers, focusing on the interaction between turbulence and scalar transport. Studies have also investigated buoyancy effects, such as in unstably stratified turbulent boundary layers, revealing significant impacts on flow dynamics Appelbaum, Kloker, and Wenzel [30]. Additionally, DNS of adverse pressure gradient turbulent boundary layers have provided insights into the effects of pressure gradients on turbulence structure and behavior Parthasarathy and Saxton-Fox [31] and Pargal et al. [32]. In particular Araya and Castillo [33] have shown enhanced wall-normal turbulent heat fluxes as the APG increases. Pirozzoli et al. [34] studied passive scalars in turbulent pipe flow, highlighting the influence of Prandtl numbers on scalar transport. Alcántara-Ávila and Pérez-Quiles [35] conducted large-scale channel flow DNS with passive scalars, focusing on $Pr = 0.71$.

The combination of numerical simulations and experimental measurements continues to drive progress in this challenging field.

2.2 DNS of a Turbulent Boundary Layer

2.2.1 Main Challenges

Direct Numerical Simulation (DNS) of a developing turbulent boundary layer presents unique challenges compared to channel flow geometry.

Transition to Turbulence

One of the primary challenges is initiating or accelerating the transition to turbulence. Various methods have been employed to address this issue, such as the force method used by Spalart and Watmuff [36], which used one-step random force near the wall to quickly introduce turbulence without affecting the free stream, or Bertolotti, Herbert, and Spalart [37], which used a body force analogue of a vibrating ribbon, or one kind that mimic sand paper effect implemented by Chevalier et al. [38], described in details by Schlatter and Örlü [39] and later used by Li et al. [28] and also in this simulation (described in details in 4.4.2). This method involves applying a periodic force within a short region to generate waves in the flow, similar to the effect of a vibrating ribbon or sandpaper. This approach is more convenient than adding perturbations at the inflow, as it results in smoother transitions and shorter transient regions. Studies have shown that distributed three-dimensional roughness elements may be more effective in inducing transition compared to simple cylindrical wires.

Another approach is the rescaling-recycling method implemented by Lund, Wu, and Squires [40], which was used in multiple simulations by Abe, Mizobuchi, and Matsuo [41] and Abe [29] and has been further explored by Garai, Murman, and Ekelschot [42]. Their work highlights the challenge of imposing experimentally observed turbulent inflow profiles, which often do not exhibit self-similar behavior, and proposes an optimization-based technique for generating these profiles. Additionally, Araya and Castillo [33] refined Lund's method by incorporating a multi-scale approach, which uses distinct scaling laws for the inner and outer regions of the boundary layer, thereby improving the precision of thermal boundary layer representations.

Outflow Condition

Another significant challenge in DNS of turbulent boundary layers is the finite size of the computational domain. Proper boundary conditions must be chosen, especially at the outlet, to prevent backflows. Various methods have been investigated to address this issue.

The fringe region method aims to achieve a base flow profile at the outlet but introduces nonphysical elements into the domain, reducing the available analysis area. The key assumption is that the non-physical phenomena occurring in the fringe do not invalidate the solution in the useful region. This method is particularly useful because it allows the use of periodic boundary conditions required by fully spectral numerical methods, eliminating the need to provide turbulent inflow conditions. Periodic conditions are the easiest and most often used boundary conditions, leading to accurate and efficient Fourier series expansions, and consequently numerical advantages and good inflow quality. The method was first implemented by Spalart [43] and has been vastly investigated by Bertolotti, Herbert, and Spalart [37] and used in various simulations.

Another approach involves accelerating the flow at the outlet by imposing a positive velocity gradient to avoid backflows and is vastly used.

The convective outflow method is another technique used to manage boundary conditions at the outlet. This method involves applying a convective boundary condition that allows disturbances to exit the computational domain without reflecting back into the flow field. It effectively simulates an open boundary by assuming that the flow convects disturbances out of the domain at a specified speed, thus minimizing artificial reflections and maintaining the physical realism of the simulation. This method is implemented in Abe, Mizobuchi, and Matsuo [41].

Lastly, another method involves imposing a pressure condition at the outlet, as described by Dong, Karniadakis, and Chrysostomidis [44]. This approach sets a specific pressure value at the outlet, ensuring that the flow remains stable and preventing backflow into the computational domain. It is used in the present case and explained in details in 4.2.1.

Present Case

Turbulent pressure-gradient flows introduce additional complexities, such as non-trivial boundary conditions, along with the usual challenges of high memory and computational time requirements. In contrast, the boundary layer without a pressure gradient has been extensively studied, confirming its fundamental scaling laws over a wide range of parameters. This thesis aims to simulate a zero pressure gradient turbulent boundary layer using direct numerical simulation (DNS) to expand our understanding of scalar turbulent boundary layer flows across a broader range of Prandtl numbers (see 1.1), including liquid metal Prandtl numbers, specifically down to the value of Prandtl number for Sodium. Enhancing the available turbulent and thermal statistics, supporting the development of thermal turbulence models, and creating a comprehensive database for the research community are the primary objectives.

Chapter 3

Theoretical Formulation

3.1 Governing Equations

The Navier-Stokes (N-S) equations, which describe the motion of Newtonian fluids, were developed in the 19th century by Claude-Louis Navier and George Gabriel Stokes. Despite the varying nature of turbulent flows, these fundamental equations remain consistent. When combined with the continuity equation and the scalar transport equation, they create a system of five equations. These equations account for five variables: three velocity components, pressure, and scalar concentration.

3.1.1 Velocity Field

To accurately describe the instantaneous velocity field of a fluid, we rely on the continuity equation and the Navier-Stokes equations, which express the conservation of mass and momentum for an infinitesimal control volume. In conservative form are given by:

$$\begin{aligned}\frac{D\rho}{Dt} + \rho \nabla \cdot \mathbf{v} &= 0 \\ \rho \frac{D\mathbf{v}}{Dt} &= -\nabla p + \mu \nabla^2 \mathbf{v} + \mathbf{F}\end{aligned}$$

where ρ is the density, p is the pressure, \mathbf{v} is the velocity vector (u, v, w) , $\frac{D}{Dt}$ represents the "material derivative" operator, μ is the dynamic viscosity of the fluid and \mathbf{F} is the body force vector per unit volume.

For incompressible flow without applied forces in tensor notation, the equations reduce to:

$$\frac{\partial u_i}{\partial x_i} = 0 \tag{3.1}$$

$$\frac{\partial u_i}{\partial t} + u_j \frac{\partial u_i}{\partial x_j} = -\frac{1}{\rho} \frac{\partial p}{\partial x_i} + \nu \frac{\partial^2 u_i}{\partial x_j^2} \tag{3.2}$$

where u_i are the velocity components, x_i are the spatial coordinates and ν is the kinematic viscosity.

Reynolds-Averaged Navier-Stokes Equations (RANS)

In many practical scenarios, the focus is on the mean flow rather than the rapid fluctuations. To achieve this, the Reynolds decomposition is employed, which separates the instantaneous flow variables into their mean and fluctuating parts.

The RANS method involves averaging over a sufficient time period to establish a clear mean value, making it suitable primarily for stationary flows. The time-averaged value of a quantity ϕ is defined as:

$$\langle \phi \rangle(x_i) = \lim_{\tau \rightarrow \infty} \frac{1}{\tau} \int_0^\tau \phi(x_i, t) dt$$

This averaging process ensures that the mean of the fluctuating component is zero:

$$\langle \phi' \rangle = \lim_{\tau \rightarrow \infty} \frac{1}{\tau} \int_0^\tau \phi'(x_i, t) dt = 0$$

Thus, for stationary turbulence, the decomposition can be expressed as:

$$\phi(x_i, t) = \langle \phi \rangle(x_i) + \phi'(x_i, t)$$

For the specific case of velocity and pressure:

$$u_i = \langle u_i \rangle + u'_i$$

$$p = \langle p \rangle + p'$$

where $\langle u_i \rangle$ and $\langle p \rangle$ represent the mean components, and u'_i and p' represent the fluctuating components.

By applying the Reynolds decomposition to the Navier-Stokes and continuity equations and averaging, we derive the Reynolds-averaged Navier-Stokes equations:

$$\frac{\partial \langle u_i \rangle}{\partial x_i} = 0 \tag{3.3}$$

$$\langle u_j \rangle \frac{\partial \langle u_i \rangle}{\partial x_j} = -\frac{1}{\rho} \frac{\partial \langle p \rangle}{\partial x_i} + \nu \frac{\partial^2 \langle u_i \rangle}{\partial x_j^2} - \frac{\partial \langle u'_i u'_j \rangle}{\partial x_j} \tag{3.4}$$

These equations, known as the Reynolds equations, differ from those for laminar flow due to the presence of the term involving averaged products of fluctuating velocities. This term, $\langle u'_i u'_j \rangle$, is the Reynolds stress tensor, which arises from the non-linear convection term in the Navier-Stokes equations. It represents the additional momentum transfer due to turbulent fluctuations and is interpreted as a turbulent stress. This tensor is symmetric and generally has six independent components. These components are unknowns in the averaged equations of motion, and modeling them is crucial to close the Reynolds equations, leading to the closure problem.

Reynolds Stress transport equation

To further understand the behavior of turbulent flows, we derive the transport equation for the kinematic Reynolds stress $\langle u_i u_j \rangle$. By subtracting the averaged momentum equation 3.4 from the instantaneous momentum equation 3.2, multiplying by u_j , and averaging, where the indices i and j are interchanged, we obtain the Reynolds stress transport equation:

$$\begin{aligned} \frac{D \langle u'_i u'_j \rangle}{Dt} &= \frac{\partial \langle u'_i u'_j \rangle}{\partial t} + \langle u_k \rangle \frac{\partial \langle u'_i u'_j \rangle}{\partial x_k} \\ &= P_{ij} + \Pi_{ij} - \varepsilon_{ij} + D_{ij} \end{aligned} \quad (3.5)$$

$$P_{ij} = - \left(\langle u'_i u'_k \rangle \frac{\partial \langle u_j \rangle}{\partial x_k} + \langle u'_j u'_k \rangle \frac{\partial \langle u_i \rangle}{\partial x_k} \right)$$

$$\Pi_{ij} = -\frac{1}{\rho} \left(\left\langle u'_i \frac{\partial p'}{\partial x_j} \right\rangle + \left\langle u'_j \frac{\partial p'}{\partial x_i} \right\rangle \right)$$

$$\varepsilon_{ij} = 2\nu \left\langle \frac{\partial u'_i}{\partial x_k} \frac{\partial u'_j}{\partial x_k} \right\rangle$$

$$D_{ij} = \mathcal{D}_{ij}^\nu + \mathcal{D}_{ij}^t = \nu \frac{\partial^2 \langle u'_i u'_j \rangle}{\partial x_k^2} - \frac{\partial \langle u'_i u'_j u'_k \rangle}{\partial x_k}$$

The production term, P_{ij} , represents the rate of creation of the turbulent stress due to the mean strain. It involves the Reynolds stresses, $\langle u'_i u'_k \rangle$, and the gradients of the mean velocity, $\frac{\partial \langle u_j \rangle}{\partial x_k}$, indicating the interaction between turbulent fluctuations and the mean flow, leading to the production of turbulent kinetic energy. The pressure-strain term, Π_{ij} , accounts for the redistribution of turbulent kinetic energy among different components of the stress tensor. This term involves the correlation between the fluctuating velocity, u'_i , and the gradient of the fluctuating pressure, $\frac{\partial p'}{\partial x_j}$. It can be decomposed into the divergence of the pressure-velocity product, D_{ij}^p , which represents the spatial transport of turbulent stress by pressure fluctuations, and the traceless part, Φ_{ij} , which redistributes energy among the normal-stress components:

$$-\frac{1}{\rho} \left(\left\langle u'_i \frac{\partial p'}{\partial x_j} \right\rangle + \left\langle u'_j \frac{\partial p'}{\partial x_i} \right\rangle \right) = -\frac{\partial}{\partial x_k} \left(\frac{1}{\rho} \langle p' (u'_i \delta_{jk} + u'_j \delta_{ik}) \rangle \right) + \frac{1}{\rho} \left\langle p' \left(\frac{\partial u'_i}{\partial x_j} + \frac{\partial u'_j}{\partial x_i} \right) \right\rangle$$

The dissipation term, ε_{ij} , represents the rate at which turbulent kinetic energy is converted into thermal energy due to viscous action. It involves the viscosity, ν , and the gradients of the fluctuating velocity, $\frac{\partial u'_i}{\partial x_k}$, and is significant in the smallest scales of motion where turbulent velocity derivatives are large. The diffusion term, D_{ij} , represents the transport of turbulent stress by molecular and turbulent diffusion. It can be divided into viscous diffusion, \mathcal{D}_{ij}^ν , which is usually negligible except near solid boundaries, and turbulent diffusion, \mathcal{D}_{ij}^t , which represents the transport of turbulent stress by the fluctuating velocity and pressure. Each of these terms represents a physical process contributing to the stress budget at a point in space, and identifying their physical character is crucial for modeling and closing the equation.

Kinetic Energy transport equation

To understand the dynamics of turbulent flows, we derive the transport equation for the turbulent kinetic energy, $k \equiv \frac{1}{2} \langle u'_i u'_i \rangle$. The transport equation is given by:

$$\frac{\partial k}{\partial t} + u_j \frac{\partial k}{\partial x_j} = - \langle u'_i u'_j \rangle \frac{\partial \langle u_i \rangle}{\partial x_j} - \frac{1}{\rho} \frac{\partial \langle u'_j p' \rangle}{\partial x_j} - \frac{1}{2} \frac{\partial \langle u'_i u'_i u'_j \rangle}{\partial x_j} + 2\nu \left\langle u'_i \frac{\partial^2 u'_i}{\partial x_j \partial x_j} \right\rangle \quad (3.6)$$

The last term on the right-hand side, can be split into a molecular diffusion term and a true dissipation term as follows:

$$2\nu \left\langle u'_i \frac{\partial^2 u'_i}{\partial x_j \partial x_j} \right\rangle = 2\nu \frac{\partial \langle u'_i s'_{ij} \rangle}{\partial x_j} - 2\nu \langle s'_{ij} s'_{ij} \rangle$$

where s'_{ij} is the fluctuating strain rate tensor defined by

$$s'_{ij} = \frac{1}{2} \left(\frac{\partial u'_i}{\partial x_j} + \frac{\partial u'_j}{\partial x_i} \right)$$

The different terms on the right-hand side of equation (3.6) are defined as follows:

$$P_k \equiv - \langle u'_i u'_j \rangle \frac{\partial \langle u_i \rangle}{\partial x_j}$$

$$\Pi_k \equiv - \frac{1}{\rho} \frac{\partial \langle u'_j p' \rangle}{\partial x_j}$$

$$\varepsilon_k \equiv 2\nu \langle s'_{ij} s'_{ij} \rangle$$

$$D_k = D_k^\nu + D_k^t \equiv 2\nu \frac{\partial \langle u'_i s'_{ij} \rangle}{\partial x_j} - \frac{1}{2} \frac{\partial \langle u'_i u'_i u'_j \rangle}{\partial x_j}$$

where P_k is the turbulent energy production, ε_k is the true viscous dissipation, Π_k is the pressure diffusion, D_k^t is the turbulent diffusion, and D_k^ν is the viscous diffusion. Note that there is also a pseudo-dissipation term, but it is almost identical to the true dissipation term, so we will focus on the true dissipation in this formulation.

This section is based on the formulations presented in Hanjalić and Launder [45] and Pope [46].

3.1.2 Scalar Field

The transport of an instantaneous scalar property by turbulent motion can be described using the scalar conservation equation. This equation, in its general form, is expressed as:

$$\frac{\partial(\rho\theta)}{\partial t} + \frac{\partial(\rho\theta u_i)}{\partial x_i} = S + \frac{\partial}{\partial x_i} \left(\gamma \frac{\partial \theta}{\partial x_i} \right)$$

where θ is the scalar property, ρ is the density, u_i is the velocity component, γ is the thermal diffusivity, and S is the source term representing the rate of creation of the property per unit volume.

For many flows, the turbulent fluctuations of density and molecular diffusivity can be neglected.

In the case of a passive scalar, such as temperature or pollutant concentration, the transport equation simplifies to:

$$\frac{\partial \theta}{\partial t} + u_i \frac{\partial \theta}{\partial x_i} = \alpha \frac{\partial^2 \theta}{\partial x_i \partial x_i} \quad (3.7)$$

where θ is the passive scalar and α is the molecular diffusivity of the scalar, that is related to γ by:

$$\alpha \equiv \frac{\gamma}{\rho} = \frac{\lambda}{\rho C_p}$$

, where λ is the thermal conductivity and C_p is the specific heat at constant pressure. Analogous to the Reynolds decomposition of the velocity field, the instantaneous scalar can be split into a mean and a fluctuating part:

$$\theta = \langle \theta \rangle + \theta'$$

By inserting this decomposition into the transport equation and taking the average, we obtain the averaged transport equation for the scalar:

$$\frac{\partial \langle \theta \rangle}{\partial t} + u_i \frac{\partial \langle \theta \rangle}{\partial x_i} = \frac{\partial}{\partial x_i} \left(\alpha \frac{\partial \langle \theta \rangle}{\partial x_i} \right) - \frac{\partial \langle u'_i \theta' \rangle}{\partial x_i} \quad (3.8)$$

where $\langle \theta \rangle$ is the mean scalar and $\langle u'_i \theta' \rangle$ represents the turbulent flux of the scalar.

Turbulent Scalar Flux transport equation

By summing up the multiplied scalar conservation 3.7 with u_i and the multiplied momentum equation 3.2 by θ , and averaging, we obtain the transport equation for turbulent scalar flux:

$$\begin{aligned} \frac{D \langle \theta' u'_i \rangle}{Dt} &= \frac{\partial \langle \theta' u'_i \rangle}{\partial t} + \langle u_k \rangle \frac{\partial \langle \theta' u'_i \rangle}{\partial x_k} \\ &= P_{\theta i} + \Pi_{\theta i} - \varepsilon_{\theta i} + D_{\theta i} \end{aligned} \quad (3.9)$$

$$\mathcal{P}_{\theta i} = - \left(\langle u'_i u'_k \rangle \frac{\partial \langle \theta \rangle}{\partial x_k} + \langle \theta' u'_k \rangle \frac{\partial \langle u_i \rangle}{\partial x_k} \right)$$

$$\Pi_{\theta i} = - \frac{1}{\rho} \left\langle \theta' \frac{\partial p'}{\partial x_i} \right\rangle$$

$$\varepsilon_{\theta i} = (\alpha + \nu) \left\langle \frac{\partial \theta'}{\partial x_k} \frac{\partial u'_i}{\partial x_k} \right\rangle$$

$$\mathcal{D}_{\theta i} = \mathcal{D}_{\theta i}^\alpha + \mathcal{D}_{\theta i}^\nu + \mathcal{D}_{\theta i}^t = \frac{\partial}{\partial x_k} \left(\alpha \frac{\partial \langle u_i u_k \rangle}{\partial x_k} + \nu \frac{\partial \langle u_i u_k \rangle}{\partial x_k} - \langle \theta u_i u_k \rangle \right)$$

The generation terms, denoted as $\mathcal{P}_{\theta i}$, involve products of second-moment correlations and mean-field gradients, and do not require approximation. The diffusive transport

term, $\mathcal{D}_{\theta i}$, arises from velocity and pressure fluctuations as well as molecular transport, which includes contributions from scalar conductivity/diffusivity and fluid viscosity. The term $\Pi_{\theta i}$ represents the non-dispersive role of pressure fluctuations, which is crucial for the 'scrambling' of turbulent eddies, thereby reducing the magnitude and differences between components of the scalar flux. It is decomposed into a divergence part representing the turbulent diffusion of the scalar by pressure fluctuations, $\mathcal{D}_{\theta i}$, and a term $\Phi_{\theta i}$ interpreted as 'pressure scrambling' of the fluctuating scalar field:

$$-\frac{1}{\rho} \left\langle \theta' \frac{\partial p'}{\partial x_i} \right\rangle = -\frac{\partial}{\partial x_k} \left(\frac{1}{\rho} \langle p' u'_i \rangle \delta_{ik} \right) + \frac{1}{\rho} \left\langle p' \frac{\partial \theta'}{\partial x_i} \right\rangle$$

The dissipation term, $\varepsilon_{\theta i}$, accounts for the effects of molecular viscosity and scalar diffusivity on the turbulent scalar flux.

This section is based on the formulation presented in Hanjalić and Launder [45] and Bejan [47].

3.2 Turbulent Boundary Layer

Turbulent boundary layers are characterized by a complex hierarchy of eddy structures, ranging from large-scale motions to the smallest dissipative scales, known as the Kolmogorov length scale (see 5.1.1). This multiscale nature is governed by the energy cascade process, where kinetic energy is transferred from larger to smaller eddies until it is dissipated by viscous forces. Understanding the mechanism by which turbulent flows transport energy between a stream and a solid wall is crucial for predicting friction and heat transfer.

3.3 Equations

In a statistically stationary and two-dimensional boundary layer with the standard boundary layer approximations, namely negligible streamwise diffusion ($\partial/\partial x \ll \partial/\partial y$) and constant pressure throughout the boundary layer ($p = p(x)$), the mean flow equations reduce to:

$$\frac{\partial \langle u \rangle}{\partial x} + \frac{\partial \langle v \rangle}{\partial y} = 0$$

$$\langle u \rangle \frac{\partial \langle u \rangle}{\partial x} + \langle v \rangle \frac{\partial \langle v \rangle}{\partial y} = -\frac{1}{\rho} \frac{d \langle p \rangle}{dx} + \frac{\partial}{\partial y} \left(\nu \frac{\partial \langle u \rangle}{\partial y} \right) - \langle u'v' \rangle \quad (3.10)$$

$$\langle u \rangle \frac{\partial \langle \theta \rangle}{\partial x} + \langle v \rangle \frac{\partial \langle \theta \rangle}{\partial y} = \frac{\partial}{\partial y} \left(\alpha \frac{\partial \langle \theta \rangle}{\partial y} \right) - \langle v'\theta' \rangle \quad (3.11)$$

Note that in equation 3.10, we use $\frac{d \langle p \rangle}{dx}$ instead of $\frac{\partial \langle p \rangle}{\partial x}$ due to the boundary layer approximation for pressure, i.e., $\langle p \rangle$ is constant through the boundary layer and is a function of x only. The closure problem appears again in the two-dimensional turbulent boundary layer due to the two additional unknown terms, $\langle u'v' \rangle$ and $\langle v'\theta' \rangle$, in equations 3.10 and 3.11, respectively.

A form of 3.10 and 3.11 that resembles the laminar ones can be introduced, since the size of the u and T fluctuations with which the flow responds to the postulated v depends on the steepness of the average u and T profiles:

$$-\rho u'v' = \rho \epsilon_M \frac{\partial u}{\partial y} \quad (\text{eddy shear stress}),$$

$$-\rho c_p v'\theta' = \rho c_p \epsilon_H \frac{\partial \theta}{\partial y} \quad (\text{eddy heat flux}),$$

where ϵ_M and ϵ_H are two empirical functions known as momentum eddy diffusivity and thermal eddy diffusivity, respectively.

Substituting these notations into the boundary layer equations, we get:

$$\langle u \rangle \frac{\partial \langle u \rangle}{\partial x} + \langle v \rangle \frac{\partial \langle v \rangle}{\partial y} = -\frac{1}{\rho} \frac{d \langle p \rangle}{dx} + \frac{\partial}{\partial y} \left[(\nu + \epsilon_M) \frac{\partial \langle u \rangle}{\partial y} \right]$$

$$\langle u \rangle \frac{\partial \langle \theta \rangle}{\partial x} + \langle v \rangle \frac{\partial \langle \theta \rangle}{\partial y} = \frac{\partial}{\partial y} \left[(\alpha + \epsilon_H) \frac{\partial \langle \theta \rangle}{\partial y} \right]$$

These equations are used for turbulence modeling, where ϵ_M and ϵ_H are determined empirically (see Bejan [47]). However, for Direct Numerical Simulation (DNS), there is no need for turbulence modeling, and the original form of the boundary layer equations 3.10 and 3.11 is used.

3.3.1 Scalings

An important concept in boundary layer problems is self-similarity, which implies that the velocity profiles at different streamwise positions x appear similar, and the same applies to the scalar profile. By applying appropriate scaling, all profiles at various downstream positions can collapse onto a single curve.

For turbulent boundary layer flows, similarity solutions for the mean velocity and mean scalar profiles are sought separately in the inner and outer regions of the boundary layer. These regions exhibit different characteristics. The individual terms in equations 3.10 and 3.11 have varying importance in these regions; for instance, convection terms are significant in the outer region, while viscous and scalar flux terms are more critical in the inner region.

Inner Region Scaling

The behavior of the flow near the wall is crucial because many engineering-relevant features are determined in the inner layer. Ludwig Prandtl first addressed the inner layer. The boundary layer equation for the flow field in the inner part, simplified from equation 3.10, reads:

$$0 = \nu \frac{\partial^2 \langle u \rangle}{\partial y^2} - \frac{\partial}{\partial y} \langle u'v' \rangle \quad (3.12)$$

Integrating this equation in y , we obtain:

$$\nu \frac{\partial \langle u \rangle}{\partial y} - \langle u'v' \rangle \Big|_{y=0} = \text{constant} \equiv \tau / \rho$$

Note that the Reynolds stress $\langle u'v' \rangle$ vanishes at the wall due to the no-slip boundary condition:

$$\nu \frac{\partial \langle u \rangle}{\partial y} \Big|_{y=0} \equiv \tau_w / \rho \quad (3.13)$$

, where τ is the total mean shear stress and τ_w is the total mean shear stress at the wall.

The characteristic length scale in the inner region can be defined as:

$$l^* \equiv \nu / u_\tau \quad (3.14)$$

where u_τ is the friction velocity, defined as:

$$u_\tau \equiv \sqrt{\tau_w / \rho} = \sqrt{\nu \frac{\partial \langle u \rangle}{\partial y} \Big|_{y=0}} \quad (3.15)$$

The wall-normal distance expressed in viscous scaling, also known as inner scaling or wall units, becomes:

$$y^+ \equiv y / l^* = y u_\tau / \nu \quad (3.16)$$

Using viscous scaling, the mean streamwise velocity can be written as:

$$u^+ \equiv \langle u \rangle / u_\tau = \Phi_1(y^+) \quad (3.17)$$

This equation is known as the law of the wall. It assumes that outer geometrical constraints, such as the outer length scale, have a negligible effect when sufficiently close to the wall. Consequently, the velocity and Reynolds shear stress profiles depend solely on y^+ , rather than both y^+ and Re . Here, Re is defined as $Re = \frac{UL}{\nu}$, where U represents the velocity scale, L the length scale, and ν the kinematic viscosity. Therefore, the law of the wall is universal, meaning the function Φ_1 remains the same for all flows at sufficiently high Reynolds numbers. Under these conditions, the law of the wall aligns well with measurements and simulations for $y < 0.3\delta$, where δ is the boundary layer thickness. Typically, the boundary layer thickness is defined as the point where the streamwise velocity $\langle u \rangle$ reaches 99% of the free-stream velocity U_∞ .

$$\langle u \rangle(y = \delta_{99\%}) = 0.99U_\infty \quad (3.18)$$

Similarly, as the mean velocity, the Reynolds shear stress using viscous scaling can be written as:

$$\langle u'v' \rangle^+ \equiv -\langle u'v' \rangle / u_\tau^2 = \Phi_2(y^+) \quad (3.19)$$

which is found to hold for $y < 0.1\delta$ when the Reynolds number of the flow is very high.

Using viscous scaling, equation 3.13 can be written as:

$$\tau^+ \equiv \frac{du^+}{dy^+} - \langle u'v' \rangle^+ = 1 \quad (3.20)$$

or

$$\Phi_1'(y^+) + \Phi_2(y^+) = 1 \quad (3.21)$$

In the region very close to the wall, viscous forces are predominant, making the viscous stress significantly higher than the Reynolds shear stress. This area is known as the viscous sub-layer. By neglecting the Reynolds shear stress term, equation 3.12 can be integrated within this layer to obtain:

$$u^+ = y^+ \quad (3.22)$$

This relation indicates that the velocity profile is a linear function of a single variable, which is influenced by both x and y . This linear relationship is observed to hold true for $y^+ < 5$.

For the scalar field, we expect similar behavior as for the velocity field. By the same reasoning as above, the boundary layer equation for the scalar field in the inner part, simplified from equation 3.11, reads:

$$0 = \alpha \frac{\partial^2 \langle \theta \rangle}{\partial y^2} - \frac{\partial \langle v'\theta' \rangle}{\partial y} \quad (3.23)$$

Similarly, the law of the wall for the scalar field reads:

$$\theta^+ \equiv \frac{\theta_w - \langle \theta \rangle}{\theta_\tau} = \Phi_\theta(y^+, Pr) \quad (3.24)$$

Here, the function Φ_θ is a universal function that depends on y^+ and the molecular Prandtl number Pr , defined as $Pr = \frac{\nu}{\alpha}$, where ν is the kinematic viscosity and α is the scalar molecular diffusivity. The scalar concentration at the wall is denoted by θ_w . The term θ_τ is referred to as the friction scalar or friction temperature when θ represents

temperature. According to Cebeci and Bradshaw [48], the friction temperature is analogous to the friction velocity u_τ and is defined by:

$$\theta_\tau \equiv \frac{q_w}{\rho c_p u_\tau} \quad (3.25)$$

where ρ is the density of the fluid, c_p is the heat capacity of the fluid, u_τ is the friction velocity, and q_w is the rate of heat transfer from the wall to the flow, which is defined by:

$$q_w = -\lambda \left. \frac{d\langle\theta\rangle}{dy} \right|_{y=0}, \quad (3.26)$$

where λ is the thermal conductivity. This equation is known as the heat conduction law or Fourier's law. Similarly, very close to the wall, there exists a conductive sub-layer for the scalar field, analogous to the viscous sub-layer for the velocity field. From the heat conduction law, we can derive the equation for the conductive sub-layer:

$$\theta^+ = Pr \cdot y^+. \quad (3.27)$$

Notably, this inner scaling equation highlights the dependency on the Prandtl number Pr , compared with the velocity field's scaling that does not involve Pr . This linear relationship is valid for $Pr \cdot y^+ < 3$ (Cebeci and Bradshaw [48]).

Outer Region Scaling

In the outer region of the turbulent boundary layer, the effect of viscosity ν is minimal, making the viscous stress negligible. As a result, equation 3.10 simplifies to:

$$\langle u \rangle \frac{\partial \langle u \rangle}{\partial x} + \langle v \rangle \frac{\partial \langle u \rangle}{\partial y} = -\frac{\partial \langle u'v' \rangle}{\partial y} \quad (3.28)$$

The pressure term is omitted due to the zero pressure gradient condition, meaning $\frac{dp}{dx} = 0$. The characteristic length scale in this outer region is defined as:

$$\Delta \equiv \delta^* \quad (3.29)$$

where δ^* represents the displacement thickness, given by:

$$\delta^* = \int_0^\infty \left(1 - \frac{\langle u \rangle}{U_\infty} \right) dy \quad (3.30)$$

The wall-normal distance in the outer region is scaled as:

$$\eta \equiv \frac{y}{\Delta} = \frac{y}{\delta^*} \quad (3.31)$$

In the outer part of the turbulent boundary layer, the turbulence is primarily inviscid. The Reynolds shear stress in this region induces a drag on the flow, creating a velocity defect ($\langle u \rangle - U_\infty$), which is expected to be proportional to the wall friction characterized by u_τ . Thus, the mean velocity is scaled as:

$$\frac{\langle u \rangle - U_\infty}{u_\tau} = \Psi_1(\eta) \quad (3.32)$$

known as the velocity defect law. The Reynolds shear stress is scaled as:

$$-\frac{\langle u'v' \rangle}{u_\tau^2} = \Psi_2(\eta) \quad (3.33)$$

For consistency, if a different velocity scale is used for the Reynolds shear stress, the ratio $\frac{u_\tau}{U_\infty}$ must approach a constant at infinitely high Reynolds numbers. The scalar field equation in the outer region, simplified from equation 3.11, becomes:

$$\langle u \rangle \frac{\partial \langle \theta \rangle}{\partial x} + \langle v \rangle \frac{\partial \langle \theta \rangle}{\partial y} = -\frac{\partial \langle v'\theta' \rangle}{\partial y} \quad (3.34)$$

This leads to the defect law for the scalar field:

$$\frac{\langle \theta \rangle - \theta_\infty}{\theta_\tau} = \Psi_\theta(\eta) \quad (3.35)$$

where θ_∞ is the scalar concentration in the free-stream, and θ_τ is the friction scalar.

Buffer Region

From the previous analysis, we understand that the velocity and scalar fields follow distinct laws in the inner and outer regions of the boundary layer. However, at sufficiently high Reynolds numbers, the outer boundary of the inner layer can overlap with the inner boundary of the outer layer. This implies that the behavior described by equations 3.17, 3.19, and 3.24 as $y^+ \rightarrow \infty$ should match the behavior given by equations 3.32, 3.33, and 3.35 as $\eta \rightarrow 0$. Consequently, in the overlap region where $l^* \ll y \ll \delta^*$, all these equations are valid simultaneously. The classical approach involves matching the equations from both the inner and outer regions. Following the derivation by Hunt [49], we obtain:

$$\Phi_1(y^+) = \frac{\langle u \rangle}{u_\tau} = \frac{1}{\kappa} \ln(y^+) + A \quad (3.36)$$

$$\Psi_1(\eta) = \frac{\langle u \rangle - U_\infty}{u_\tau} = \frac{1}{\kappa} \ln(\eta) + B \quad (3.37)$$

where κ is the Kármán constant. Experimental data suggest that $\kappa \approx 0.41$, $A \approx 5.2$, and $B \approx 1$. Equations 3.36 and 3.37 describe the velocity distribution in the overlap region and are commonly referred to as the logarithmic law or log-law. In this thesis, the Kármán constant κ is set to 0.41.

The log-law for the scalar field has a similar form to that of the velocity field:

$$\Phi_\theta(y^+, Pr) = \frac{\theta_w - \langle \theta \rangle}{\theta_\tau} = \frac{1}{\kappa_\theta} \ln(y^+) + A_\theta(Pr) \quad (3.38)$$

$$\Psi_\theta(\eta) = \frac{\theta_\infty - \langle \theta \rangle}{\theta_\tau} = \frac{1}{\kappa_\theta} \ln(\eta) + B_\theta(Pr) \quad (3.39)$$

where the Kármán constant for the scalar field, κ_θ , is 0.33. Both A_θ and B_θ are functions of the Prandtl number Pr . It may be more logical to express the argument of the logarithm as $Pr \cdot y^+$, incorporating the scalar conductivity rather than the viscosity, but this would only alter the constant A_θ without eliminating it.

In equation 3.24, it is evident that there is a dependence on the Prandtl number Pr , which is not present in equation 3.17 for the velocity field. The Prandtl number, Pr , can vary significantly depending on the fluid, ranging from very low values for liquid metals (as low as 0.001) to very high values for viscous fluids like oils (exceeding 100). In this thesis, we focus on the lower bound of the Prandtl number range, as described in 1.2.1.

It is important to note that we assume the term $\alpha \frac{\partial \langle \theta \rangle}{\partial y}$ is dominant in the inner region, while the term $\langle v' \theta' \rangle$ is dominant in the outer region. However, this assumption may not always hold true, as $\alpha \frac{\partial \langle \theta \rangle}{\partial y}$ can vary greatly with the Prandtl number. The neglected terms in the inner and outer regions are not zero; they are simply small compared to the dominant terms. By selecting a different Prandtl number, the dominance of these terms may be reversed.

For the purposes of this thesis, we neglect $\langle v' \theta' \rangle$ in the inner region and $\alpha \frac{\partial \langle \theta \rangle}{\partial y}$ in the outer region, restricting our analysis to $O(Pr) = 1$. The function Φ_θ in equation 3.24, which depends on both y^+ and Pr , helps to account for this effect.

Chapter 4

Direct Numerical Simulation

4.1 Non-Dimensional Form of the Navier-Stokes and Scalar Transport Equations

Non-dimensionalizing the Navier-Stokes and scalar transport equations simplifies the analysis and generalization of fluid dynamics problems. By converting variables into non-dimensional forms, the equations become independent of specific flow conditions, fluid properties, or scales, making them universally applicable.

The non-dimensional governing equations are:

$$\begin{aligned}\frac{\partial u_i^*}{\partial x_i^*} &= 0 \\ \frac{\partial u_i^*}{\partial t^*} + u_j^* \frac{\partial u_i^*}{\partial x_j^*} &= -\frac{\partial p^*}{\partial x_i^*} + \frac{1}{Re} \frac{\partial^2 u_i^*}{\partial x_j^* \partial x_j^*} \\ \frac{\partial \theta^*}{\partial t^*} + u_i^* \frac{\partial \theta^*}{\partial x_i^*} &= \frac{1}{RePr} \frac{\partial^2 \theta^*}{\partial x_i^* \partial x_i^*}\end{aligned}$$

The non-dimensional variables are defined as follows:

$$u_i^* = \frac{u_i}{U_\infty}, \quad x_i^* = \frac{x_i}{\delta_0^*}, \quad \theta^* = \frac{\theta - \theta_\infty}{\theta_w - \theta_\infty}, \quad p^* = \frac{p}{\rho U_\infty^2}, \quad t^* = \frac{t U_\infty}{\delta_0^*}$$

For the isothermal boundary condition:

$$\theta^* = \frac{\lambda(\theta - \theta_\infty)}{q_w \delta_0^*}$$

For the isoflux boundary condition:

$$\theta^* = \frac{\theta - \theta_\infty}{\theta_w - \theta_\infty}$$

Here, $*$ denotes a non-dimensional variable, x_i are the coordinates, U_∞ is the undisturbed laminar streamwise free-stream velocity at $x = 0$ and $t = 0$, and δ_0^* is the displacement thickness of the undisturbed streamwise velocity at $x = 0$ and $t = 0$. ρ is the fluid density, θ_w and θ_∞ are the scalar concentrations at the wall and in the

free-stream, respectively. q_w is the rate of scalar transfer from the wall to the flow, and λ is the scalar conductivity.

In these equations, the Reynolds number Re is based on the free-stream velocity U_∞ and the inlet displacement thickness δ_0^* , while Pr is the molecular Prandtl number. The product of Re and Pr is the Péclet number (Pe), which represents the ratio of convective transport of the scalar to its molecular diffusion. By using non-dimensional equations, we can easily simulate different passive scalars by varying the Prandtl number, thus changing the Péclet number, without needing to specify the properties of each fluid.

Note: for simplicity, the superscript $*$ will be dropped from the non-dimensional variables unless specified otherwise.

4.2 Boundary Conditions

To fully define the governing equations, it is essential to specify appropriate boundary conditions. These conditions are critical as they determine the fluid's behavior at the domain boundaries, ensuring the problem is well-posed.

4.2.1 Boundary Conditions for Flow Field

Wall Boundary Condition

At the wall, the no-slip boundary conditions apply, meaning the velocity of the fluid at a solid surface must be equal to the velocity of the surface:

$$u|_{y=0} = 0, \quad v|_{y=0} = 0, \quad w|_{y=0} = 0$$

Additionally,

$$\left. \frac{\partial v}{\partial y} \right|_{y=0} = 0$$

This condition is derived from the continuity equation and ensures that there is no slip between the fluid and the wall.

Upper Boundary Condition

At the upper boundary of the domain in the wall-normal direction, Dirichlet and Neumann boundary conditions are typically more appropriate for simulations. However, since the full stress formulation, which assigns the components of the stress tensor, is required to impose the Neumann condition, and given that the domain height y_L is sufficiently large for the velocity field, a slip condition (also called symmetry) has been chosen:

$$v = 0, \quad \frac{\partial u}{\partial x} = 0, \quad \frac{\partial w}{\partial z} = 0$$

Inlet Boundary Condition

At the inlet in the stream direction, a Dirichlet condition is imposed with the velocity specified as the Blasius velocity profile. The Blasius profile is a similarity solution for the laminar boundary layer over a flat plate, derived from the more general Falkner-Skan equation. The Falkner-Skan equation describes the steady two-dimensional laminar boundary layer that forms on a wedge and is given by:

$$f''' + \frac{m+1}{2} f f'' + m(1 - (f')^2) = 0$$

where f is the dimensionless stream function, $\eta = \frac{y}{\delta}$ is the similarity variable, and m is a parameter related to the pressure gradient along the plate, defined as:

$$m = \frac{x}{U_\infty} \frac{dU_\infty}{dx} \quad (4.1)$$

For the Blasius solution, which corresponds to a flat plate with zero pressure gradient, $m = 0$. This simplifies the Falkner-Skan equation to:

$$f''' + f f'' = 0$$

The boundary conditions for this equation are:

$$f(0) = 0, \quad f'(0) = 0, \quad f'(\infty) = 1$$

where $f'(\eta) = \frac{u}{U_\infty}$. Here, U_∞ is the free-stream velocity, and δ is the boundary layer thickness. The Blasius solution provides a self-similar velocity profile that serves as the inlet profile for the simulation (see Cebeci and Bradshaw [48]).

Outlet Boundary Condition

At the outlet in the stream-wise direction, a standard outlet condition with $\nabla \mathbf{u} = 0$ is typically specified. However, to better handle the outflow and ensure stability, the outflow condition from Dong, Karniadakis, and Chrysosostomidis [44] is applied. This condition is designed to manage vortices and backflows at the outflow boundary. The condition over the pressure is given by:

$$p = \nu(\mathbf{n} \cdot \nabla \mathbf{u}) \cdot \mathbf{n} - \frac{1}{2} |\mathbf{u}|^2 S_0(\mathbf{n} \cdot \mathbf{u})$$

where

$$S_0(\mathbf{n} \cdot \mathbf{u}) = \frac{1}{2} \left(1 - \tanh \left(\frac{\mathbf{n} \cdot \mathbf{u}}{U_0 \delta} \right) \right)$$

Here, ν is the kinematic viscosity, \mathbf{n} is the unit normal vector at the outflow boundary, \mathbf{u} is the velocity vector, U_0 is a reference velocity taken in this case equal to the free-stream velocity, and δ is a small parameter to control the smoothness of the transition. This formulation helps to mitigate the artificial reflections and numerical instabilities that can occur at the outflow boundary, ensuring a more accurate and stable simulation.

Span-wise Boundary Conditions

In the span-wise direction, periodicity is imposed:

$$p(z) = p(z + \delta z), \quad \mathbf{u}(z) = \mathbf{u}(z + \delta z)$$

Note: The pressure boundary conditions are not explicitly specified in the sections above because they are inherently determined by the velocity boundary conditions. In general, the boundary condition for pressure must satisfy the following equation, unless explicitly stated otherwise:

$$\nabla \cdot \left(\frac{1}{\rho} \nabla p \right) = -\nabla \cdot \left(\frac{D\mathbf{u}}{Dt} \right) + \nabla \cdot \left(\frac{1}{\rho} (\nabla \cdot \boldsymbol{\tau}) \right) + \nabla \cdot \mathbf{f}$$

where the stress tensor $\boldsymbol{\tau}$ is given by:

$$\boldsymbol{\tau} = \mu [\nabla \mathbf{u} + (\nabla \mathbf{u})^T]$$

In the case of a zero pressure gradient, this implies that the pressure value can be specified on only one boundary. On all other boundaries, the condition $\frac{\partial p}{\partial n} = 0$ must be satisfied to ensure the problem is well-posed and not over-constrained.

4.2.2 Boundary Conditions for Scalar Field

Wall Boundary Condition

In the present implementation for the scalar field, we use two types of wall boundary conditions: isothermal and isoflux. These boundary conditions are defined as follows:

$$\theta|_{y=0} = 1 \quad \text{for the isothermal boundary condition}$$

$$\left. \frac{\partial \theta}{\partial y} \right|_{y=0} = -1 \quad \text{for the isoflux boundary condition}$$

These boundary conditions represent extreme cases of physical scenarios. When θ represents temperature, the isothermal boundary condition models a situation where the fluid, characterized by low density ρ , specific heat c_p , and thermal conductivity λ , is in contact with a thick wall that has high density ρ_w , specific heat c_{pw} , and thermal conductivity λ_w . In this scenario, the thermal activity ratio K is given by:

$$K = \frac{\rho c_p \lambda}{\rho_w c_{pw} \lambda_w}$$

and approaches zero. On the other hand, the isoflux boundary condition models a thin wall with low density, specific heat, and thermal conductivity, while the fluid properties are relatively large, resulting in a thermal activity ratio K that approaches infinity (Tiselj et al. [50]).

For more general cases, the conjugate heat transfer problem must be solved, which involves solving the coupled equations for both the fluid and the solid. This approach accounts for the unsteady heat conduction in the solid wall and the turbulent heat transfer in the fluid.

Upper Boundary Condition

At the upper boundary of the domain in the wall-normal direction, an isothermal boundary condition is applied:

$$\theta|_{y=y_L} = 0$$

This condition ensures that the scalar field reaches a specified value at the upper boundary, simulating an environment where the scalar concentration is maintained at a constant level far from the wall.

Inlet Boundary Condition

At the inlet in the stream direction, a Dirichlet condition is imposed with the temperature being zero for all the scalars:

$$\theta = 0$$

Outlet Boundary Condition

At the outlet in the streamwise direction, a standard outlet condition is applied:

$$\frac{\partial \theta}{\partial n} = 0$$

Span-wise Boundary Condition

In the span-wise direction, periodicity is imposed:

$$\theta(z) = \theta(z + \delta z)$$

4.3 Computational Domain

In this thesis, we examine the development of a turbulent boundary layer flow over a flat plate with passive scalars, under zero pressure gradient (ZPG) conditions. The simulation begins with a laminar Blasius boundary layer at the inlet, characterized by a Reynolds number $Re_x = 68385$, where Re_x is the Reynolds number based on the streamwise position x and the free-stream velocity U_∞ , as described in 4.2.1. The laminar flow is then tripped by a random volume force (see 4.4.2) strip to transition and eventually becomes turbulent. The trip forcing in this case is located at the wall at a streamwise position of $x = 10$, corresponding to $Re_x = 72885$. The computational domain is a three-dimensional cuboid bounded at the lower edge by a flat plate with a no-slip boundary condition. The boundary layer grows in the domain, starting with an initial boundary layer thickness δ_0^* . At the end of the computational domain in the streamwise direction, the pressure is imposed as described in 4.2.1.

All relevant flow quantities are scaled with the inlet boundary layer displacement thickness δ_0^* , the free-stream velocity U_∞ , and the viscosity ν . The Reynolds number based on the inlet displacement thickness and free-stream velocity is set to 450 in the simulation. The distance from the leading edge x_0 can then be computed from

$$\frac{x_0}{\delta_0^*} = \frac{Re_{\delta_0^*}}{1.72^2} = 154$$

which corresponds to $Re_x = 68385$ or $Re_\theta = 174$. The values of the various Reynolds numbers are listed in Table 4.1 with respect to the downstream locations. The trends, along with the plots and averages, are presented in 5. The simulation is carried out in a computational box with the length x_L , height y_L , and width z_L being $350\delta_0^*$, $30\delta_0^*$, and $34\delta_0^*$, respectively. The vertical extent of the box must include the entire boundary layer. Depending on the choice of free-stream boundary condition, the box may include only the boundary layer or a few times more. The sufficiency of the box height may be investigated through numerical simulations.

A grid of $210 \times 14 \times 24$ elements is used in the streamwise, wall-normal, and spanwise directions, respectively. The element distribution is uniform in the streamwise and spanwise directions and is characterized a ratio $r = 1.28$ in the wall-normal direction. The grid spacing inside each element is based on Gauss-Lobatto-Legendre collocation points. The collocation points are the roots of the derivative of the Legendre polynomial $P'_N(x)$, where $P_N(x)$ is the Legendre polynomial of degree N , along with the endpoints -1 and 1 . These points ensure optimal placement for numerical integration and differentiation. The number of points is set to 9, corresponding to an 8th-order polynomial, which improves the computational efficiency of the simulation (see C).

An adaptive time-stepping method, using the third-order backward differentiation formula (bdf3), is employed for this Direct Numerical Simulation until the statistical steady-state is reached, where the time step is adjusted to maintain the Courant-Friederichs-Lewy (CFL) number below $CFL = 0.3$ (maximum value). For the averaging part a constant time step is set, equal to the average time step size, Δt that is approximately 0.0074. The code is compiled for 2048 processors, which are parallel vector processors with distributed memory and the statistics are averaged over 1100 time units, $\frac{\delta_0^*}{U_\infty}$.

x	Re_{δ^*}	Re_θ	Re_x
0	450	174	68385
10	446	203	72885
100	548	339	113385
150	628	396	135886
175	665	422	147136
200	704	448	158386
225	742	476	169636
250	784	504	180886
275	823	531	192136
300	857	554	203386
325	887	575	214636
350	921	598	225886

Table 4.1: Reynolds numbers with respect to the downstream location x

4.4 Numerical Method

The numerical code Nek5000 is used for calculations presented in this thesis. It is written in FORTRAN77 and developed by Argonne National Laboratory (ANL). The code solves weakly compressible Navier-Stokes equations. The code utilizes the Message Passing Interface (MPI) protocol to solve the equations in parallel. Parts of the code implementing the particular case are taken from the KTH toolbox, which is part of the KTH Framework for Nek5000 simulations KTH-Nek5000 [51]. The toolbox has been successfully applied in various studies and simulations on different workstations and supercomputers Massaro et al. [52].

4.4.1 Numerical scheme

The numerical code used in Nek5000¹ for solving the incompressible Navier-Stokes equations is based on the spectral element method (SEM). This method combines the geometric flexibility of finite elements with the high accuracy of spectral methods. The domain is divided into smaller subdomains (elements), and within each element, the solution is approximated using high-order polynomials.

The time advancement in Nek5000 is performed using a semi-implicit method. The non-linear terms are treated explicitly using Adams-Bashforth schemes, while the linear terms are treated implicitly using backward differentiation formulas (BDF). This approach ensures stability and accuracy in the numerical solution. The spatial discretization involves using Lagrange interpolation polynomials at Gauss-Lobatto-Legendre (GLL) points within each element, ensuring spectral accuracy (see Perez et al. [53]).

The Karniadakis scheme is used for the time integration of the Navier-Stokes equations. This scheme splits the computation into three substeps. First, the non-linear terms are computed explicitly using Adams-Bashforth schemes. Then, the pressure is computed by solving a Poisson equation. Finally, the velocity is updated by solving a Helmholtz equation. This splitting of the pressure and velocity computations is at the core of the Karniadakis scheme.

The pressure Poisson equation is derived by taking the divergence of the momentum equation and using the incompressibility condition. The boundary conditions for the pressure are derived from the semi-discrete formulation and are approximated using a high-order extrapolation scheme. The velocity field is decomposed into its irrotational and solenoidal components, and the pressure equation is solved using the rotational form of the Laplacian.

There are two common approaches for solving the incompressible Navier-Stokes equations using SEM: the $P_n - P_n$ formulation, in which both the velocity and pressure fields are approximated using the same polynomial order P_n and the $P_n - P_{n-2}$ formulation, that approximates the velocity field using a polynomial order P_n , while the pressure field is approximated using a polynomial order P_{n-2} . The first one ensures that the velocity and pressure fields are represented with the same level of accuracy, on the other hand, the second approach reduces the computational cost by using a

¹P. F. Fischer, J. W. Lottes, S. G. Kerkemeier, and B. Smith, "Nek5000 v19.0," Argonne National Laboratory, 2008. Available: <https://nek5000.mcs.anl.gov>

lower polynomial order for the pressure field, but it can introduce splitting errors (see Joshi and Abedi [54] and Krantz, Gholamisheeri, and Karp [55]).

Overall, the numerical scheme in Nek5000 leverages the strengths of the spectral element method to solve the incompressible Navier-Stokes equations effectively, ensuring high-order accuracy and stability.

4.4.2 Random Volumetric Force

In transient simulations, the choice of initial disturbances plays a crucial role. Unlike controlled experimental setups where specific disturbances are introduced, real-world scenarios often involve random disturbances. These can include surface waviness, defects in screens and free-stream noise, which are inherently random in nature. By incorporating random disturbances, simulations can more accurately reflect the continuous spectrum of real flow conditions, providing a more realistic approximation of the natural instability mechanisms (see Spalart and Yang [56]).

To simulate these random disturbances, a random volume force is implemented, acting in the wall-normal direction. This tripping force is designed to mimic the effects of physical tripping devices, such as sandpaper, by introducing low amplitude random noise into the flow. The force is applied along a line defined by its starting and ending points, and can be either finite or infinite in length and applied within an elliptical region along the line, defined by the smoothing lengths l_x and l_y , and rotated by an angle ζ . The force direction is always normal to the line, with its magnitude fluctuating randomly.

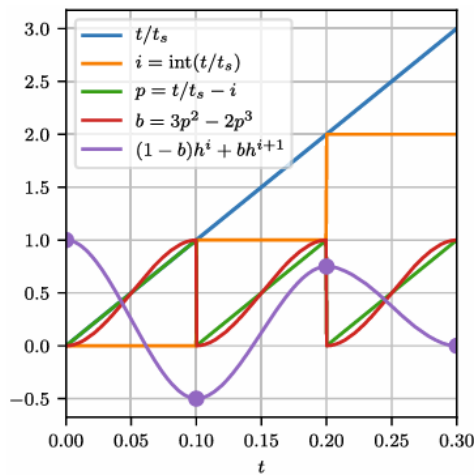


Figure 4.1: *Illustration of the time-dependent components of the tripping function. The resulting function has a continuous time derivative* Massaro et al. [52]

The tripping force is composed of both steady and unsteady components, with amplitudes A and A_t , respectively. The unsteady component is implemented using third-order Lagrange interpolants with a time scale t_s , ensuring continuity in the zeroth and first-order derivatives. The force is described by the following equations and shown in Figure 4.1:

$$\mathbf{F} = f_{\text{smth}}(r) \cdot \mathbf{f}(\mathbf{z}, \mathbf{t})$$

with $\mathbf{F} = (f_x, f_y, f_z)$

$f_{\text{smth}}(r)$ is the smoothing function, defined as:

$$f_{\text{smth}}(r) = \begin{cases} \exp(-r^2) \cdot (1 - r^2)^2 & \text{if } r \leq 1.0 \\ 0 & \text{if } r > 1.0 \end{cases}$$

with $r = \left(\frac{x_{loc}}{l_x}\right)^2 + \left(\frac{y_{loc}}{l_y}\right)^2$, where x_{loc} and y_{loc} are the coordinates obtained by rotating the GLL point coordinates clockwise by the angle ζ relative to the tripping line.

$$f(z, t) = A \cdot g(z) + A_t \cdot [(1 - b(t)) h^i(z) + b(t) h^{i+1}(z)],$$

with

$$\begin{aligned} i &= \text{int}(t/t_s) \\ b(t) &= 3p^2 - 2p^3 \\ p &= t/t_s - i \end{aligned}$$

and $g(z)$, $h(z)$ being Fourier series of unit amplitude with random coefficients. This formulation ensures that the tripping force generates noise uniformly distributed over all frequencies lower than the cutoff frequency corresponding to $2\pi/t_s$, where t_s is the time interval between changes in the time-dependent part of the trip. This approach provides a realistic representation of random disturbances in the flow.

Force Parameter	Value	Description
\mathcal{N}	48	Number of Fourier modes
ζ	0.123	Rotation angle [rad]
A	0.015	Time independent amplitude
A_t	0.025	Time dependent amplitude
l_x	8	Smoothing length x
l_y	1	Smoothing length y
z_s	0	Spanwise scale
t_s	4	Temporal scale

Table 4.2: Parameters set in the simulation

The force used in the simulation is part of the Nek5000 toolboxes developed at KTH Royal Institute of Technology, which is based on the implementation of the same volumetric force in SIMSON by Chevalier et al. [38], and it is described in detail by Schlatter and Örlü [39]. The parameters of the force used in the simulation are given in Table 4.2. For a detailed explanation of the forcing terms and how they influence the flow, see Schlatter and Örlü [39].

Chapter 5

Results

Two direct numerical simulations (DNS) were conducted, yielding extensive statistics on both the mean flow and the scalar distributions, along with their corresponding fluctuations. This chapter presents these results and compares them with other simulations, especially the one by Li et al. [28]. The first simulation ran for a total of 5000 time units $\frac{\delta_0^*}{U_\infty}$, with averages computed over the last 3000 time units $\frac{\delta_0^*}{U_\infty}$ to ensure convergence, using a smaller domain corresponding to $150\delta^* \times 20\delta^* \times 32\delta^*$. A second simulation, whose results are mainly presented in this thesis, was carried out for a total of 1800 time units $\frac{\delta_0^*}{U_\infty}$, with averages computed over the last 1100 time units $\frac{\delta_0^*}{U_\infty}$ with the setup presented in Chapter 4. A larger domain was analyzed to better compare the results with the results of Li et al. [28] at higher Re_θ , and although the simulation ran for a shorter duration, the results achieved comparable level of accuracy for almost all the averaged quantities. The code was executed on 1024 CPUs for the first simulation and on 2048 CPUs for the second, utilizing parallel processors and distributed memory.

Before collecting averaged statistical data, it is essential to verify that the simulation has reached a statistical steady state. This is done by plotting the velocity field components, integrated over the entire domain, against time, as shown in Figure 5.1. The streamwise component remains constant, as the imposed tolerance on the velocity field matches the magnitude of the oscillations around the mean value, indicating numerical stability. The wall-normal and spanwise components show an initial transient, followed by sustained oscillations.

In addition, the dissipation rate of the turbulent kinetic energy, converted into thermal internal energy, is monitored to confirm a statistical steady state, as shown in Figure 5.2. After the initial transient, the dissipation rate oscillates around the mean value, consistent with the expected behavior in turbulent flows.

The chapter is divided in three sections: Section 5.1 discusses the flow field results, Section 5.2 focuses on scalar transfer results and Section 5.3 compares the flow and scalar fields.

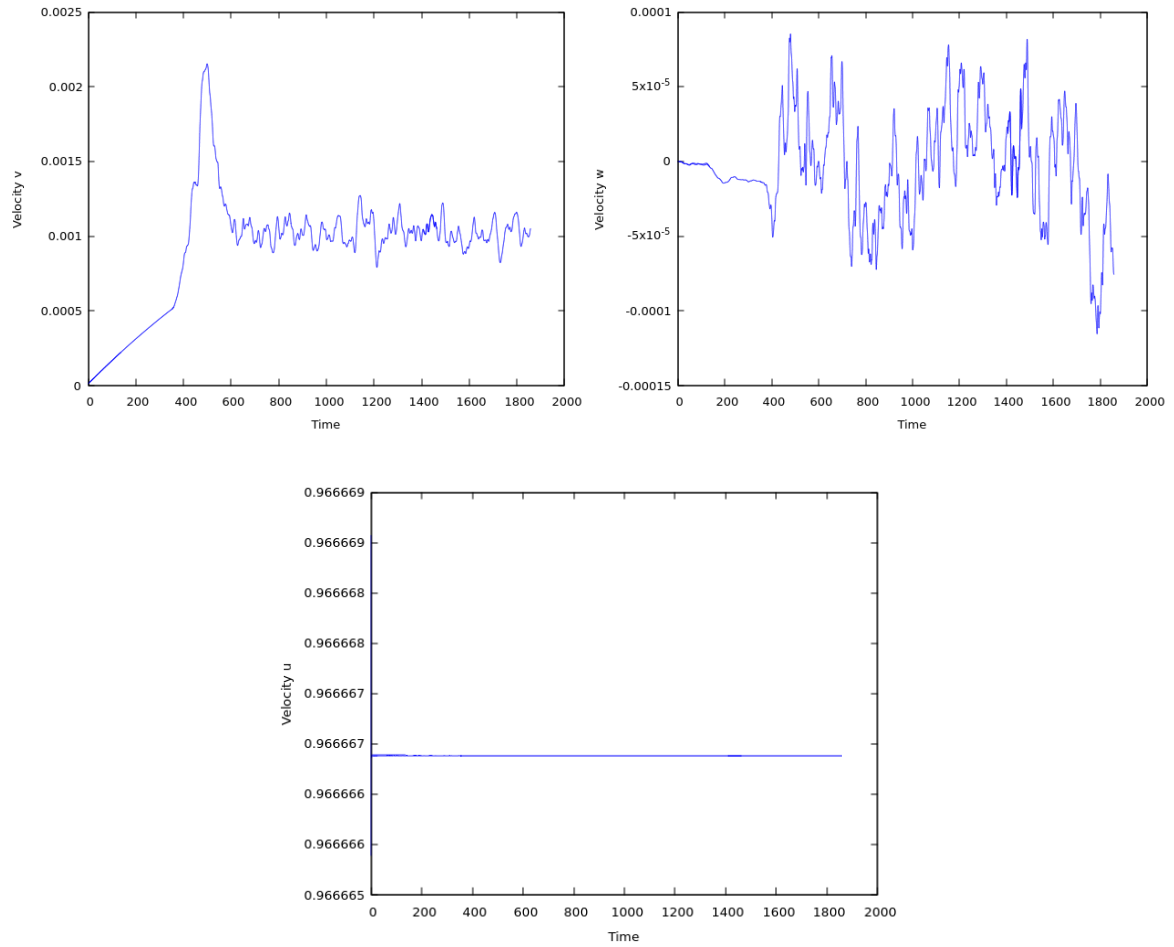


Figure 5.1: Mean velocity components over time, where each component is integrated over the entire volume and normalized by the volume itself.

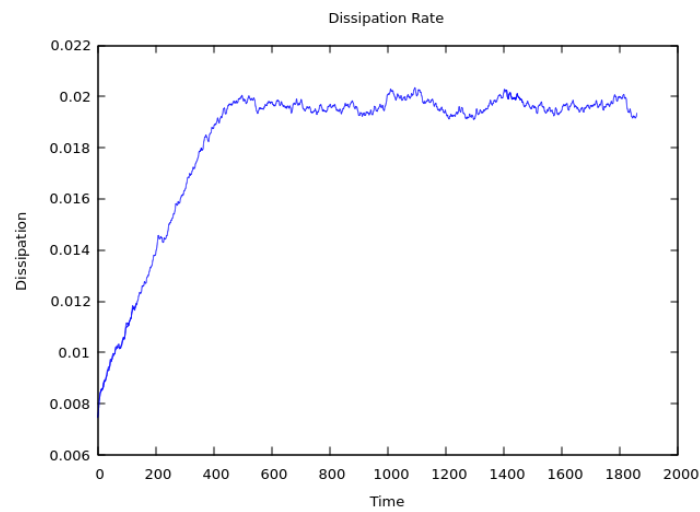


Figure 5.2: Dissipation rate of turbulent kinetic energy

5.1 Flow Field

This section presents the resolution of the computational domain and the hydrodynamic results obtained from the DNS, which are compared at the same Reynolds numbers rather than at the same downstream positions, as different experiments and simulations have different flow conditions. The Reynolds numbers used in this study are summarized in Table 4.1. Before analyzing the simulation data, it is essential to verify the correctness of the setup. According to the definition of the boundary layer, the free-stream velocity should be constant along the domain, and the case analyzed should exhibit a zero pressure gradient. As shown in Figure 5.3, the free-stream velocity is not constant along the streamwise coordinate. This variation occurs due to the slip boundary condition imposed at the upper boundary, which accelerates the flow, resulting in a 3% difference along the domain. Regarding the pressure, a coefficient is defined as:

$$\beta = \frac{\delta^*}{\tau_w} \frac{dp}{dx}$$

which accounts for the pressure gradient. It is shown that this coefficient is not equal to zero, especially in the region where the force is applied. The influence of the force diminishes along x , but the influence of the upper boundary condition and of the condition imposed over the pressure at the outlet can be seen.

The discrepancies from the theoretical trend, primarily due to the imposed boundary conditions, are the main reasons for the differences observed in comparison with other experimental and computational results. These comparisons are presented in the following sections.

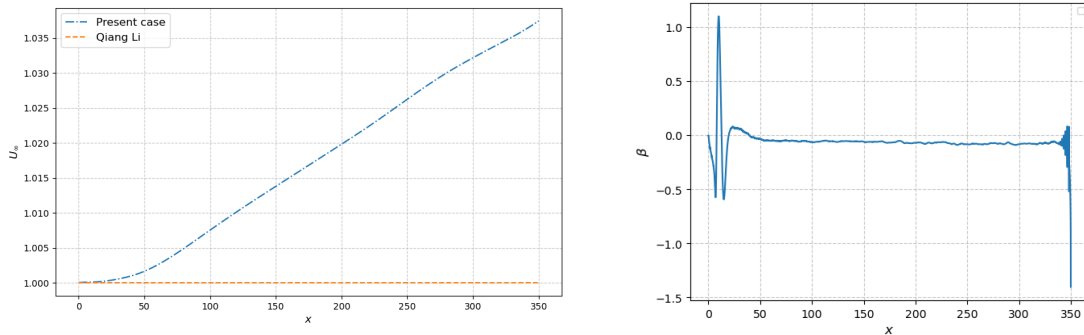


Figure 5.3: Variation of the free-stream velocity U_∞ and β with downstream positions.

5.1.1 Kolmogorov Length Scale

The Kolmogorov length scale, denoted as η , represents the smallest scale in turbulent flow where viscosity dominates and the turbulence kinetic energy is dissipated into thermal energy. This scale is crucial in understanding the dissipation of energy in turbulent flows and is given by the formula:

$$\eta = \left(\frac{\nu^3}{\varepsilon_k} \right)^{1/4}$$

where:

- ν is the kinematic viscosity of the fluid.
- ε_k is the average rate of dissipation of turbulence kinetic energy per unit mass (3.1.1).

In Direct Numerical Simulation (DNS), the mesh size Δ must be fine enough to capture the smallest eddies, which means it should be comparable to the Kolmogorov length scale η . This ensures that the simulation can resolve the smallest scales of turbulence and accurately model the dissipation of energy.

In the present simulation, as shown in Figure 5.4, the value of $\frac{\Delta}{\eta}$ is less than 2.2 throughout the entire domain, except in the forcing region, where the dissipation rate is slightly higher due to the tripping mechanism, and in the buffer region, where the energy dissipation rate is higher, leading to a smaller Kolmogorov length scale. This trend is also evident in Figure 5.5, where the wall-normal variation reflects the GLL distribution within the elements (see 4.3). Although the wall-normal values exceed the Kolmogorov length scale, they remain within acceptable limits, indicating that a sufficient number of grid points have been used.

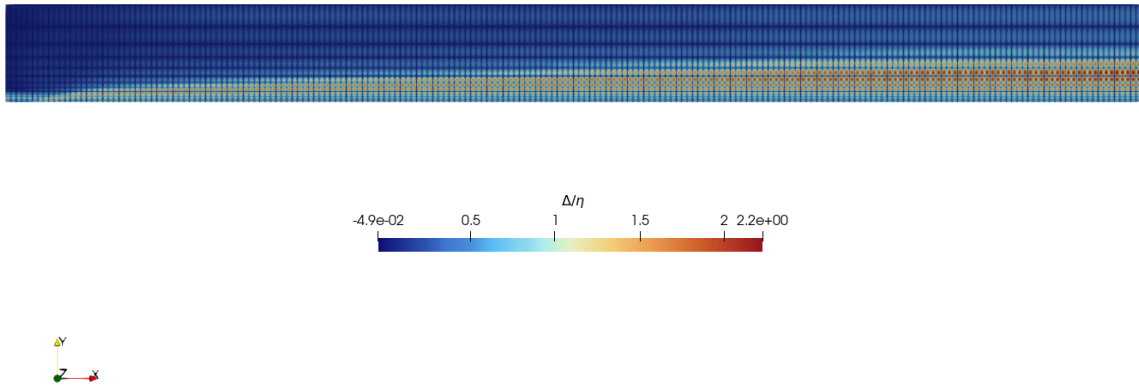


Figure 5.4: Kolmogorov length scale divided by the mesh size in the entire domain. Note: the value is above η only in the region where the influence of the tripping force is high and within the boundary layer.

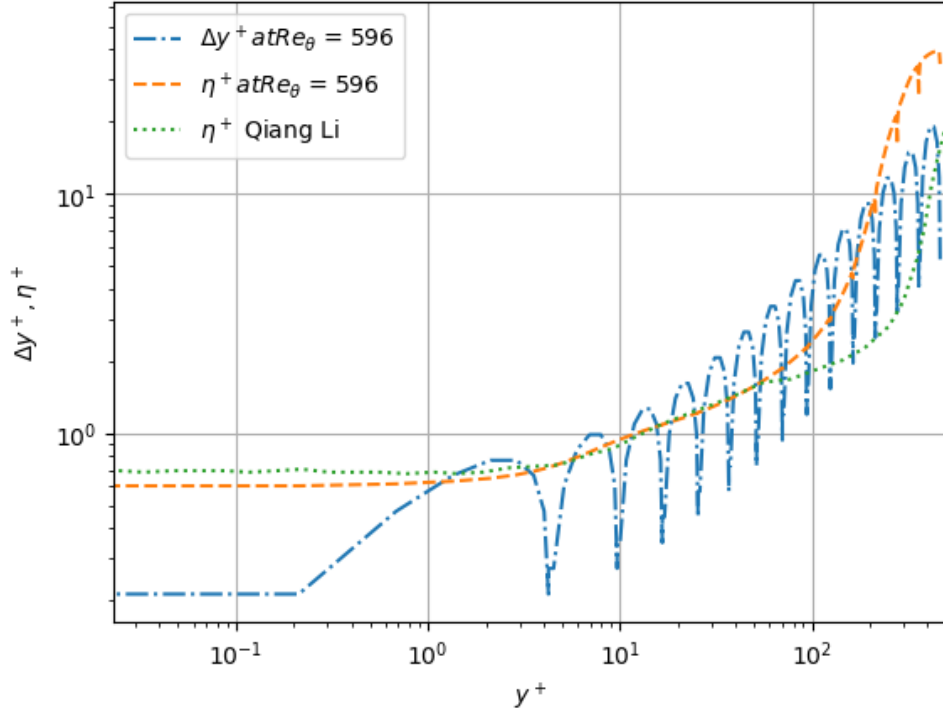


Figure 5.5: Resolution check: Wall-normal resolution Δy^+ , Kolmogorov length scale η^+ in the simulation and from Li et al. [28]. Note: Δy and η are divided by $\frac{u_\tau}{\nu}$ to make the variables dimensionless

5.1.2 Boundary Layer Thickness

In this section, we present the results of the simulation concerning boundary layer thickness, specifically focusing on displacement thickness and momentum thickness along the streamwise coordinate as shown in Figure 5.6. The displacement thickness δ^* represents the distance by which the external flow is displaced due to the boundary layer and reads as:

$$\int_0^\infty \left(1 - \frac{\langle u \rangle}{U_\infty}\right) dy$$

The momentum thickness represents the thickness of a hypothetical layer with uniform velocity that has the same momentum deficit as the actual boundary layer and is defined as:

$$\int_0^\infty \frac{\langle u \rangle}{U_\infty} \left(1 - \frac{\langle u \rangle}{U_\infty}\right) dy$$

The two can be considered as representative length of the problem, that means specific Reynolds number can be defined: the Reynolds number based on displacement thickness Re_{δ^*} and the Reynolds number based on momentum thickness Re_θ . The two values are plotted against the Reynolds number based on streamwise position Re_x , as shown in Figures 5.7.

The results are compared with those of Li et al. [28], and the agreement is partial. Figures 5.7 illustrate that Re_{δ^*} follows the same trend as the reference case, although

the Reynolds numbers differ at the same positions. The two Reynolds numbers, Re_{δ^*} and Re_x , exhibit opposite influences due to the free stream velocity increasing in the streamwise direction. Despite this, the overall trend remains consistent.

To validate the results of simulations and compare with the results in literature, a coefficient based on both thicknesses of the boundary layer can be constructed. A factor, called shape factor can be defined as:

$$H = \frac{\delta^*}{\theta}$$

that also accounts for the flatness of the mean velocity as seen in Figure 5.12, since in a turbulent boundary layer, the velocity profile near the wall is more uniform, exhibiting a steeper gradient and indicating that the momentum thickness grows more quickly than the displacement thickness. A smaller shape factor indicates that the mixing and momentum transfer within the turbulent boundary layer are increased, resulting in a flatter velocity profile close to the wall. Normally for the Blasius laminar profile its value is $H = 2.59$ and it goes to $H = 1.38$ for a fully turbulent flow with high Reynolds number. The trend of the shape factor is shown in Figure 5.8 and is compared with the data from Li et al. [28] and the experimental data from Roach and Brierley [57]. The shape factor value is slightly higher than that of Li et al. [28], indicating that the flow is less turbulent. Additionally, the domain length in the streamwise direction is not sufficiently large to allow the flow to develop properly. The agreement with the experimental data is getting closer as the flow reaches the fully turbulent region.

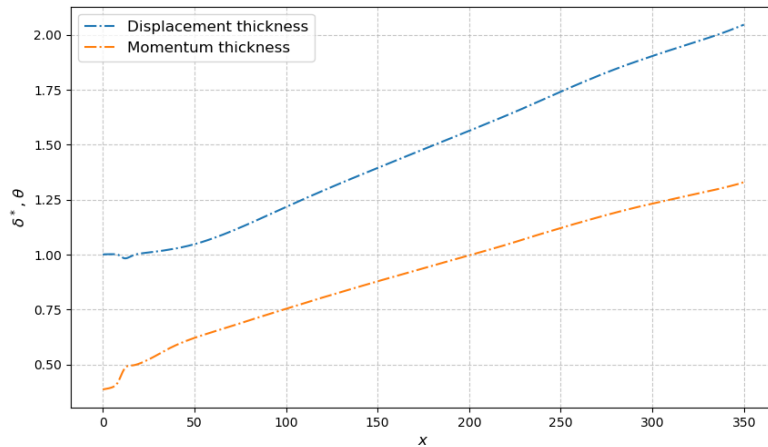


Figure 5.6: Displacement thickness and momentum thickness, measures of the boundary layer thickness versus the downstream positions.

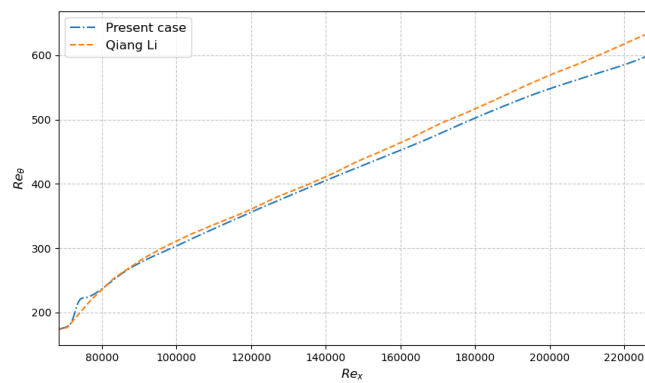
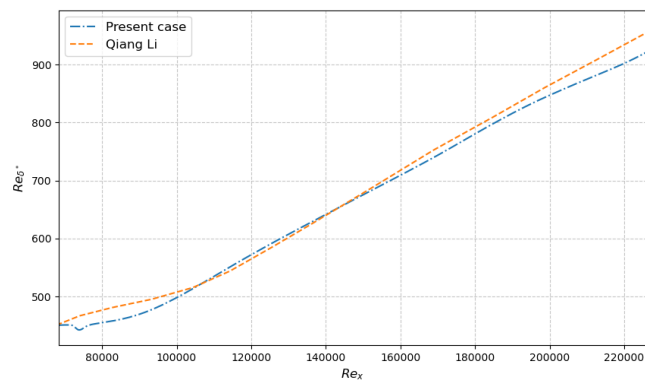


Figure 5.7: Reynolds number based on displacement Re_{δ^*} and momentum thickness Re_{θ} versus Reynolds number based on downstream positions Re_x .

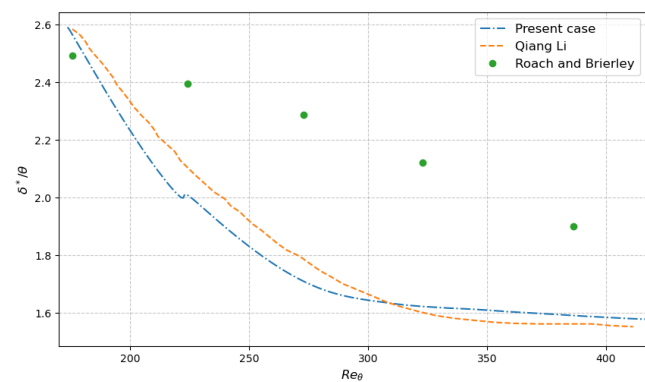


Figure 5.8: Variation of the shape factor with the downstream positions.

5.1.3 Outer Layer

As described in Chapter 3, the outer layer is the upper part of the boundary layer. In Figure 5.9, the mean streamwise velocity profiles at several downstream positions are

plotted in outer scaling. For outer scaling, the mean streamwise velocity u is scaled by the free-stream velocity U_∞ , and the wall-normal distance y is scaled by the local displacement thickness δ^* . It is shown that the profile does not change significantly with the Reynolds number, and all three curves collapse within each other.

The root-mean-square (RMS) values of the velocity and pressure fluctuations, as well as the Reynolds shear stress normalized by the free-stream velocity U_∞ , are shown in Figure 5.10. The wall-normal distance y is normalized by the outer scale δ^* . The agreement with the results from Li et al. [28] is quite good for the streamwise velocity, and there is almost no Reynolds effect. However, for the spanwise component, the wall-normal component, the pressure fluctuations and the shear stress the peak values of the RMS values decrease with a higher Reynolds number, and the peak positions move towards the wall. For the pressure fluctuations, it can be clearly seen that the influence of the upper boundary is more significant than in the simulation of Li et al. [28], because the height of the domain is not sufficient for the imposed boundary condition. As the flow moves further downstream from the inlet, the velocity profiles at different Reynolds numbers tend to collapse onto a single curve. This indicates that the flow is becoming fully developed, meaning that the effects of the initial conditions and transient behaviors diminish, and the flow reaches a statistically steady state where the profiles are self-similar.

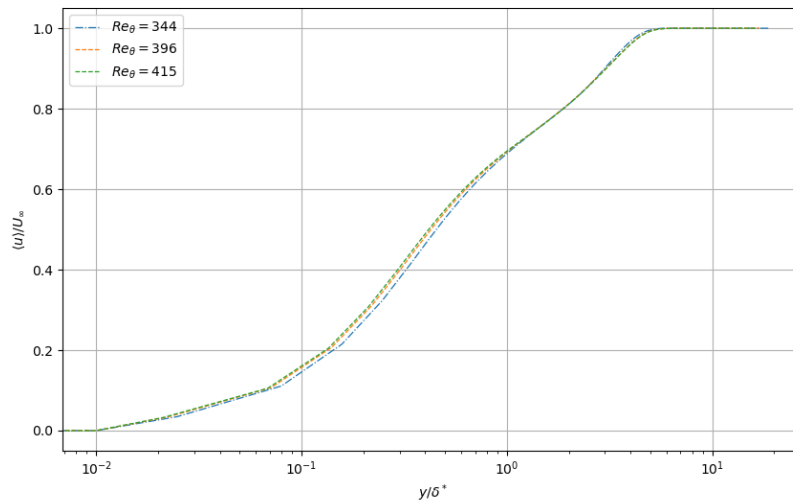


Figure 5.9: Mean streamwise velocity profile at different downstream positions in outer scaling.

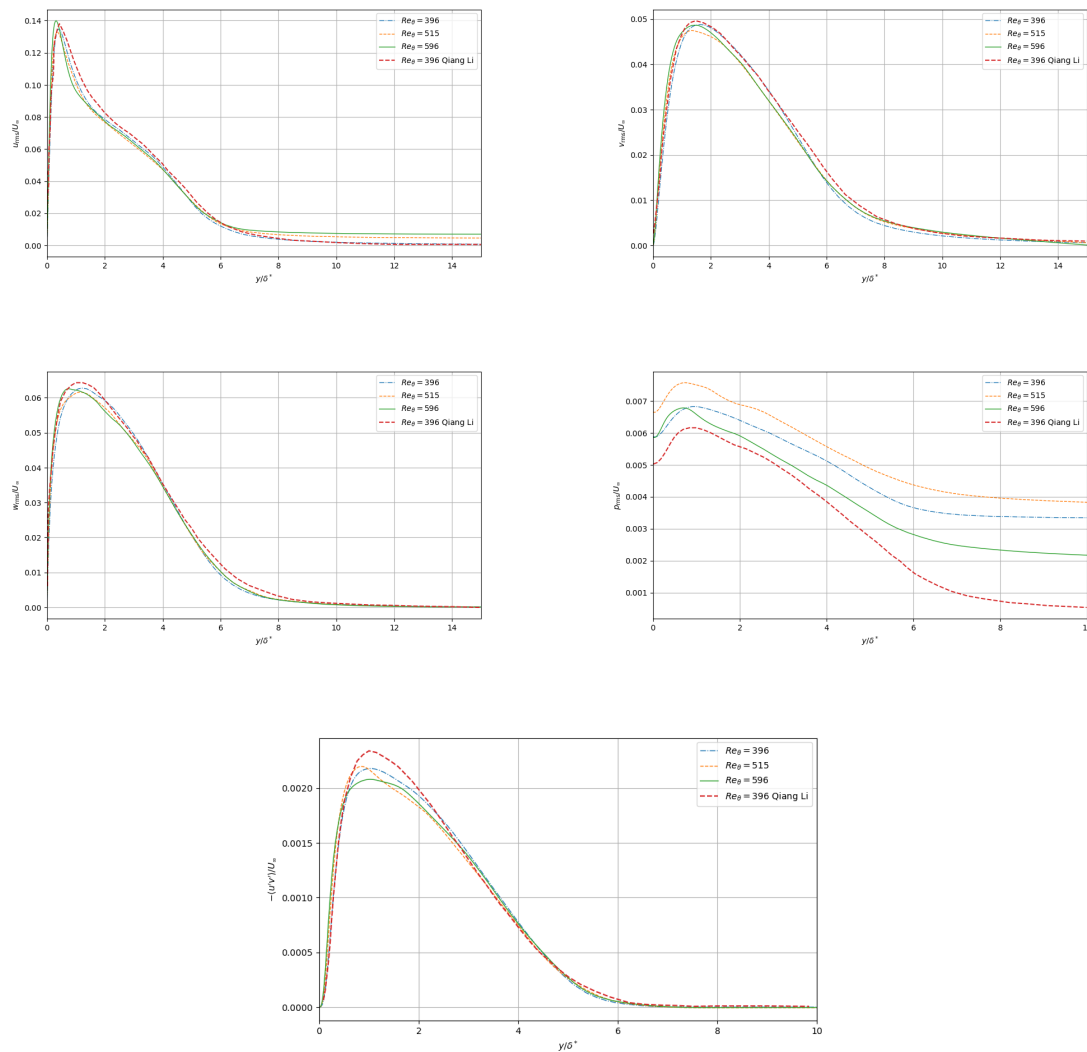


Figure 5.10: RMS values of the velocity, pressure fluctuations and Reynolds shear stress versus downstream positions in outer scaling.

5.1.4 Inner Layer

As described in Chapter 3, the inner layer is the region close to the wall. In Figure 5.11, the mean streamwise velocity profiles at several downstream positions are plotted in inner scaling. In this scaling, the mean streamwise velocity u is normalized by the friction velocity u_τ , and the wall-normal distance y is normalized by ν/u_τ , where ν is the kinematic viscosity and u_τ is the friction velocity.

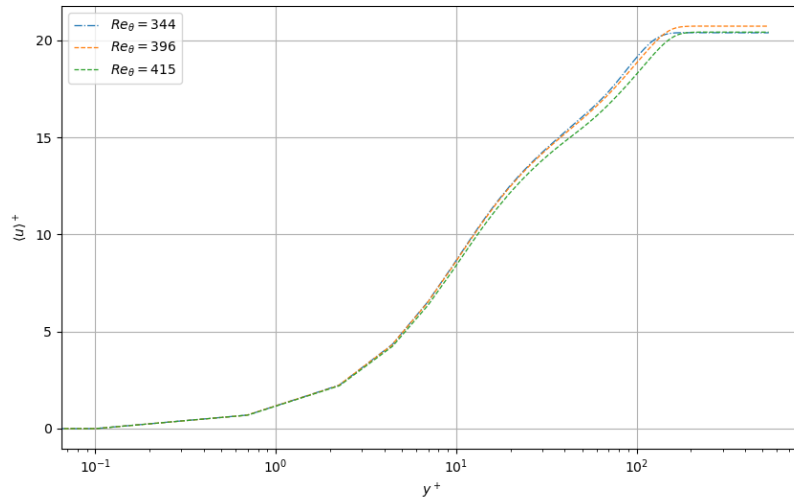


Figure 5.11: Mean streamwise velocity profile at different downstream positions in outer scaling.

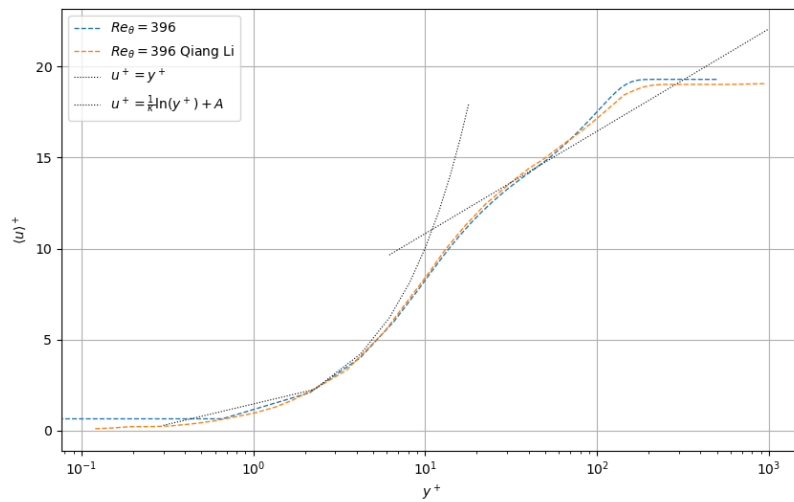


Figure 5.12: Mean streamwise velocity profile at different downstream positions in outer scaling.

Within the viscous sub-layer, the calculated mean velocity profile follows closely the linear relationship:

$$u^+ = y^+$$

Additionally, the profile at the final position aligns well with the classical logarithmic law:

$$u^+ = \frac{1}{\kappa} \ln y^+ + A,$$

where $\kappa = 0.41$ and $A = 5.2$, as illustrated in Figure 5.12. The wake region is also evident in this profile.

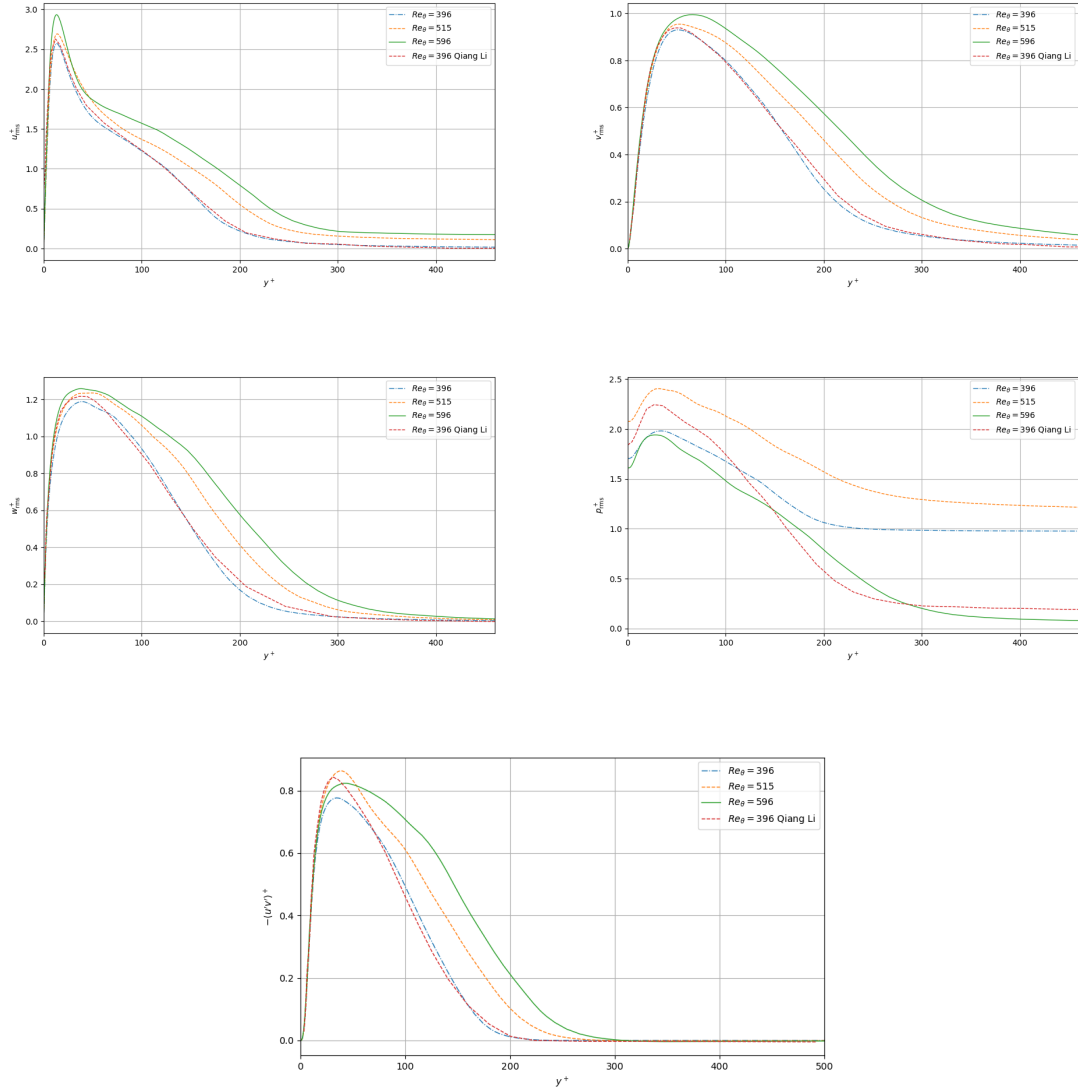


Figure 5.13: RMS values of the velocity, pressure fluctuations and Reynolds shear stress versus downstream positions in inner scaling.

Figure 5.13 presents the RMS values of the velocity and pressure fluctuations, as well as the Reynolds shear stress, all normalized by the friction velocity u_τ . The wall-normal distance y is normalized by the viscous scale ν/u_τ . The peak RMS values for all three velocity components, pressure fluctuations, and Reynolds shear stress increase with higher Reynolds numbers. Notably, the wall-normal and spanwise components, v_{rms} and w_{rms} , show more significant increases compared to the streamwise component u_{rms} . The peak value of the Reynolds shear stress $-u'v'$ also rises, with the peak position moving further from the wall as the Reynolds number increases. The influence of the averaging time is evident in this case, as the curve with the highest Reynolds number does not follow the expected trend. This discrepancy occurs because the

averaging period was insufficient for the flow to fully develop till the end. The RMS values of the velocity fluctuations are more sensitive to Reynolds effect than the mean velocity profiles, as can be seen clearly in the case of p_{rms} in Figure 5.13.

5.1.5 Skin Friction

Skin friction is a measure of the drag force exerted by the fluid on the surface due to the viscosity of the fluid. It is quantified by the skin friction coefficient c_f , which is defined as:

$$c_f = \frac{\tau_w}{\frac{1}{2}\rho U_\infty^2}$$

where τ_w is the wall shear stress, ρ is the fluid density, and U_∞ is the free stream velocity.

The evolution of the skin friction coefficient c_f is shown in Figure 5.14. The upper dashed line represents the turbulent solution provided by Kays and Crawford [58], given by:

$$c_f = 0.025Re_\theta^{-\frac{1}{4}}$$

For comparison, empirical formulas from Schoenherr [59] are also included:

$$c_f = 0.31(\ln^2(2Re_\theta) + 2\ln(2Re_\theta))^{-1}$$

A step increase in the skin friction coefficient can be observed in the forcing region due to the introduced high-frequency perturbation. In the simulation by Li et al. [28], a similar bump is present but appears smoother because the forcing region is extended over a larger length and the applied force is weaker than in the present case.

The computed skin friction initially exhibits laminar behavior, as the Blasius profile is present at the inlet. This is followed by a transient phase that leads to weakly turbulent behavior.

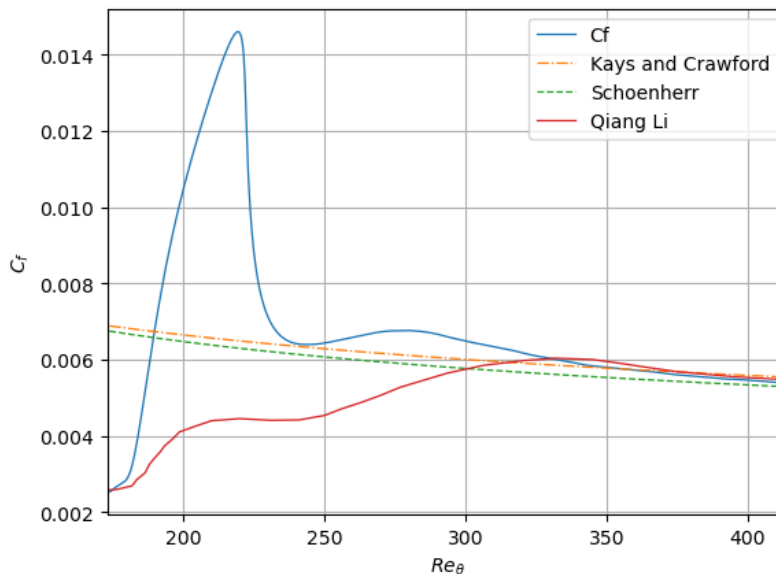


Figure 5.14: Skin friction coefficient c_f versus the Reynolds number based on the momentum thickness Re_θ

5.1.6 Probability Density Function

Stochastic methods use distribution functions to describe fluctuating scalars in a turbulent field. The probability density function (PDF) is defined as:

$$P(\Phi) = \frac{dF_\phi(\Phi)}{d\Phi} \quad (5.1)$$

In this study, the PDF was computed for the velocity component fluctuations u' , v' , and w' . The velocity fluctuations are normalized by their corresponding RMS values, and the probability density distributions are normalized such that the area under each curve is unity. A Gaussian distribution with zero mean and matching variance is used as a reference.

For u' , the PDF shows (Figure 5.15) that close to the wall, the distribution is positively skewed, indicating that the fluctuations are more intense in the positive direction due to sweep motions. Around $y^+ \approx 10$, the distribution becomes nearly Gaussian, reflecting a balance between positive and negative fluctuations. Further away from the wall, the distribution becomes negatively skewed, indicating stronger negative fluctuations, possibly due to ejection motions. These observations are expected because near the wall, the shear forces create coherent structures such as streamwise vortices and streaks, leading to intense sweep and ejection motions.

For the v' component, the PDF (Figure 5.16) is slightly negatively skewed in the near-wall region, suggesting that downward fluctuations are more intense. As we move away from the wall, the distribution becomes positively skewed, indicating stronger upward fluctuations. This behavior is expected because near the wall, the interaction with the wall restricts upward motions, making downward fluctuations more intense. As the distance from the wall increases, this restriction diminishes, allowing upward fluctuations to dominate.

For the w' component, the PDF (Figure 5.17) is slightly negatively skewed near the wall and alternates between positive and negative skewness further away. The distribution is almost Gaussian but with a pronounced peak at the mean (zero), indicating that the fluctuations are centered around the mean value with occasional deviations.

The behavior of these components is consistent with the dynamics of turbulent boundary layers and the interaction of coherent structures with the wall.

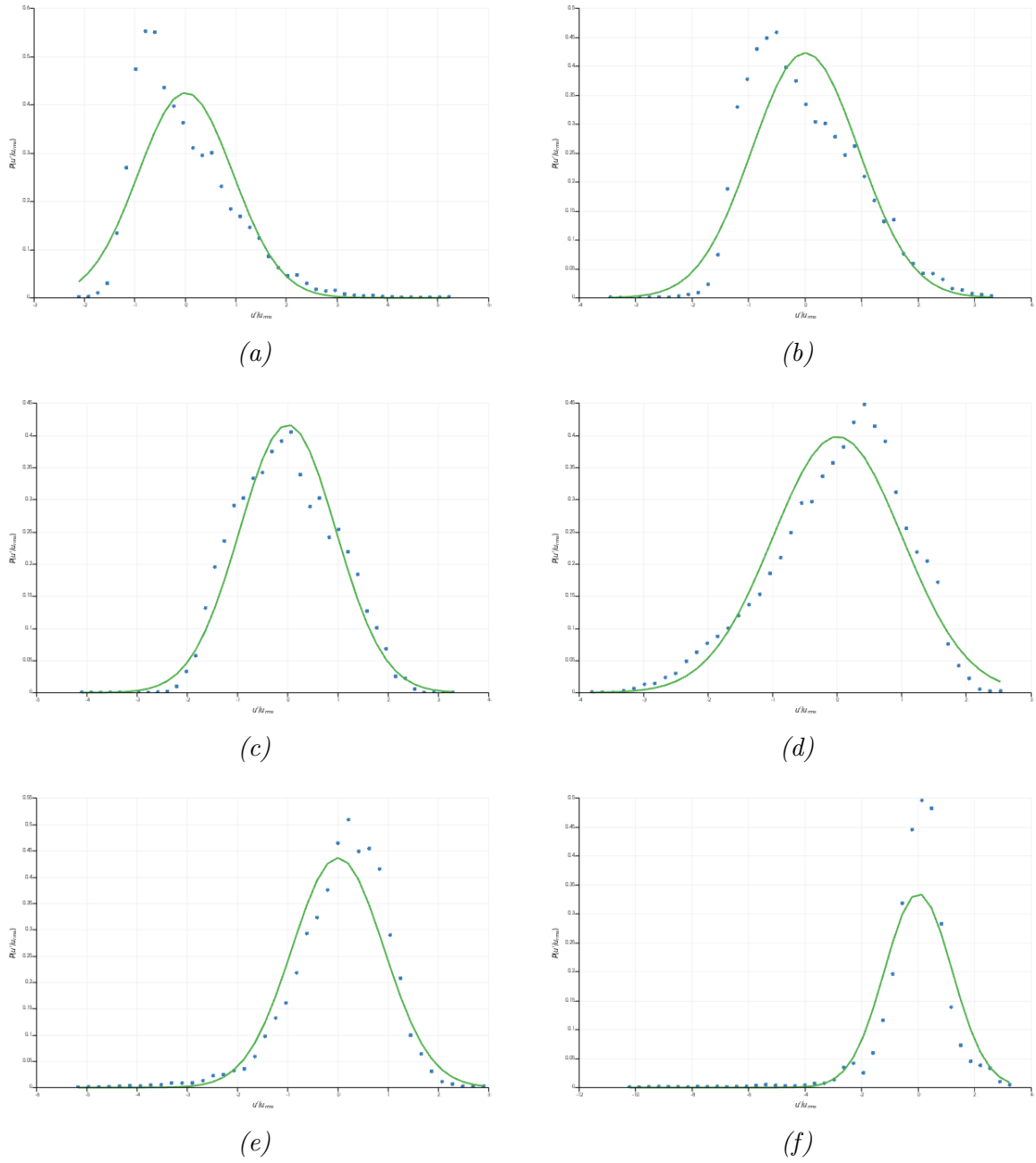


Figure 5.15: PDF of u' at different y^+ position: (a) $y^+ = 1.57$ $S(u') = 1.01$, (b) $y^+ = 4.86$ $S(u') = 0.58$, (c) $y^+ = 9.72$ $S(u') = 0.15$, (d) $y^+ = 30.2$ $S(u') = -0.50$, (e) $y^+ = 48.5$ $S(u') = -0.86$, (f) $y^+ = 95.3$ $S(u') = -1.98$.

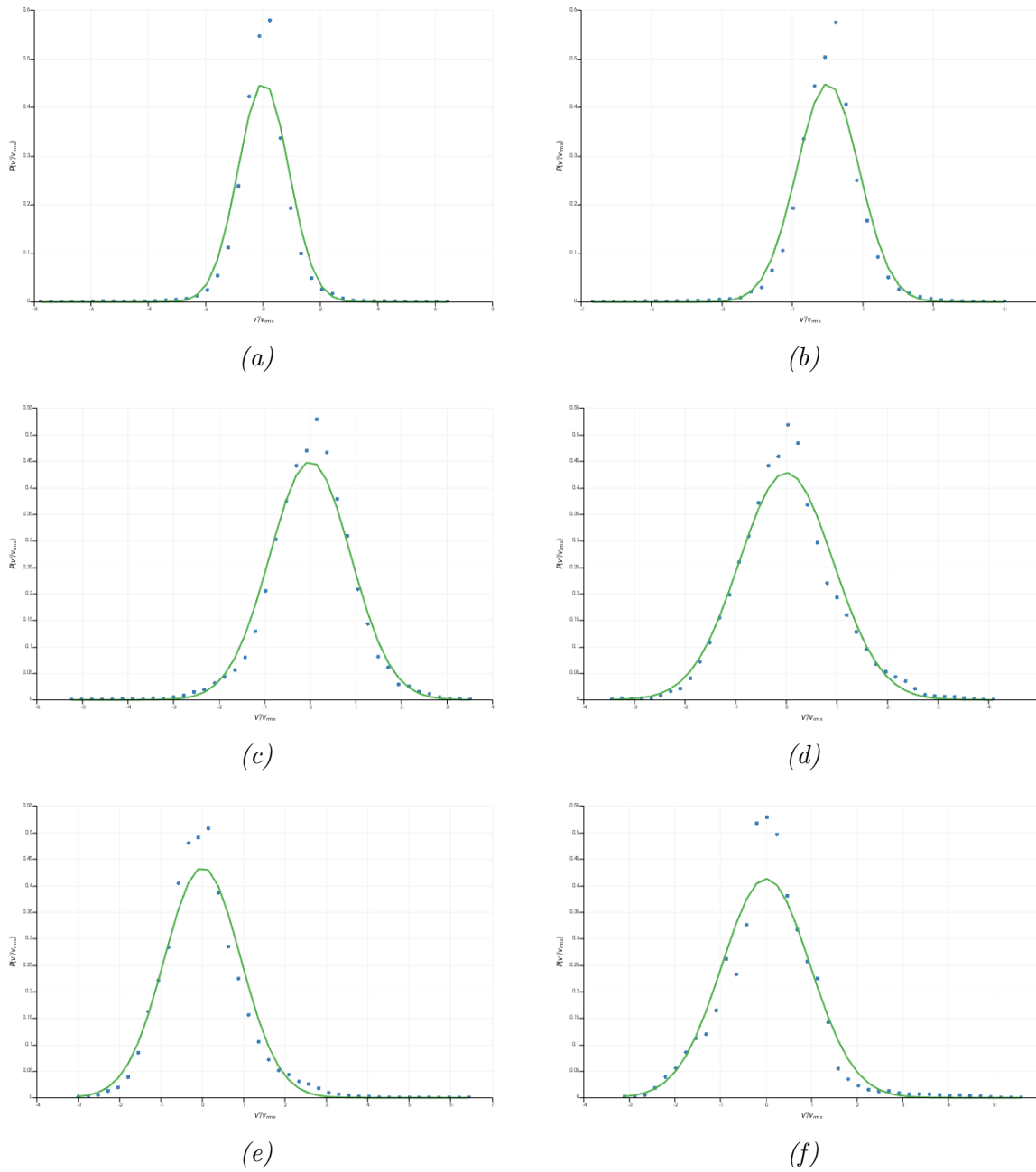


Figure 5.16: PDF of v' at different y^+ position: (a) $y^+ = 1.57$ $S(v') = -0.25$, (b) $y^+ = 4.86$ $S(v') = -0.32$, (c) $y^+ = 9.72$ $S(v') = -0.34$, (d) $y^+ = 30.2$ $S(v') = 0.31$, (e) $y^+ = 48.5$ $S(v') = 0.62$, (f) $y^+ = 95.3$ $S(v') = 0.43$.

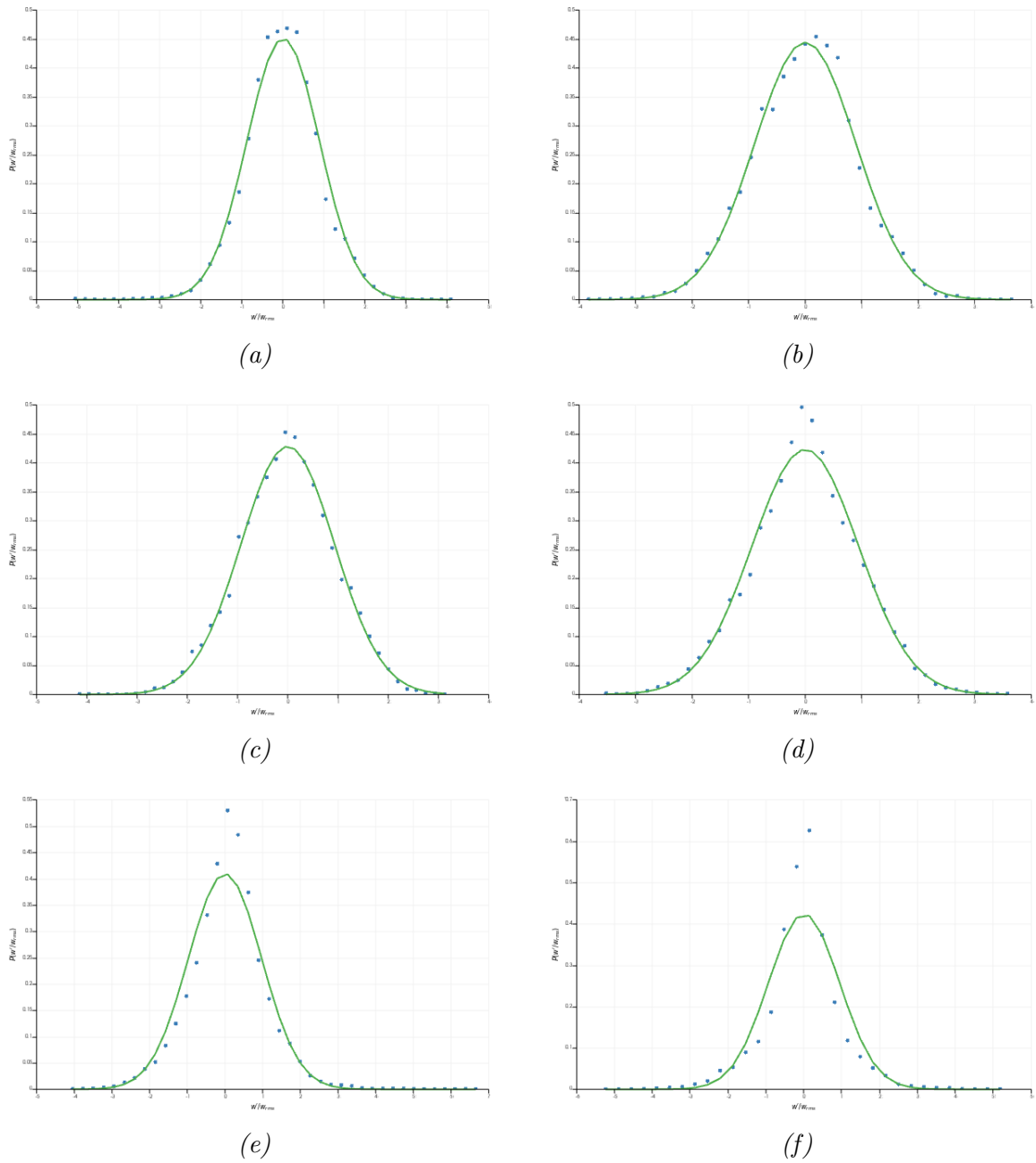


Figure 5.17: PDF of w' at different y^+ position: (a) $y^+ = 1.57$ $S(w') = -0.16$, (b) $y^+ = 4.86$ $S(w') = -0.077$, (c) $y^+ = 9.72$ $S(w') = -0.071$, (d) $y^+ = 30.2$ $S(w') = -0.03$, (e) $y^+ = 48.5$ $S(w') = 0.17$, (f) $y^+ = 95.3$ $S(w') = -0.08$.

5.1.7 Energy Spectrum of Turbulence

Turbulent flow is characterized by chaotic and irregular fluid motion, occurring over a wide range of length scales. The energy spectrum, $E(k)$, is a fundamental tool used to analyze the distribution of kinetic energy across different scales in turbulent flow. It represents the contribution to turbulence kinetic energy by wavenumbers from k to $k + dk$. The largest eddies have low wavenumbers, while the smallest eddies have high wavenumbers.

In this study, the energy spectrum is examined at a specific Reynolds number, $Re_\theta = 319$, and at three different wall-normal distances, y^+ , corresponding to the viscous sublayer ($y^+ = 2.5$), buffer layer ($y^+ = 22.8$), and log region ($y^+ = 154.5$). These regions are crucial for understanding the behavior of turbulent flow near a wall.

The energy spectrum is calculated using the Fourier transform of the velocity field. The formula for the energy spectrum $E(k)$ is given by:

$$E(k) = \sum_i |\hat{u}_i(k)|^2$$

where $\hat{u}_i(k)$ are the Fourier coefficients of the velocity components.

To ensure the consistency of the energy spectrum along the spanwise direction, spectra at fixed y^+ for two different z positions are compared in Figure 5.18. This comparison demonstrates that the energy spectrum remains unchanged along the spanwise direction, indicating homogeneity in this direction.

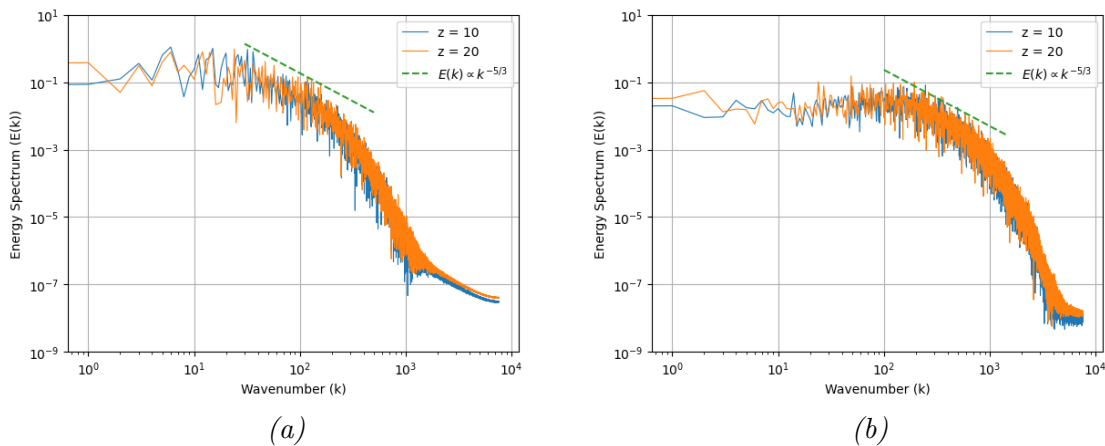


Figure 5.18: Energy spectra for two spanwise positions at $Re_\theta = 396$ and (a) $y^+ = 2.5$ (b) $y^+ = 154.5$

Subsequently, spectra at the same y^+ but at different streamwise positions, corresponding to different Reynolds numbers, are compared, to observe the Reynolds effect (Figure 5.19). As the Reynolds number increases, the flow becomes more turbulent, which is evident from the different energy levels and the slight rightward shift of the curve. However, the differences are not highly noticeable because the range of Re_θ is small, making the variations barely visible.

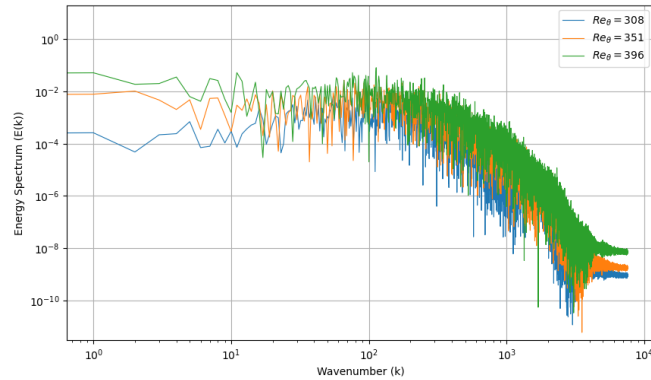


Figure 5.19: Comparison of energy spectra for at $Re_\theta = 308$, $Re_\theta = 351$ and $Re_\theta = 396$ for $y^+ = 154.5$

5.1.8 Reynolds Stress Anisotropy

Understanding the departure from isotropy is essential, when modeling the Reynolds stress tensor and that is the main reason anisotropy invariant maps (AIMs) are valuable tools able to quantify the degree of anisotropy in turbulent flows. These maps represent a domain within which all realizable Reynolds stress invariants must lie. The AIM, proposed by Lumley and Newman [60], helps in characterizing different states of turbulence by plotting invariants II_a and III_a .

The Reynolds stress anisotropy is defined by the anisotropy tensor a_{ij} , derived from the Reynolds stress tensor R_{ij} , the turbulent kinetic energy k , and the Kronecker delta δ_{ij} :

$$a_{ij} = \frac{R_{ij}}{k} - \frac{2}{3}\delta_{ij}$$

The anisotropy tensor has zero trace, meaning $a_{ii} = 0$, and the two non-zero invariants, II_a and III_a , are defined as:

$$II_a = a_{ij}a_{ji}$$

$$III_a = a_{ij}a_{jk}a_{ki}$$

The AIM can also be described using variables η and ζ , where:

$$6\eta^2 = 2II_a$$

$$6\zeta^3 = 3III_a$$

Characteristic states of turbulence are represented by specific points and lines on the AIM, such as isotropic turbulence at the origin $(0, 0)$, isotropic two-component turbulence in the right corner, and one-component turbulence in the left one. The upper boundary line of the AIM represents two-component turbulence, typically observed near solid walls where the wall-normal component of the fluctuations diminishes faster than the other components (see Djordje Novkovic and Radojkovic [61]).

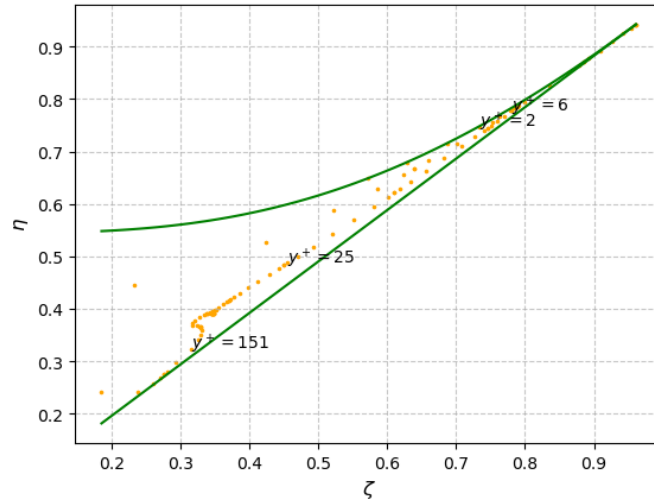


Figure 5.20: Anisotropy invariant map at $Re_\theta = 596$ against wall normal position y^+ .

The AIM of this simulation at $Re_\theta = 596$ is shown in Figure 5.20. Close to the wall, at $y^+ = 2$, the turbulence is very near the two-component limit. As we move away from the wall, at $y^+ = 6$, the turbulence approaches the one-component limit near the edge of the viscous sub-layer. This indicates that one of the diagonal components of the Reynolds stress tensor becomes significantly larger than the other two, which are nearly zero. Further from the wall, at $y^+ = 25$, the turbulence is closer to the isotropic state and lies within the axisymmetric expansion line and the two-component turbulence line. This suggests that at this wall-normal position, the flow is in an intermediate state, such as the buffer layer. At $y^+ = 151$, in the log region, the turbulence is close to the bottom curve corresponding to axisymmetric expansion, where one diagonal component of the Reynolds stress tensor is larger than the other two. These results align with the ones of Li et al. [28], including the agglomeration of points close to $y^+ = 150$.

5.2 Scalar Field

In this chapter, the transport of 30 different scalars is simulated, each with either a distinct Prandtl number or wall-boundary condition and the results presented are averaged in the spanwise direction. All the scalars are summarized in Table 1.1. Special attention is given to the comparison between scalars with Prandtl numbers close to unity and those with values typical of liquid metals. Additionally, the range of Prandtl numbers from 0.1 to 0.3 is of particular interest, as a change in behavior is expected within this range, which will be demonstrated in the results. Furthermore, comparisons between isothermal and isoflux wall boundary condition cases are also presented. All the scalars are transformed from θ to $1 - \theta$ to simulate a cooling wall.

5.2.1 Boundary Layer Thickness

The scalar displacement thickness, denoted as δ_θ^* , quantifies the effective displacement of the external scalar concentration profile due to the presence of the boundary layer. Mathematically, it is expressed as:

$$\delta_\theta^* = \int_0^\infty \left(1 - \frac{\theta - \theta_w}{\theta_\infty - \theta_w} \right) dy$$

where θ represents the scalar concentration, θ_w is the scalar concentration at the wall, and θ_∞ is the scalar concentration in the freestream.

The scalar momentum thickness, denoted as θ_θ , represents the thickness of a hypothetical layer with uniform scalar concentration that would produce the same scalar momentum deficit as the actual boundary layer. This is defined by the integral:

$$\theta_\theta = \int_0^\infty \frac{\theta - \theta_w}{\theta_\infty - \theta_w} \left(1 - \frac{\theta - \theta_w}{\theta_\infty - \theta_w} \right) dy$$

The two measures of the thermal boundary layer thickness are shown in Figures 5.22 and 5.23 for various Prandtl numbers, ranging from $Pr = 1$ to $Pr = 0.0232$ (LBE). It is evident that the thickness is governed by the Prandtl number, resulting in a thermal boundary layer that is thicker than the velocity boundary layer for $Pr \ll 1$ and thinner for $Pr > 1$, as shown in Figure 5.21. From the Figure, it is clear that as the Prandtl number decreases, the boundary layer becomes more uniform. This effect is due to the increased thermal diffusivity relative to momentum diffusivity, allowing heat to spread more evenly through the fluid.

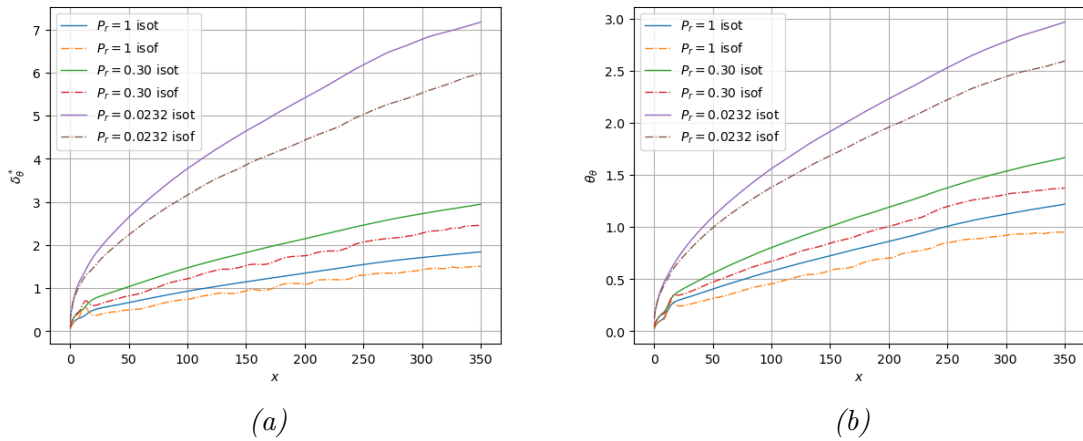


Figure 5.21: Comparison of boundary layer thickness for different scalars at $Re_\theta = 596$
 (a) Displacement thickness δ_θ^* (b) Momentum thickness θ_θ

Additionally, there is a significant difference between the cases with isothermal and isoflux wall boundary conditions. The boundary layer thickness profile appears less uniform for the isoflux case. This phenomenon can be explained by the nature of the boundary conditions: in the isothermal case, the wall temperature is constant, leading to a more consistent temperature distribution and a more regular boundary layer profile. In contrast, the isoflux condition involves a constant heat flux at the wall, which results in temperature fluctuations and a less consistent temperature distribution, thereby causing a less regular boundary layer profile and also a slightly thinner one (see Figure 5.21).

These observations highlight how both the Prandtl number and the boundary conditions influence the thermal boundary layer thickness profiles.

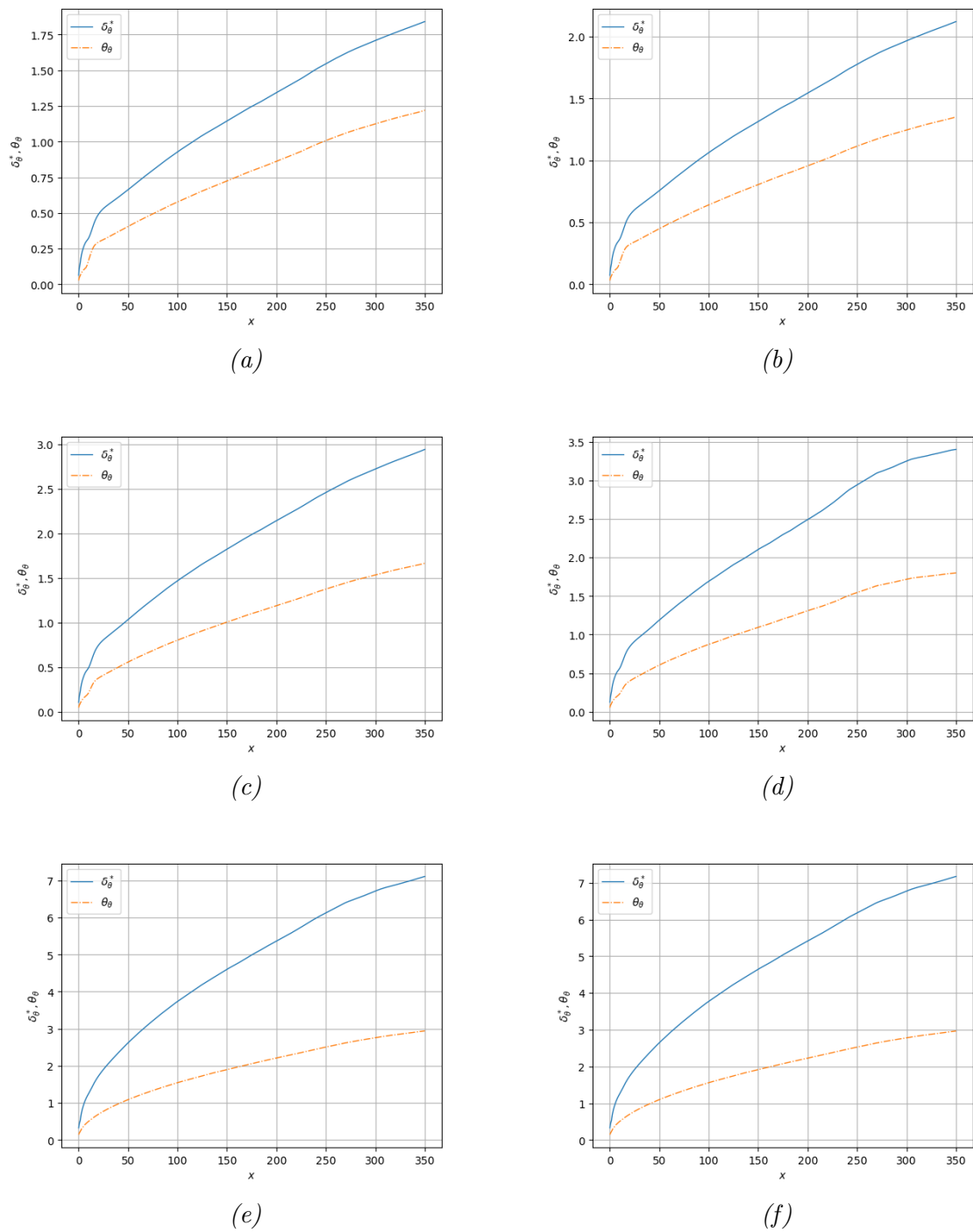


Figure 5.22: Different measures of the scalar boundary layer thickness versus the downstream positions for (a) $Pr = 1$, (b) $Pr = 0.71$, (c) $Pr = 0.30$, (d) $Pr = 0.20$, (e) $Pr = 0.0237$, (f) $Pr = 0.0232$ with isothermal boundary conditions.

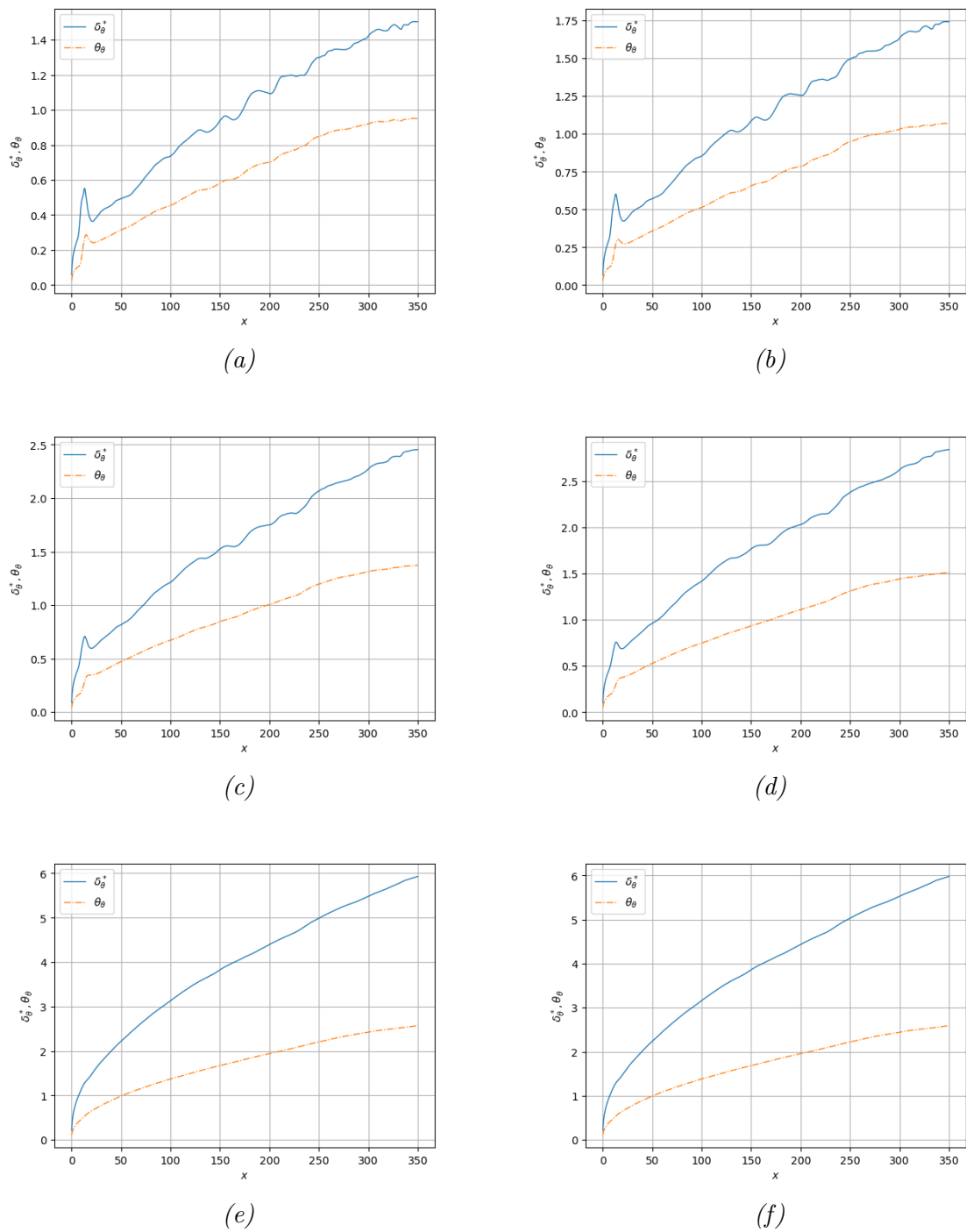


Figure 5.23: Different measures of the scalar boundary layer thickness versus the downstream positions for (a) $Pr = 1$, (b) $Pr = 0.71$, (c) $Pr = 0.30$, (d) $Pr = 0.20$, (e) $Pr = 0.0237$, (f) $Pr = 0.0232$ with isoflux boundary conditions.

5.2.2 Inner Layer

Mean scalar

The results of θ^+ against y^+ for different Prandtl numbers (Pr) at various downstream positions (Re_θ) provide insightful comparisons with the velocity field. Here, θ^+ represents the dimensionless mean scalar, normalized by the friction scalar θ_τ , and y^+ is the dimensionless wall-normal distance, scaled by the viscous length scale.

The mean scalar profiles for higher Pr numbers exhibit a clear logarithmic region, similar to the streamwise velocity profiles. However, as Pr decreases, the logarithmic region becomes less distinct due to the thickening of the conductive sub-layer, as shown in Figure 5.25, where the logarithmic region can be clearly observed only for Pr = 1. The comparison of the mean scalar profiles in Figure 5.24 clearly illustrates at which Prandtl number the logarithmic region disappears. This thickening effect is more pronounced at lower Pr values, leading to a broader scalar boundary layer. Consequently, the mean scalar value increases with decreasing Pr, indicating a thicker boundary layer, in complete accordance with Figure 5.21.

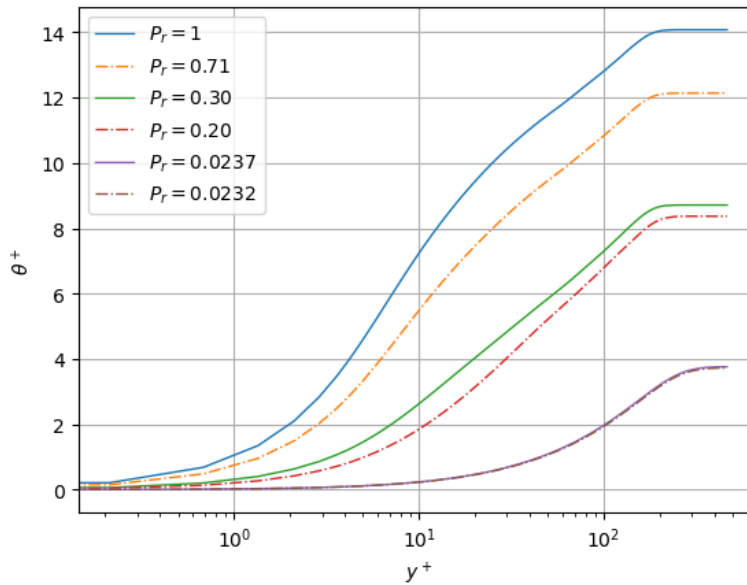


Figure 5.24: Comparison of mean scalar profile for various Prandtl numbers at $Re_\theta = 596$

For Pr = 1 (Figure 5.25a), it is observed that as the Reynolds number increases, the profiles of θ^+ become higher, indicating an increase in the mean scalar value. This trend is consistent across other Prandtl numbers, suggesting that higher Reynolds numbers lead to more efficient scalar transport due to increased turbulence.

However, an interesting behavior is noted for Pr = 0.2, where the departure from the lowest values starts earlier in the buffer region as Reynolds number increases. This early departure indicates that the scalar transport mechanisms are more active at lower y^+ values, leading to a more pronounced effect in the buffer region. This behavior is not observed for the lowest Pr corresponding to liquid metal Lead-Bismuth Eutectic

(LBE), but within the range of Pr 0.2-0.3, the behavior changes significantly. This suggests that within this Pr range, the interaction between molecular diffusion and turbulent transport is altered, affecting the scalar distribution earlier in the boundary layer.

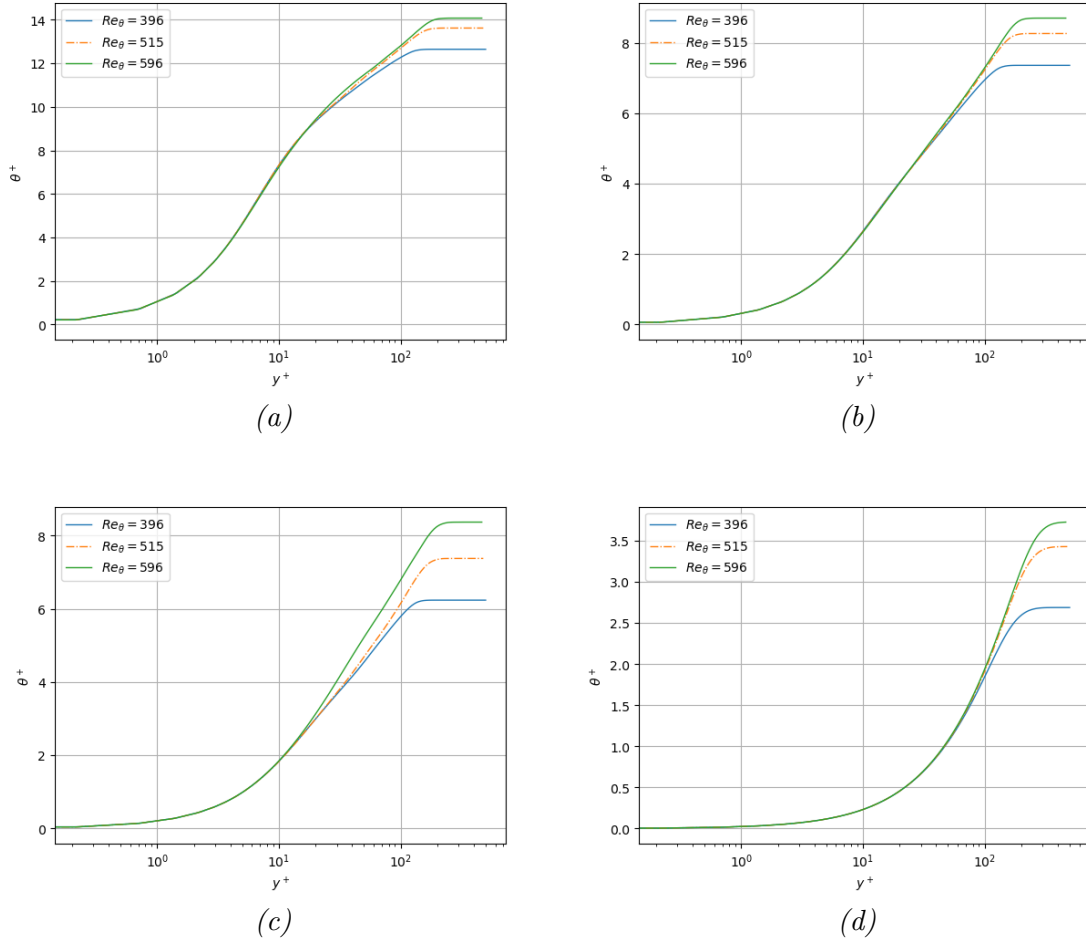


Figure 5.25: Mean scalar profiles at different downstream positions for (a) $Pr = 1$, (b) $Pr = 0.30$, (c) $Pr = 0.20$, (d) $Pr = 0.0232$ with isothermal wall-boundary conditions.

Turbulent statistics

The root-mean-square (RMS) values of the scalar fluctuations, normalized by the friction scalar θ_τ , are shown in Figures 5.27 and 5.28. The wall-normal distance is normalized by ν/u_τ . A first straightaway consideration is over the boundary condition: the RMS values at the wall are non-zero for the isoflux boundary condition, while they are zero for the isothermal boundary condition. This difference is due to the nature of the boundary conditions: the isothermal condition imposes a constant temperature at the wall, leading to zero fluctuations, whereas the isoflux condition allows temperature fluctuations at the wall.

The RMS values of θ are plotted at different streamwise positions to highlight the Reynolds effect. It can be seen that the effect becomes more significant as the Prandtl number decreases. For the isothermal boundary condition, the RMS values of

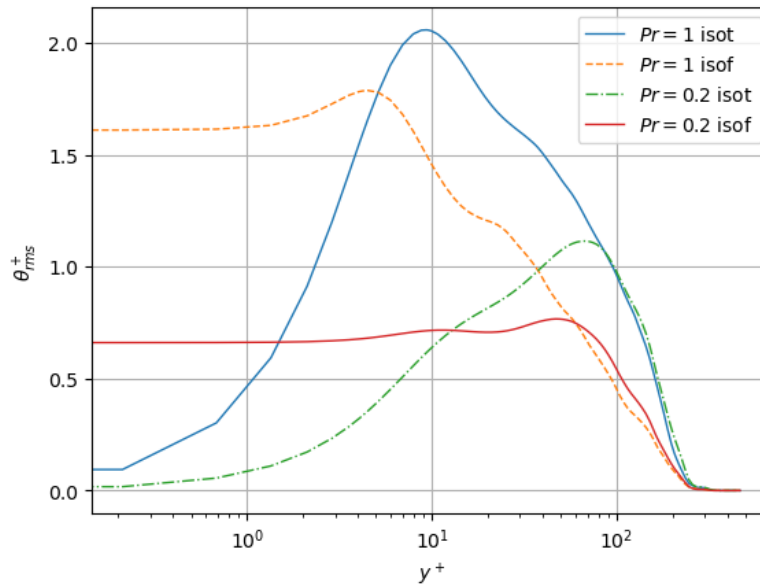


Figure 5.26: Comparison of scalars with different wall-boundary conditions, highlighting the behavior at the wall.

the scalar fluctuations with different Reynolds numbers collapse with each other for $y^+ \approx 10$. The peak values increase with an increase in the Reynolds number. In the outer region, the profiles of the RMS scalar fluctuations differ due to the Reynolds number effect, similar to the RMS values of the streamwise velocity. The maximum RMS values of the scalar fluctuation increase as the Prandtl number increases, as shown in Figure 5.26. The comparison of the RMS values at $Re_\theta = 596$ for various Prandtl numbers shows that the value is very high for $Pr = 1$ close to the wall and then rapidly decreases to zero. As the Prandtl number decreases, the maximum RMS value decreases, and the values approach zero more gradually. This behavior can be explained by the increased thermal diffusivity at lower Prandtl numbers, which leads to more uniform temperature distributions and less pronounced fluctuations.

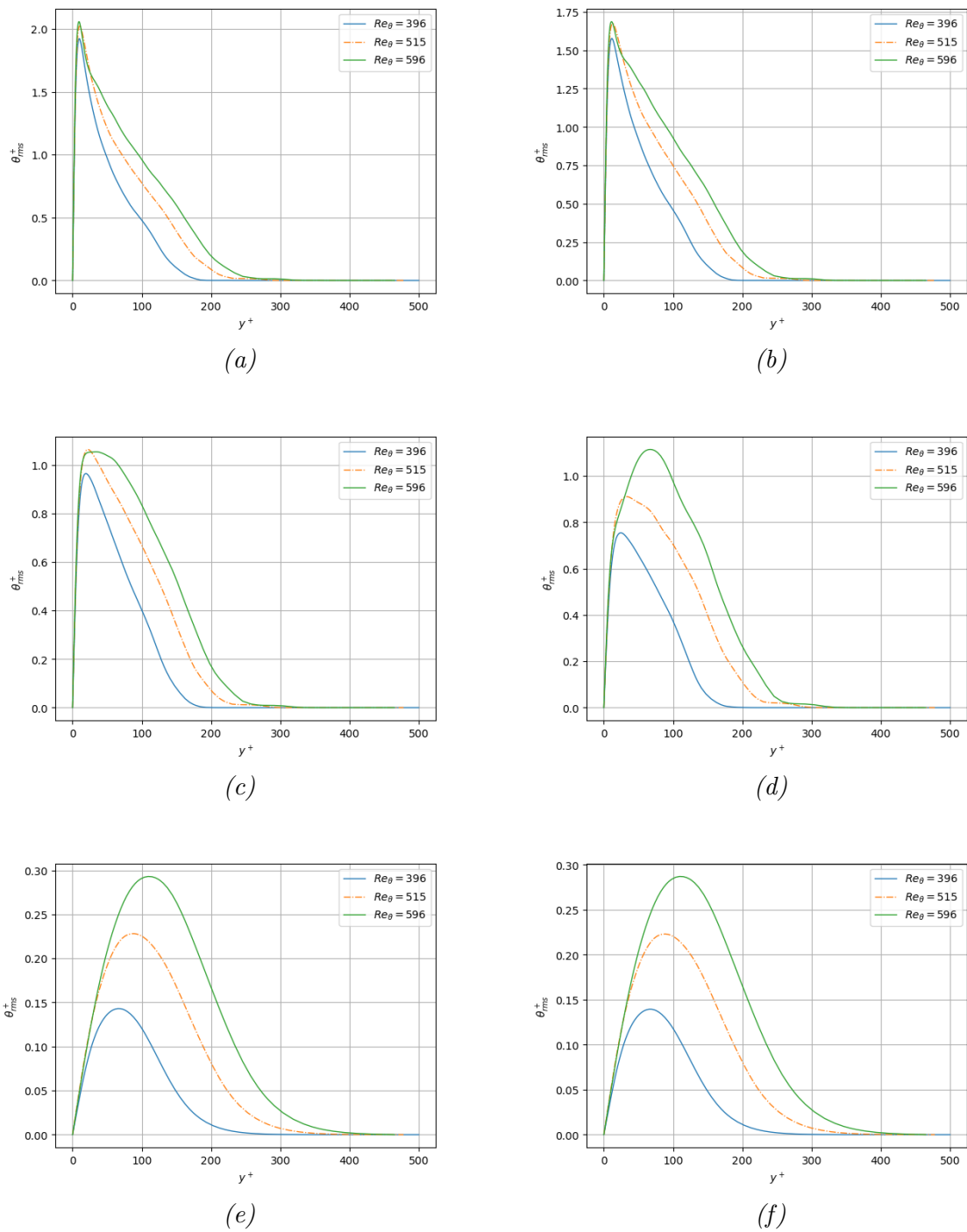


Figure 5.27: RMS values of the scalar fluctuation at different downstream positions for (a) $Pr = 1$, (b) 0.71, (c) $Pr = 0.30$, (d) $Pr = 0.20$, (e) $Pr = 0.0237$, (f) $Pr = 0.0232$ with isothermal wall-boundary conditions.

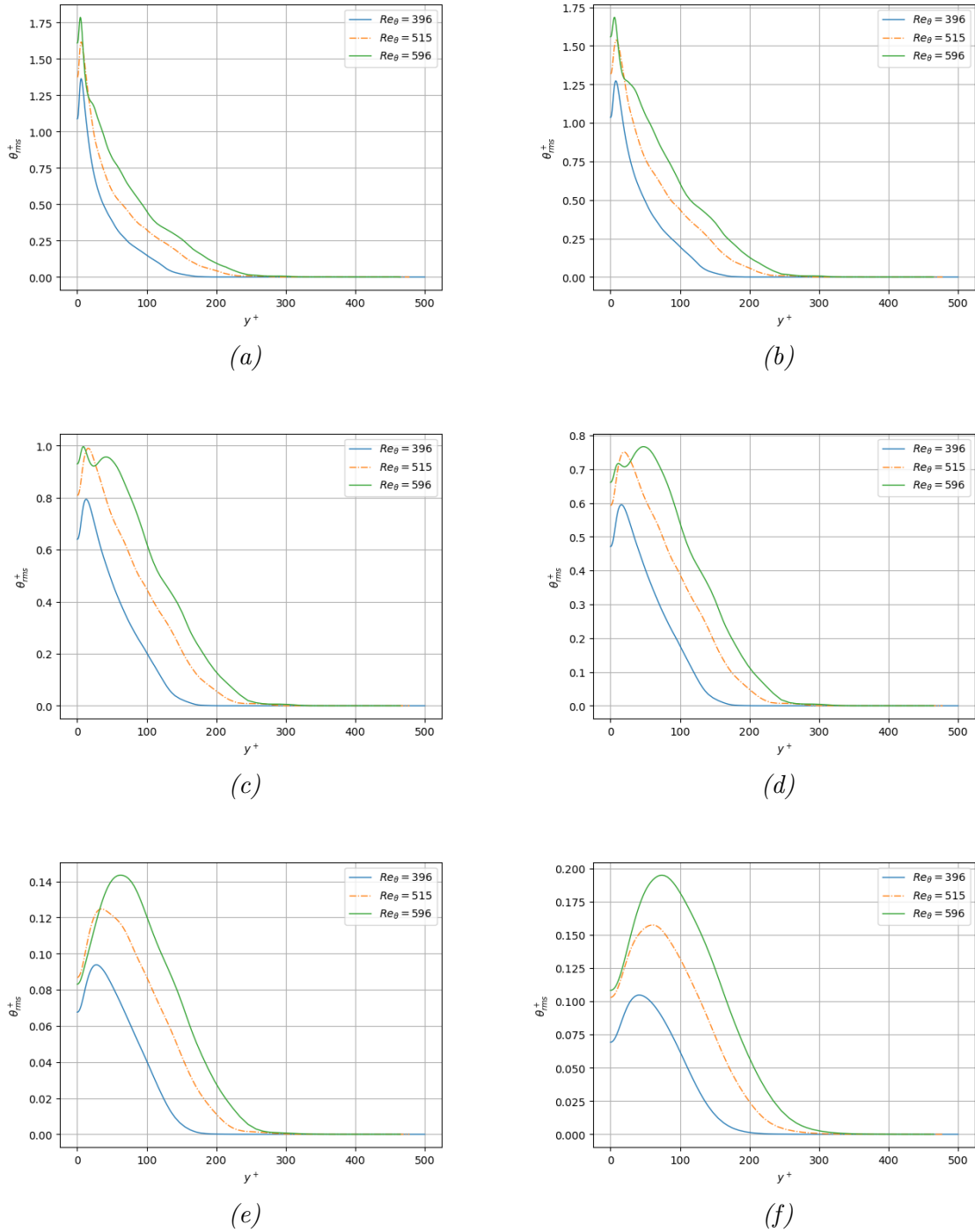


Figure 5.28: RMS values of the scalar fluctuation at different downstream positions for (a) $Pr = 1$, (b) 0.71 , (c) $Pr = 0.30$, (d) $Pr = 0.20$, (e) $Pr = 0.0237$, (f) $Pr = 0.0232$ with isoflux wall-boundary conditions.

The streamwise scalar flux, denoted as $u'\theta'$, represents the transport of heat in the direction of the main flow. As shown in Figures 5.30 and 5.32, the trend indicates that with increasing Reynolds number, the peak value of the streamwise heat flux increases, demonstrating a consistent Reynolds effect. For the highest Prandtl number with isothermal boundary conditions, this trend is evident. However, at $Pr = 0.2$,

the trend changes drastically (see Figure 5.29), with the peak value for the highest Reynolds number being almost twice that of the highest Pr in the range at the same Reynolds. Decreasing the Prandtl number below $Pr = 0.2$ leads to a decrease in the peak value again. This abrupt change in behavior within this range suggests a significant shift in the heat transfer mechanism, warranting further investigation (see Figure 5.36).

For the isoflux boundary condition, the peak values are very high for the highest Reynolds number at $Pr = 1$. In this case, the peak values are within the range, indicating that the Reynolds effect is still present. The behavior of the streamwise scalar flux highlights the importance of considering both Reynolds and Prandtl numbers in heat transfer analysis.

The wall-normal scalar flux, denoted as $v'\theta'$, represents the transport of heat perpendicular to the main flow direction. The trends for the wall-normal heat flux better resemble those of the RMS values, with an increase in the peak value as the Reynolds number increases. As the Prandtl number decreases, the curve shifts the peak towards the right, and the curve becomes thicker. This behavior indicates that at lower Prandtl numbers, the thermal diffusivity is higher, leading to more uniform temperature distributions and less pronounced fluctuations (Figures 5.31 and 5.33).

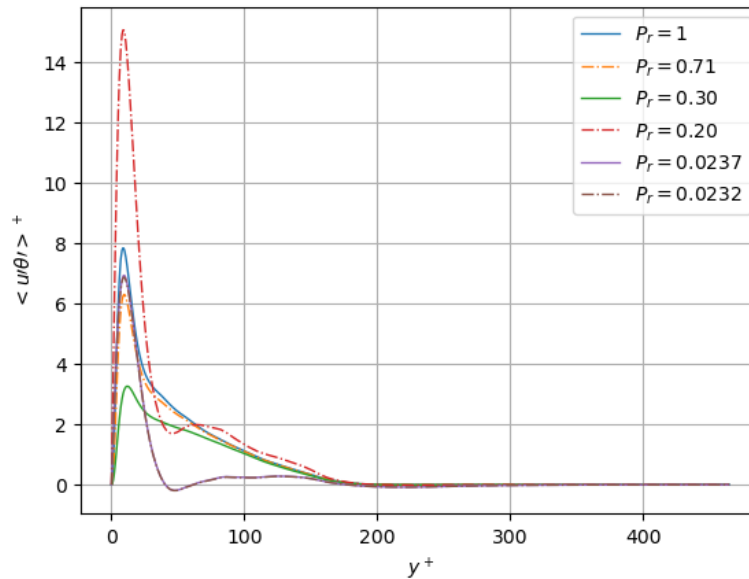


Figure 5.29: Comparison of streamwise scalar flux at $Re_\theta = 596$ for various Prandtl numbers.

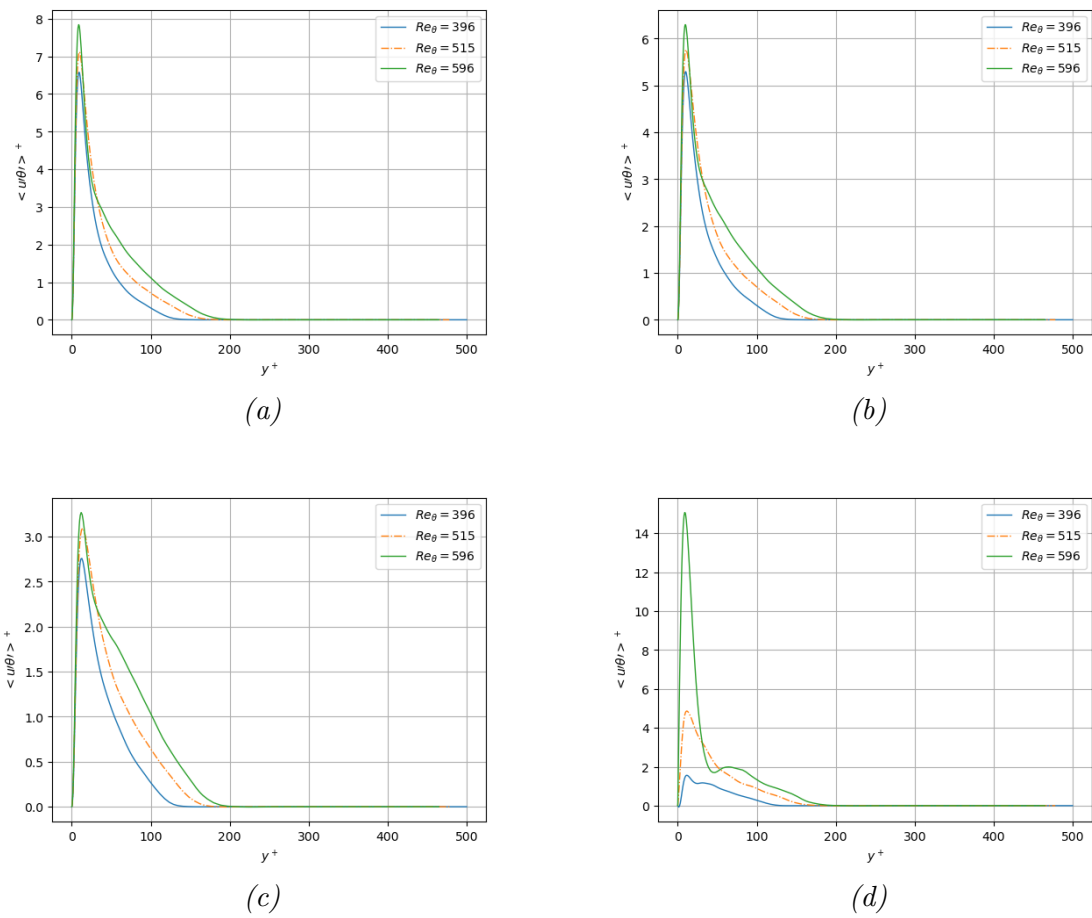


Figure 5.30: Streamwise scalar flux fluctuations at different downstream positions for (a) $Pr = 1$, (b) 0.71 , (c) $Pr = 0.30$, (d) $Pr = 0.20$, with isothermal wall-boundary conditions.

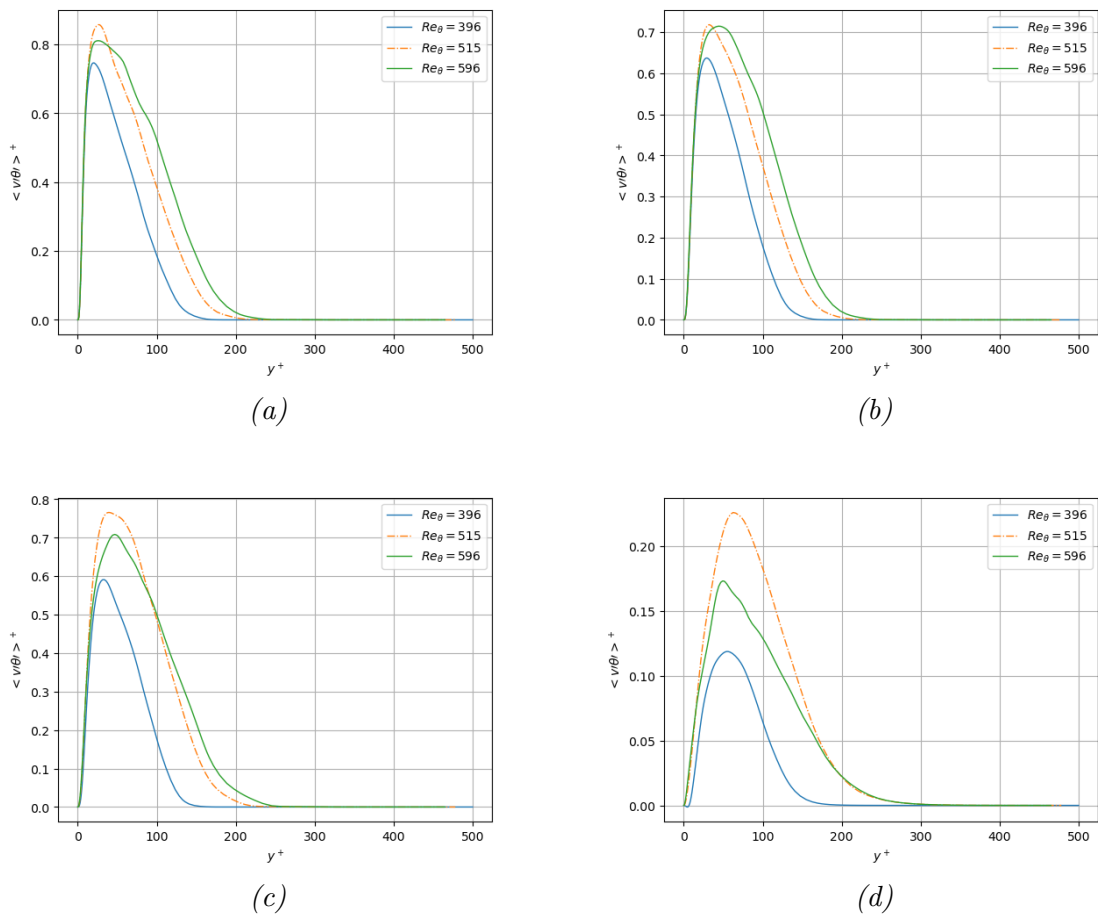


Figure 5.31: Wall-normal scalar flux fluctuations at different downstream positions for (a) $Pr = 1$, (b) 0.30, (c) $Pr = 0.20$, (d) $Pr = 0.0237$, with isothermal wall-boundary conditions.

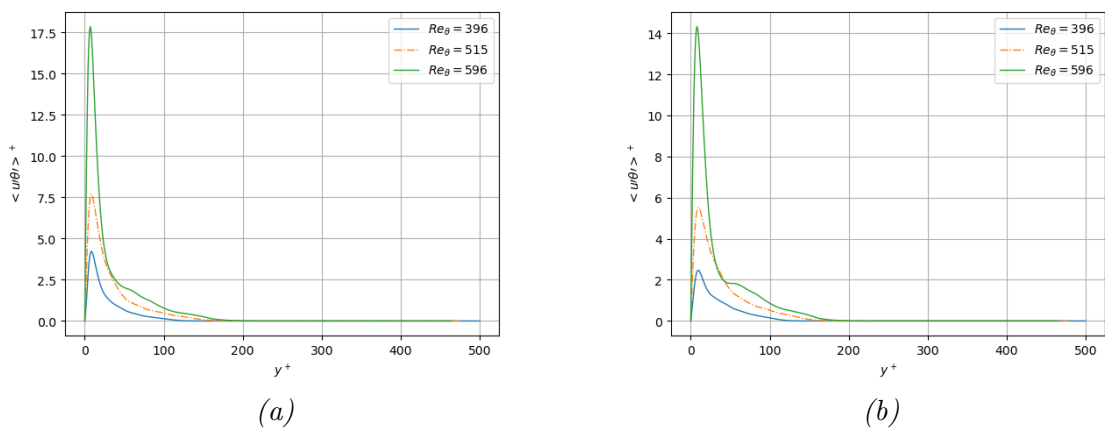


Figure 5.32: Streamwise scalar flux fluctuations at different downstream positions for (a) $Pr = 1$, (b) 0.20 with isoflux wall-boundary conditions.

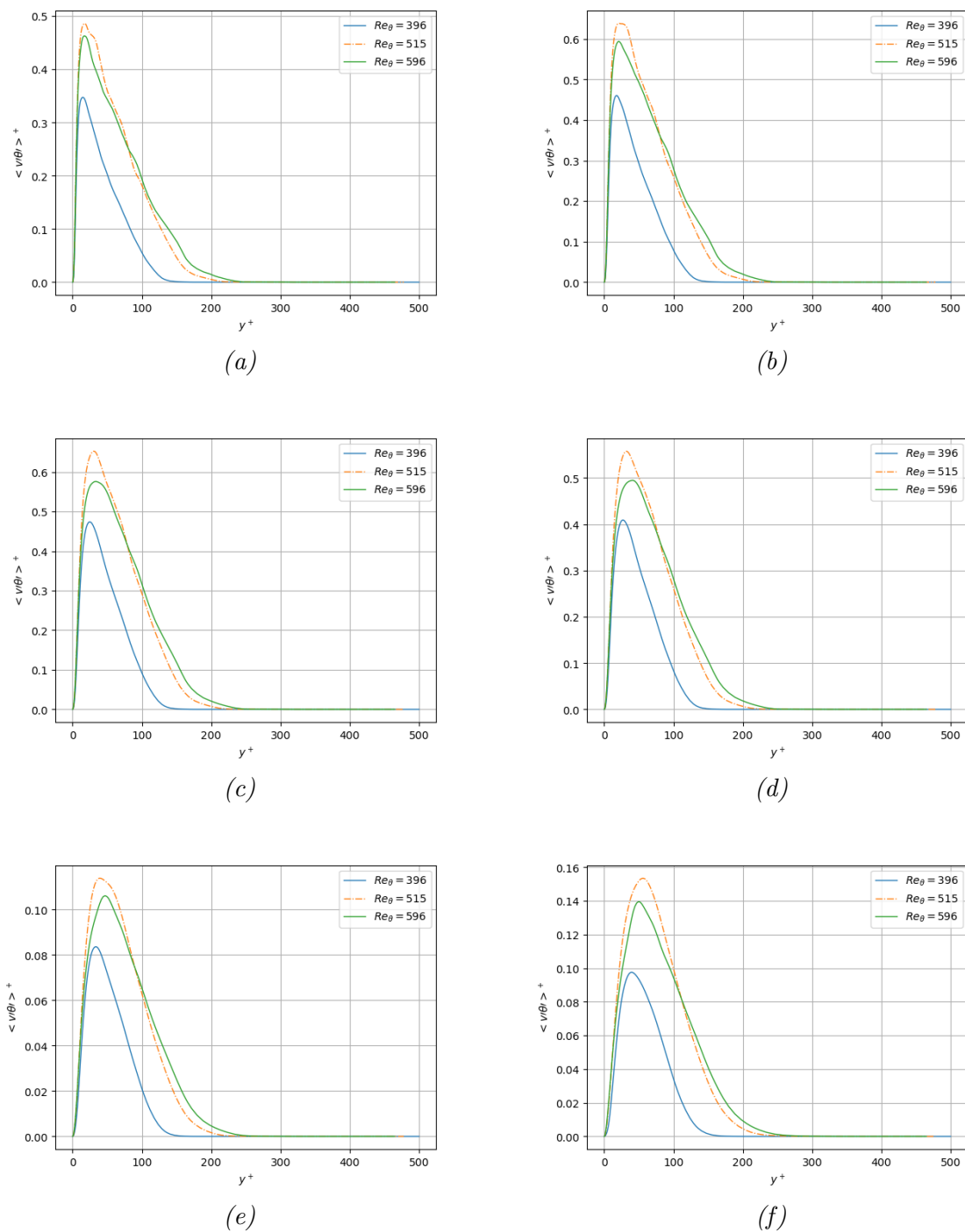


Figure 5.33: Wall-normal scalar flux fluctuations at different downstream positions for (a) $Pr = 1$, (b) 0.71 , (c) $Pr = 0.30$, (d) $Pr = 0.20$, (e) $Pr = 0.0237$, (f) $Pr = 0.0232$ with isoflux wall-boundary conditions.

5.2.3 Turbulent Prandtl Number

Another important parameter in scalar transfer is the turbulent Prandtl number (Pr_t). The turbulent Prandtl number plays a crucial role in predicting near-wall scalar trans-

fer using turbulence models and is defined as the ratio of the turbulent eddy viscosity ν_t to the eddy diffusivity α_t :

$$Pr_t = \frac{\nu_t}{\alpha_t} \quad (5.2)$$

where ν_t and α_t are defined by (strictly only for parallel flows):

$$\nu_t = -\frac{u'v'}{\partial u/\partial y} \quad (5.3)$$

$$\alpha_t = -\frac{v'\theta'}{\partial \theta/\partial y} \quad (5.4)$$

The Reynolds analogy is the simplest model for the turbulent Prandtl number since it leads to the equivalence of the eddy viscosity for momentum transfer and the eddy diffusivity of scalar transfer, such that $Pr_t = 1$. To analyze the near-wall asymptotic behavior of the turbulent scalar statistics, Monin and Yaglom [62] proposed expanding the velocity and scalar distributions in Taylor series. However, in this study, the direct application of the formula valid for flow with one main component was preferred due to its simplicity and accuracy within the boundary layer.

The turbulent Prandtl number was computed up to the thickness of the boundary layer, as outside of it in the free stream a turbulent Prandtl number cannot be defined. This approach was preferable because using a Taylor expansion would lead to an approximate solution even inside the boundary layer.

In Figure 5.34, the trend of the turbulent Prandtl number is shown for $Pr = 1$ and $Pr = 0.71$ to better understand the influence of the wall-boundary condition on it (without the low Pr effect being present). It is clear that for the isothermal boundary condition, the turbulent Prandtl number is almost constant along y^+ , close to one as a value, and does not depend on the Prandtl number (at least in this short range). In contrast, for the isoflux boundary condition, the turbulent Prandtl number approaches zero close to the wall, reaches one at $y^+ \approx 10$, increases, and then decreases. In this case, the curves for the two Prandtl numbers are distinguished, indicating that the turbulent Prandtl number changes with Pr.

In Figure 5.34b, the same comparison is made with $Pr = 1$ and $Pr = 0.0232$ (LBE). For the isoflux boundary condition, the trend is similar even though the Pr range is wider. However, for the isothermal wall-boundary condition, the behavior of the liquid metal Prandtl number departs from the $Pr = 1$ case and resembles more the isoflux case. A third figure shows the comparison within an even smaller range of Pr for two liquid metals, lead and LBE. It can be seen that for the isothermal boundary condition, the curve is not influenced by the Prandtl number, while it is for the isoflux boundary condition. This indicates that the influence of the Prandtl number appears abruptly in the form of the low Pr effect.

To further investigate the behavior between this range from $Pr = 1$ and $Pr = 0.0232$, various Prandtl numbers were considered, as shown in Figure 5.36. It is evident that the abrupt change occurs within $Pr = 0.2 - 0.3$. This change can be attributed to the significant alteration in the interaction between molecular diffusion and turbulent transport mechanisms within this Prandtl number range. As the Prandtl number decreases, the thermal diffusivity increases, leading to more pronounced effects of molecular diffusion close to the wall, which affects the turbulent Prandtl number.

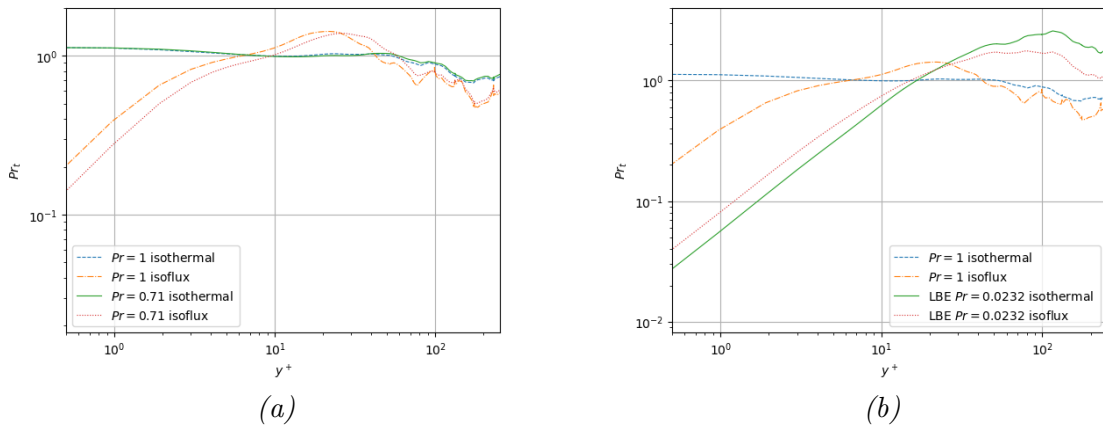


Figure 5.34: Comparison of turbulent Pr with different wall-boundary conditions at $Re_\theta = 596$ for (a) $Pr = 1$ and $Pr = 0.71$, (b) $Pr = 1$ and $Pr = 0.0232$ (LBE).

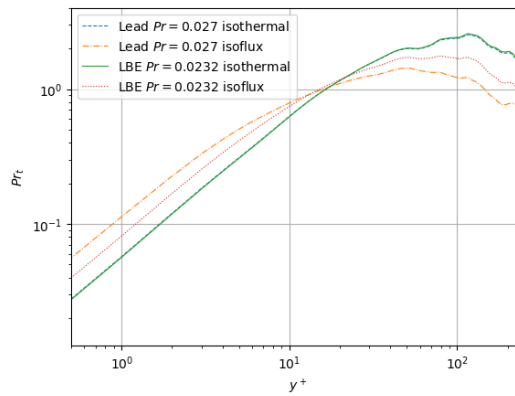


Figure 5.35: Low Pr effect at $Re_\theta = 596$ depending on the wall-boundary conditions.

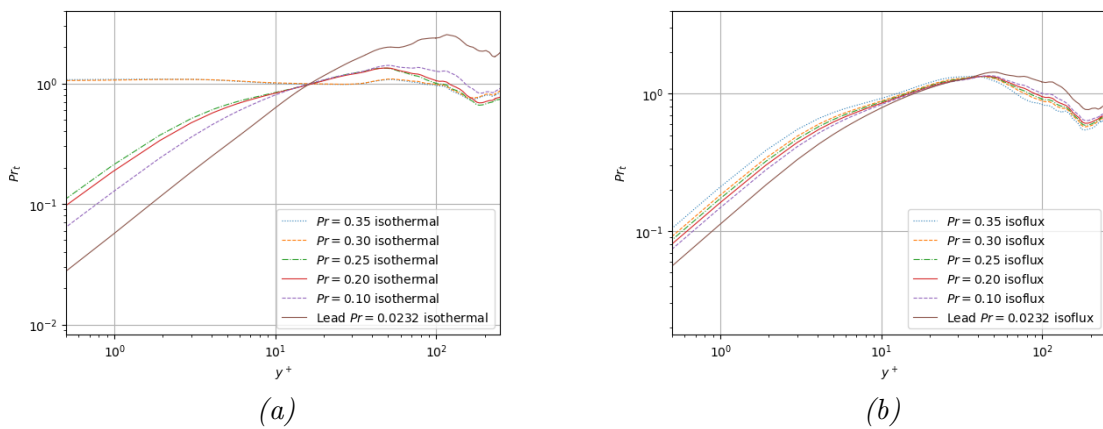


Figure 5.36: Turbulent Pr with different wall-boundary conditions at $Re_\theta = 596$ for a wide range of Prandtl number.

5.2.4 Stanton Number

The **Stanton number (St)** is a dimensionless number that measures the ratio of heat transferred into a fluid to the thermal capacity of the fluid. It is defined as:

$$\text{St} = \frac{h}{\rho U_{\infty} c_p} \quad (5.5)$$

where:

- h is the convection heat transfer coefficient,
- ρ is the density of the fluid,
- U_{∞} is the free stream velocity,
- c_p is the specific heat of the fluid.

It is significant in characterizing heat transfer in forced convection flows, since provides a measure of the efficiency of heat transfer relative to the fluid's capacity to store thermal energy.

For a fluid with a Prandtl number of 1, the momentum diffusivity is equal to the thermal diffusivity. This results in the boundary layer governing equations for mean velocity and mean scalar becoming identical, leading to equivalent solutions for both velocity and scalar fields. This concept, under the name of Reynolds Analogy, relates the turbulent momentum transfer to the heat transfer in a fluid flow and expressed in non-dimensional form, states as:

$$\text{St} = \frac{c_f}{2} \quad (5.6)$$

where c_f is the skin friction coefficient. This relationship shows that the Stanton number is half of the skin friction coefficient for a fluid with $\text{Pr} = 1$.

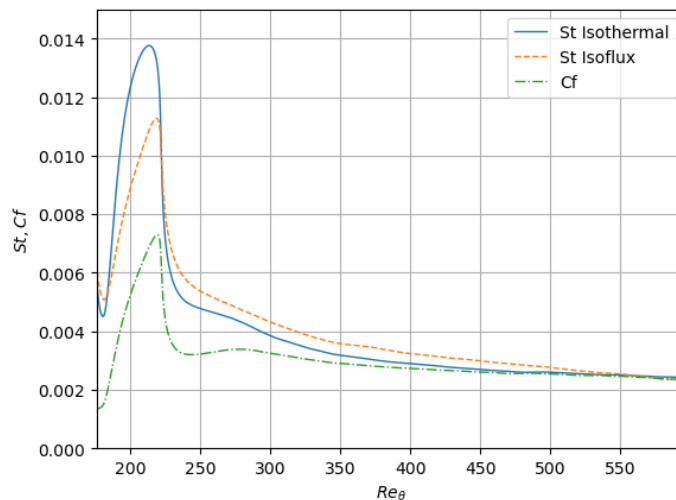


Figure 5.37: Reynolds Analogy: Stanton number for both isothermal and isoflux wall-boundary conditions at $\text{Pr} = 1$ and friction coefficient C_f .

For fluids with Prandtl numbers different from 1, the relationship between the Stanton number and the skin friction coefficient changes. Specifically, for lower Prandtl numbers ($Pr < 1$), the thermal diffusivity is higher relative to the momentum diffusivity. This results in more efficient heat transfer, leading to a higher Stanton number. The Reynolds analogy can be modified to account for different Prandtl numbers.

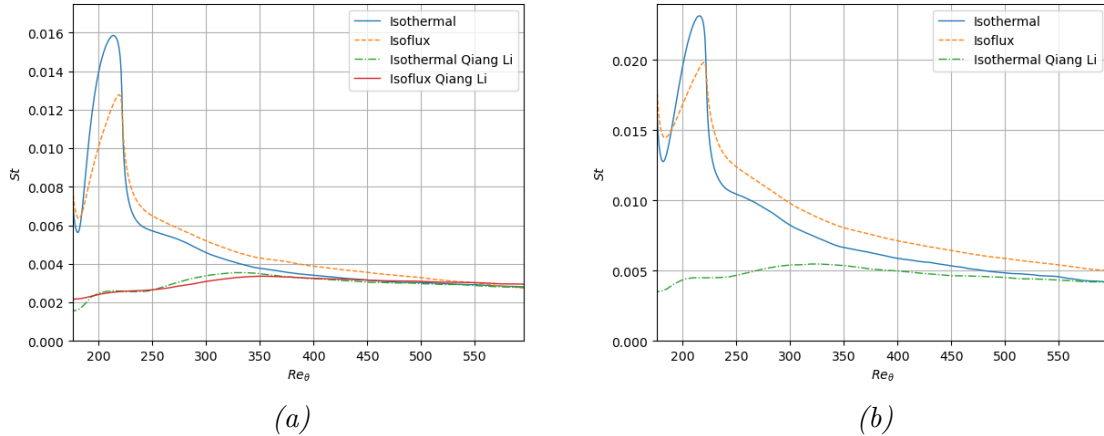


Figure 5.38: Comparison with the data from Li et al. [28] of Stanton number for (a) $Pr = 0.71$ (b) $Pr = 0.2$.

Figure 5.37 shows the comparison of the Stanton number for isothermal and isoflux cases with the skin friction coefficient c_f for a scalar with $Pr = 1$. The similarity in trends is due to the Reynolds analogy, which equates the scalar transfer to the momentum transfer. The overshoot observed in the Stanton number profiles is similar to that of the skin friction coefficient, indicating that the heat transfer behavior closely follows the momentum transfer behavior.

Figure 5.38 compares the data with the results from Li et al. [28] for scalars with $Pr = 0.71$ and $Pr = 0.2$. The trends align with Li's data for $Re_\theta > 400$ because the initial conditions influence the results at lower Reynolds numbers. The Stanton number increases significantly at the beginning due to the inflow condition, where the scalar is set to zero. Also the forcing region increases the Stanton number, leading to a peak around $Re_\theta \approx 200$. This peak is due to strong and random fluctuations in scalar concentration in this region. As verified by Li et al. [28], the isoflux case is smoother than the isothermal one, as evidenced by a smaller peak. This is because an isoflux boundary condition provides a more uniform scalar transfer rate compared to an isothermal boundary condition.

Figure 5.39 shows comparisons within different Prandtl numbers. As Prandtl number decreases, general trends of Stanton number shift to higher values. This occurs because lower Prandtl numbers indicate higher thermal diffusivity relative to momentum diffusivity, resulting in more efficient heat transfer and thus higher Stanton numbers. At $Re_\theta \approx 600$, Stanton number for $Pr = 1$ is one-fifth of value for $Pr = 0.0232$ (LBE). The initial peak is attenuated as the value increases, becoming part of the main trend.

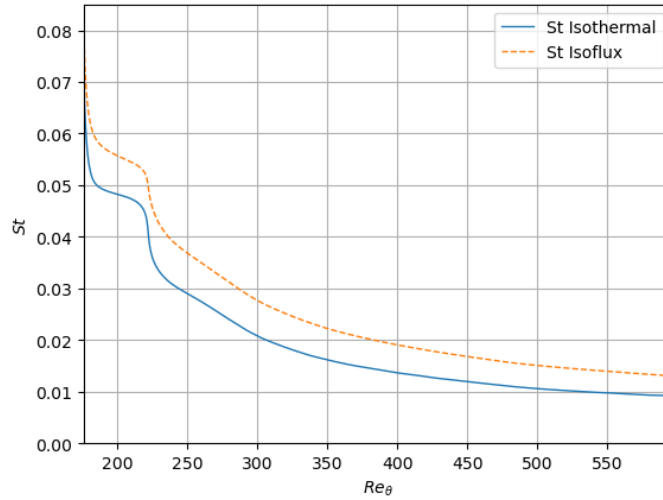


Figure 5.39: Stanton Number at different downstream position for $pr = 0.0232$ (LBE).

5.2.5 Probability Density Function

The probability density function (PDF) distributions of the scalar fluctuations are shown in Figures 5.43, 5.42, 5.40 and 5.41. A Gaussian distribution with zero mean and matching variance is also shown as a reference, denoted by the orange line. Similar to the velocity and pressure fluctuations, the scalar fluctuations are normalized by the corresponding RMS values, and the probability density distributions are normalized such that the area under each curve is unity.

In this study, the PDF was computed for a wide range of Prandtl numbers (Pr) with both isothermal and isoflux wall-boundary conditions at the same y^+ close to the wall. For the isothermal case, it is observed that as the Prandtl number decreases, the PDF becomes less positively skewed, reaching the smallest value for Sodium ($Pr = 0.0058$). This behavior can be explained by the fact that at lower Prandtl numbers, the thermal diffusivity is higher, leading to more uniform temperature distributions and less pronounced positive fluctuations near the wall.

Conversely, for the isoflux case, the behavior is different. As the Prandtl number decreases, the PDF becomes more negatively skewed until it reaches the liquid metal range, where it becomes slightly positively skewed. This can be attributed to the constant heat flux boundary condition, which maintains a nonzero temperature gradient at the wall. At lower Prandtl numbers, the higher thermal diffusivity causes the temperature fluctuations to be more influenced by the imposed heat flux, leading to stronger negative fluctuations. However, in the liquid metal range, the extremely high thermal diffusivity results in a more balanced distribution of temperature fluctuations, causing the skewness to become slightly positive again.

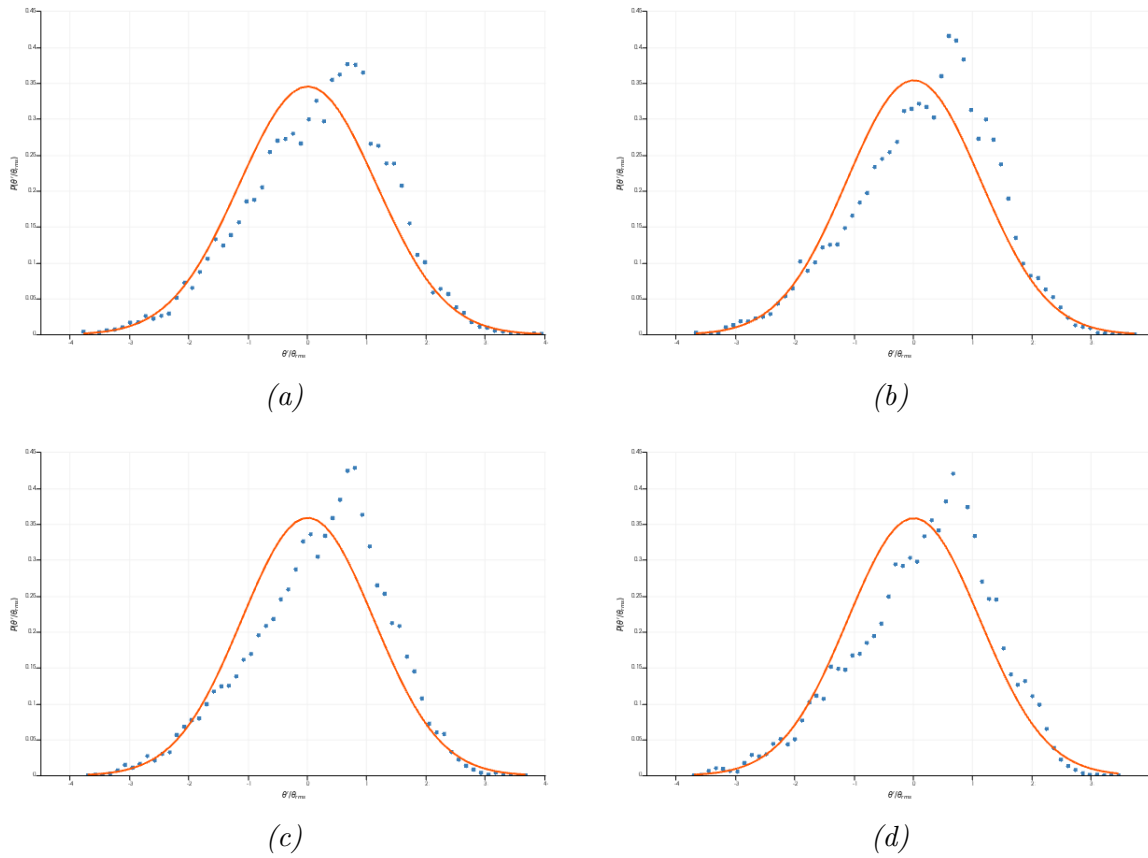


Figure 5.40: PDF of θ' at $y^+ \approx 1.57$ with isoflux wall-boundary condition of the following Prandtl numbers and respective skewness of the distribution: (a) $\text{Pr} = 1$, (b) $\text{Pr} = 0.71$, (c) $\text{Pr} = 0.5$, (d) $\text{Pr} = 0.3$.

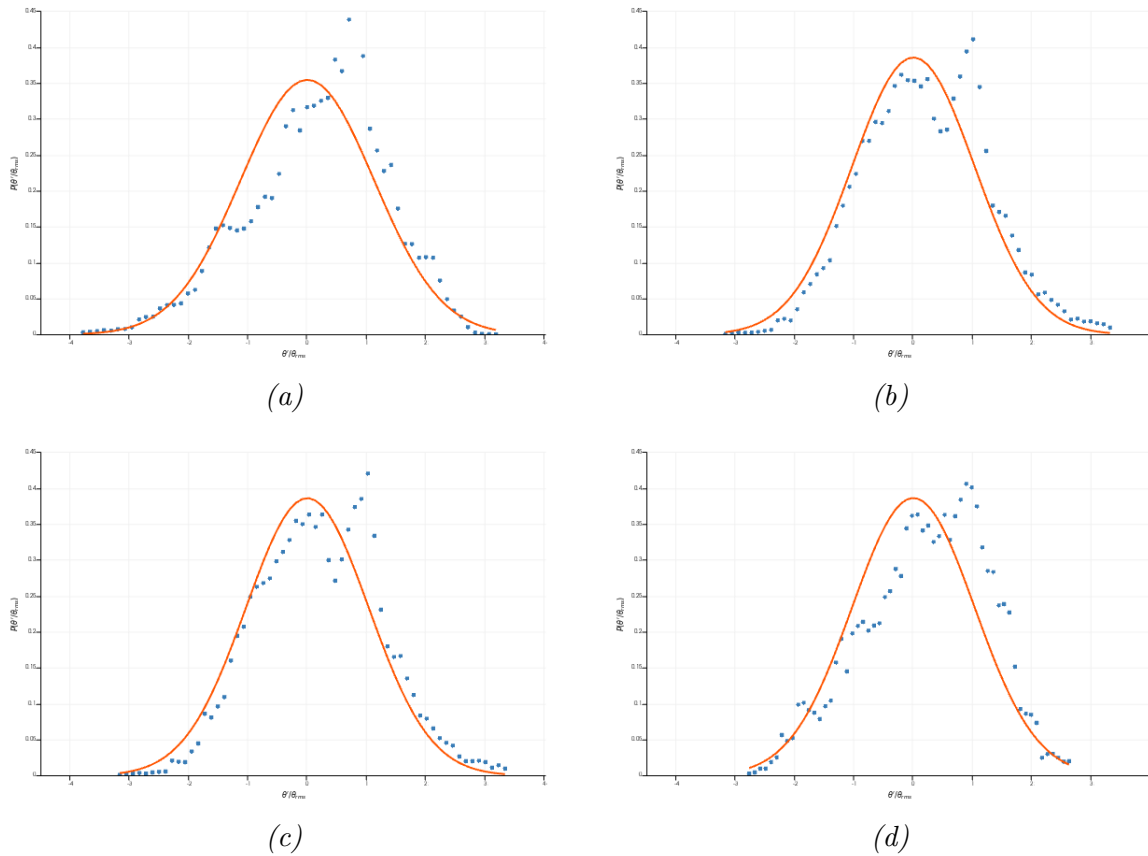


Figure 5.41: PDF of θ' at $y^+ \approx 1.57$ with isoflux wall-boundary condition of the following Prandtl numbers and respective skewness of the distribution: (a) $Pr = 0.2$, (b) $Pr = 0.0237$, (c) $Pr = 0.0232$, (d) $Pr = 0.0058$.

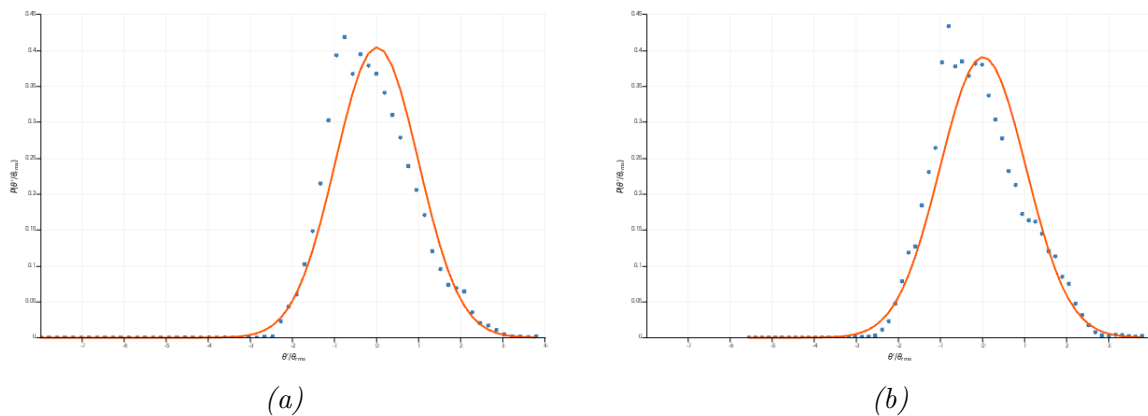


Figure 5.42: PDF of θ' at $y^+ \approx 1.57$ with isoscalar wall-boundary condition of the following Prandtl numbers and respective skewness of the distribution: (a) $Pr = 0.0232$, (b) $Pr = 0.0058$.

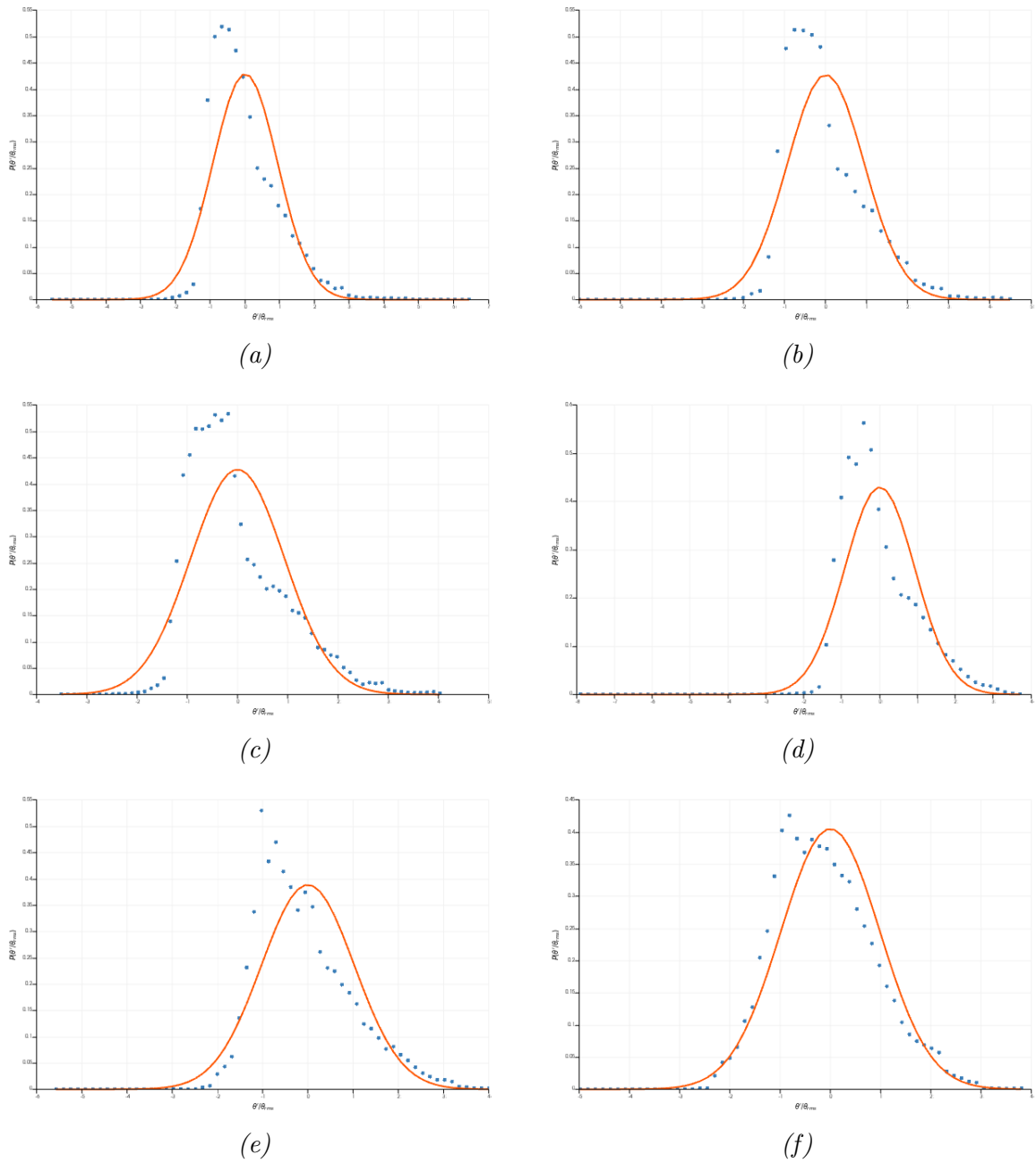


Figure 5.43: PDF of θ' at $y^+ \approx 1.57$ with isoscalar wall-boundary condition of the following Prandtl numbers and respective skewness of the distribution: (a) $Pr = 1$, (b) $Pr = 0.71$, (c) $Pr = 0.5$, (d) $Pr = 0.3$, (e) $Pr = 0.2$, (f) $Pr = 0.0237$.

5.3 Comparative Analysis of Velocity and Scalar Fields

The comparative analysis of the velocity field and scalar field aims to understand the intricate interactions between these fields in a turbulent boundary layer, considering different wall-boundary conditions and various Prandtl numbers. This comparison is conducted using various methods, including energy spectra, joint probability density functions (JPDF) and visualization of contour plots, to provide a comprehensive view of the flow dynamics and scalar transport mechanisms.

5.3.1 Energy Spectrum

In the present analysis, the energy spectra within velocity and scalar fields are compared at different Prandtl numbers ($Pr = 1$, $Pr = 0.2$, and $Pr = 0.0232$) across three y^+ positions corresponding to the viscous sublayer, buffer layer, and log layer for the velocity field, as shown in Figures 5.44 and 5.45. For $Pr = 1$, the similarity between thermal diffusivity and momentum diffusivity results in boundary layers of nearly identical thickness, demonstrating the Reynolds analogy. In the case of $Pr = 0.0232$, at $y^+ = 22.8$, the velocity field is in the buffer layer, but the scalar field remains laminar due to the significantly higher thermal diffusivity compared to momentum diffusivity.

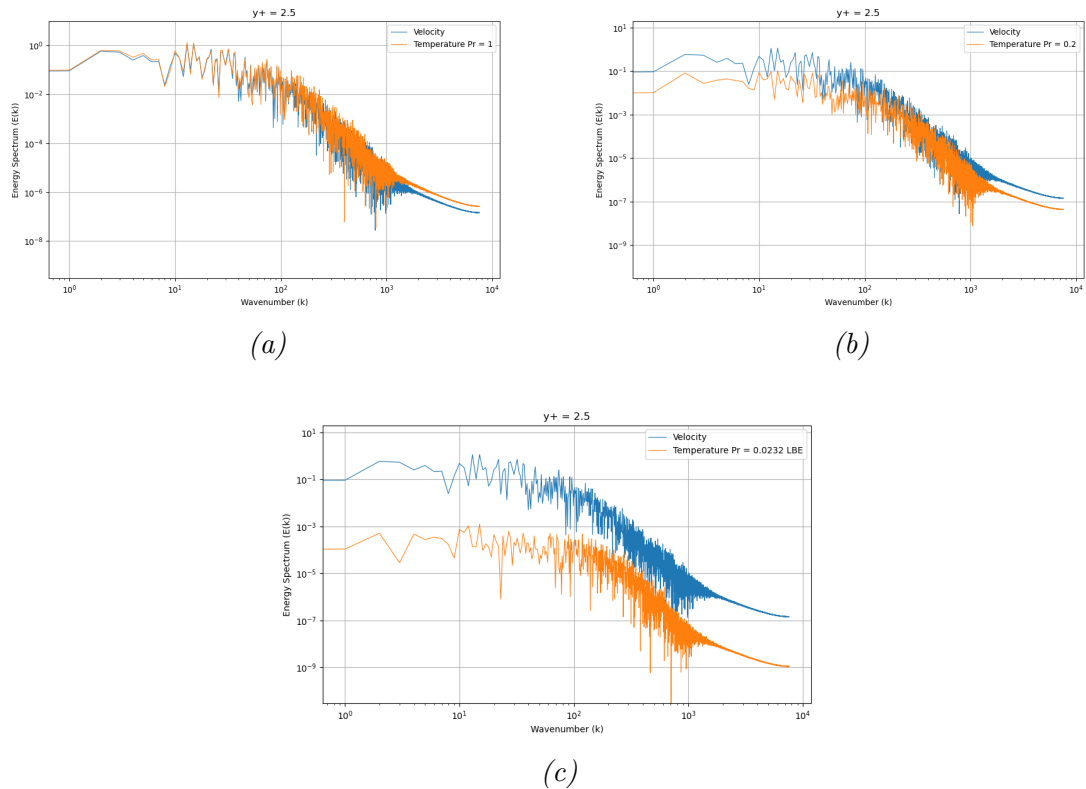


Figure 5.44: Comparison of energy spectra of flow and scalar fields at $y^+ \approx 2.5$ with isothermal wall-boundary condition of the following Prandtl numbers: (a) $Pr = 1$, (b) $Pr = 0.2$, (c) $Pr = 0.0232$.

This difference in diffusivity levels causes the scalar field to lag behind in its transition to turbulence. Additionally, at $y^+ = 154.5$, the velocity field is already in the log-region, while the scalar field has not yet reached the buffer layer, highlighting the disparity in their respective diffusivities. For the intermediate case of $Pr = 0.2$, the behavior of the scalar field is quite similar to the velocity field, but with slightly lower energy levels due to the moderate thermal diffusivity.

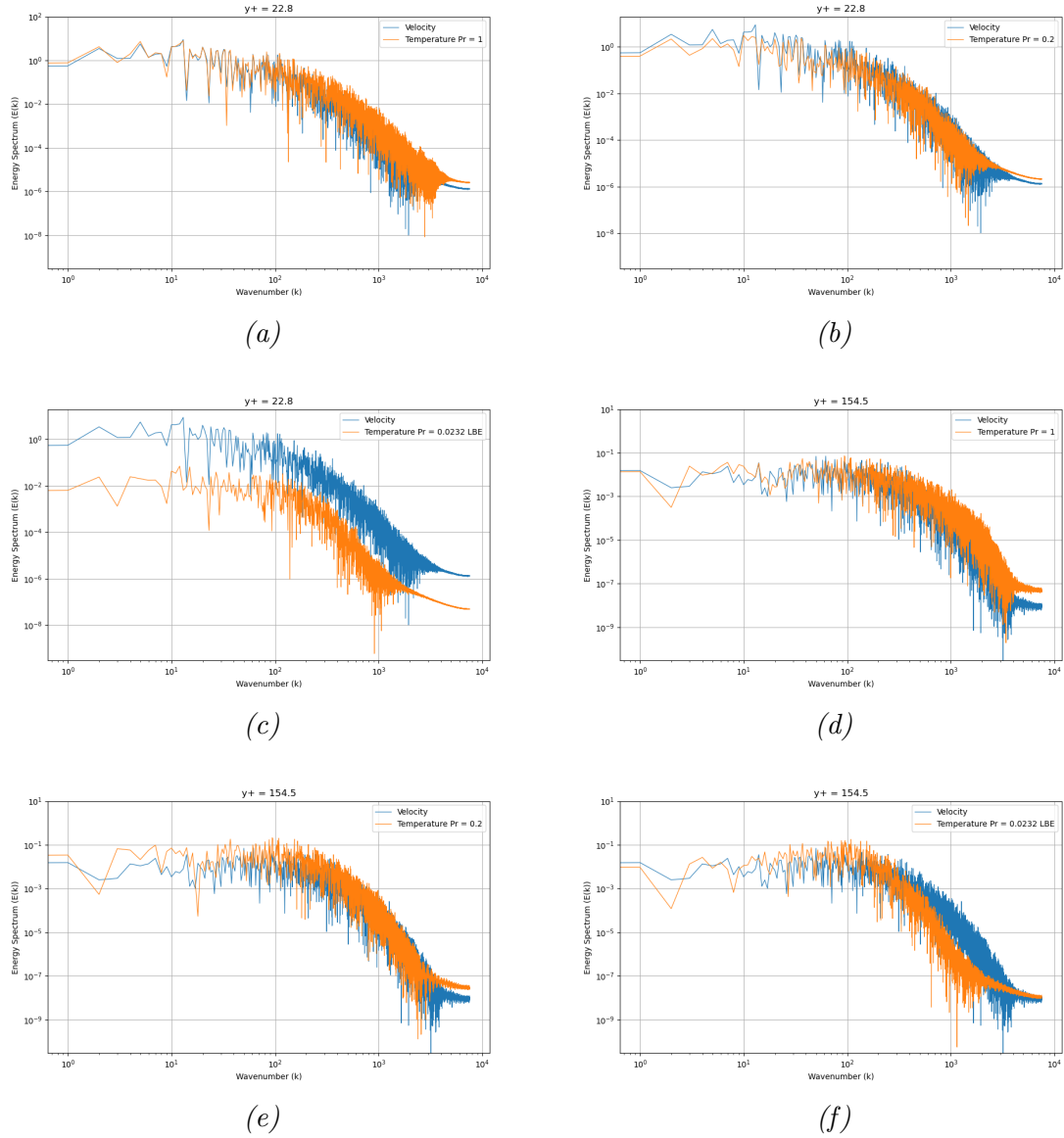


Figure 5.45: Comparison of energy spectra of flow and scalar fields with isothermal wall-boundary condition of the following Prandtl numbers and wall normal position: (a) $Pr = 1$ $y^+ = 22.8$, (b) $Pr = 0.2$ $y^+ = 22.8$, (c) $Pr = 0.0232$ $y^+ = 22.8$ (d) $Pr = 1$ $y^+ = 154.5$, (e) $Pr = 0.2$ $y^+ = 154.5$, (f) $Pr = 0.0232$ $y^+ = 154.5$.

5.3.2 Joint Probability Density Function

Stochastic methods use distribution functions to describe fluctuating scalars in a turbulent field. For two variables ϕ and ψ , the joint-PDF (JPDF) is defined as:

$$P(\Phi, \Psi) \quad (5.7)$$

The correlation between the two variables is given by:

$$\overline{\phi'\psi'} = \int (\phi - \bar{\phi})(\psi - \bar{\psi})P(\Phi, \Psi) d\Phi d\Psi \quad (5.8)$$

In this study, the JPDF of $P(u', \theta')$ for different scalars at $y^+ \approx 1.57$ is analyzed. For $Pr = 1$, the correlation between the velocity and scalar fields is very strong, as perfect correlation is represented by a straight line. For $Pr = 0.71$, the line becomes thicker, and for both $Pr = 2$ and $Pr = 0.5$, the thickness is similar, indicating a departure from the Reynolds analogy and a weakening of the correlation between u' and θ' . As the Prandtl number decreases further, the shape becomes rounded and no longer resembles a line, indicating no correlation between the fields.

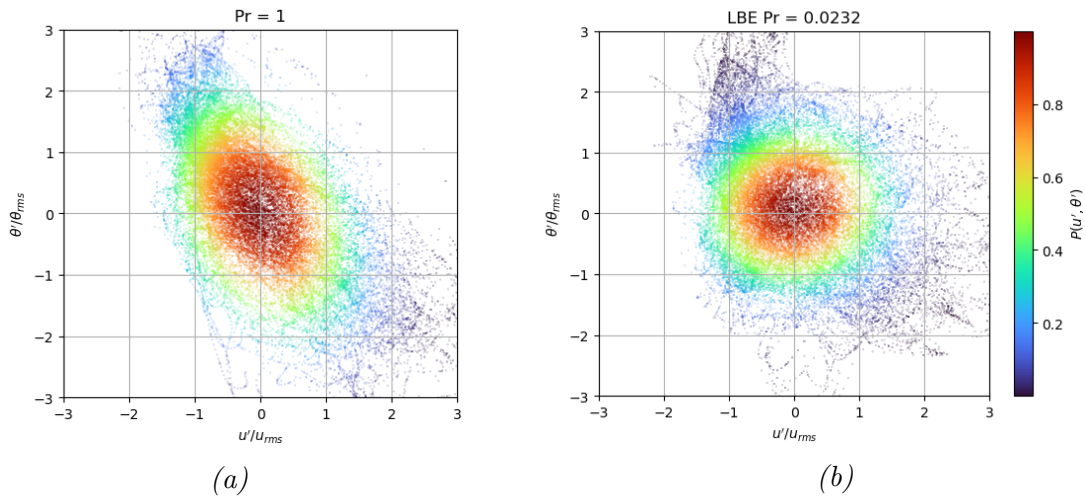


Figure 5.46: JPDF of (u', θ') with isoflux wall-boundary conditions of the following Prandtl numbers: (a) $Pr = 1$, (b) $Pr = 0.0232$.

A comparison between isoscalar (Figure 5.47) and isoflux wall-boundary conditions (Figure 5.46) shows that for the isoflux condition, the flow and scalar fields are less correlated, even for $Pr = 1$, which is highly correlated in the isothermal case.

In summary, the JPDF analysis demonstrates that the correlation between velocity and scalar fields is highly dependent on the Prandtl number and boundary conditions. At Prandtl numbers close to unity, the correlation is strong, whereas it diminishes at lower Prandtl numbers. Additionally, the isoflux boundary condition tends to weaken the correlation further compared to the isoscalar condition, showing clearly the significant influence of thermal boundary conditions on scalar transport mechanisms.

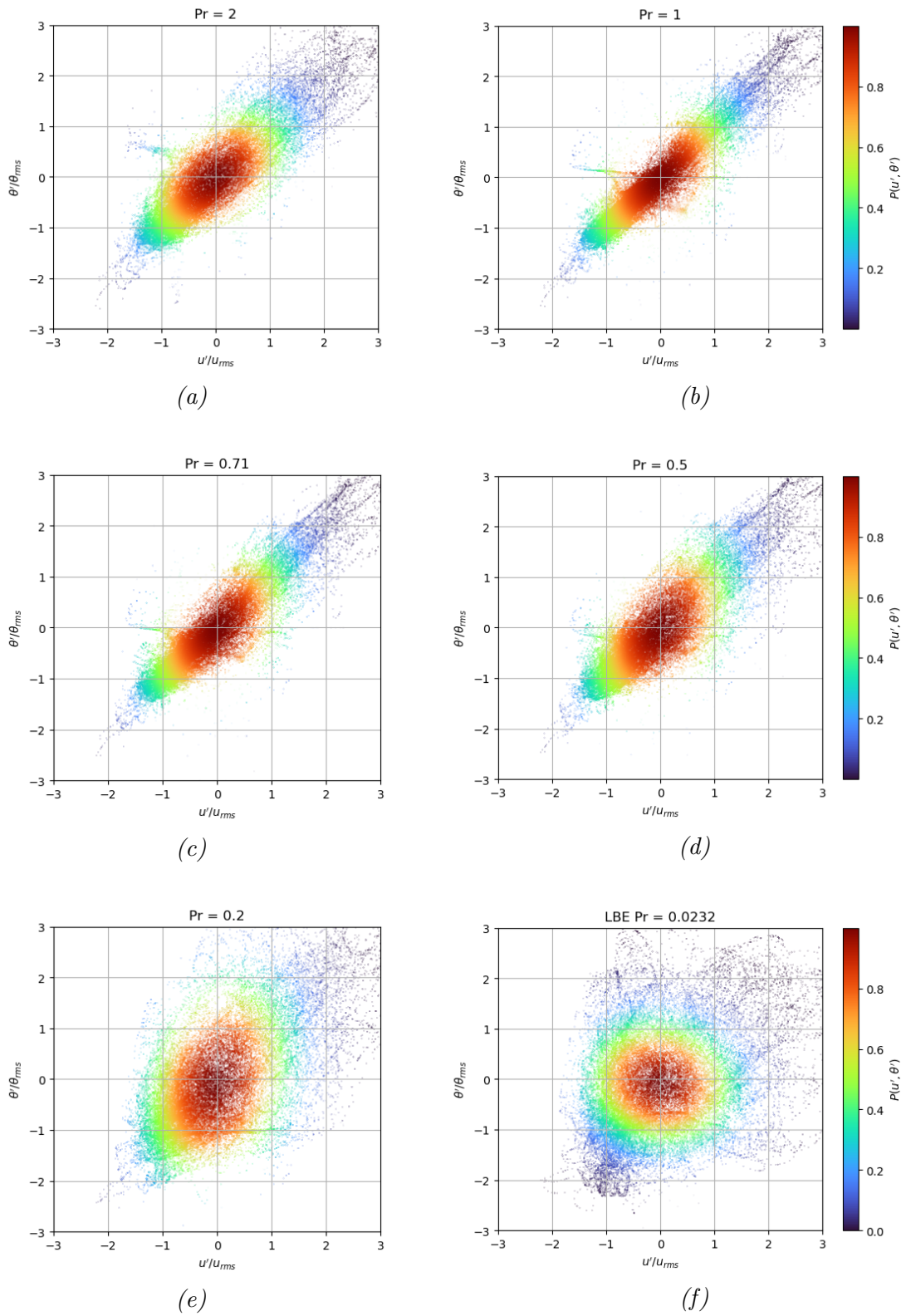


Figure 5.47: JPDF of (u', θ') with isoscalar wall/boundary condition of the following Prandtl numbers: (a) $Pr = 2$, (b) $Pr = 1$, (c) $Pr = 0.71$, (d) $Pr = 0.5$, (e) $Pr = 0.2$, (f) $Pr = 0.0232$.

5.4 Visualization of Instantaneous Fields

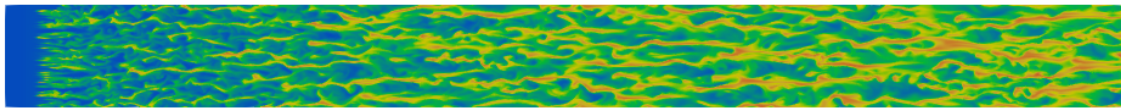
The instantaneous fields of both velocity and thermal scalars in a turbulent boundary layer are presented. The analysis focuses on the development of passive scalars starting from Prandtl unity to the range of very small Prandtl numbers, to confirm the previous results and trends. Visualizations are shown in both the x-z and x-y planes to provide a comprehensive view of the flow and scalar fields. All the contour plots are obtained at the same time instant and the visualized box is the entire computational domain.

5.4.1 Plane x-z

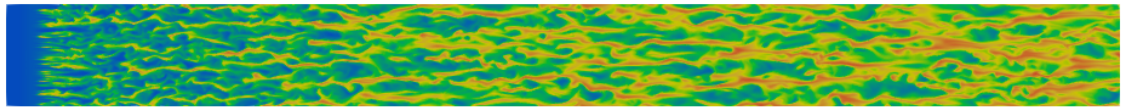
Figures 5.49, 5.48 and 5.50 show the instantaneous streamwise velocity and scalar fluctuations in the x-y plane, at $y^+ \approx 1.57$, for both isoscalar and isoflux wall-boundary condition. For all the contour plots at $Re_\theta = 175$, a laminar region can be observed without streaks because the Blasius laminar profile is imposed at the inlet 4.2.1. At $Re_\theta = 203$, a high alternate region of low and high gradients can be observed, corresponding to the forcing region where the flow is tripped to turbulence 4.4.2. The velocity field reveals streaky structures, with regions of high and low-speed fluid aligned in the streamwise direction. These streaks are a common feature of turbulent boundary layers and are associated with the near-wall cycle of turbulence production. The scalar field also exhibits streaky structures, with regions of high and low scalar concentrations elongated in the streamwise direction, especially the contour plots for $Pr = 1$ 5.48a and $Pr = 0.71$ 5.48b exhibit this structures quite well, indicating a strong coupling between the velocity and scalar fields. The streaks are elongated in the streamwise direction, reflecting the dominant direction of turbulent transport.

In the range of $Pr = 0.3$ to $Pr = 0.2$ (5.48c, 5.48d), the structures are less elongated due to the increased dominance of thermal diffusion over momentum diffusion, showing a lower coupling between flow and scalar fields, similar to what was observed in 5.47. For $Pr = 0.0232$ 5.48e, corresponding to the liquid metal LBE, almost no structures can be seen, and for Sodium ($Pr = 0.0058$) 5.48f, the structures are not present anymore. This is because at very low Prandtl numbers, thermal diffusivity is much higher, leading to a more uniform temperature distribution and the disappearance of streaky structures.

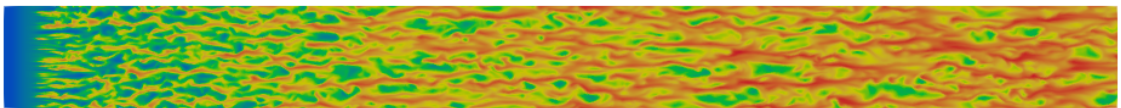
In Figures 5.48 and 5.50 the comparison between isothermal and isoflux boundary conditions shows that for the isoflux condition, the structures are less elongated. The spanwise spacing of the scalar streaks is similar to that of the velocity streaks for the isothermal boundary condition but becomes larger for the isoflux boundary condition.



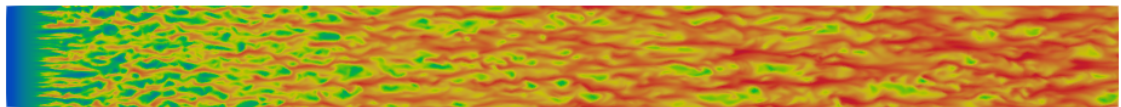
(a)



(b)



(c)



(d)



(e)



(f)

Figure 5.48: Instantaneous contour plot of the fluctuating scalar fields, with isothermal boundary condition at the wall, in the x — z plane at $y^+ = 1.57$, starting from $Re_\theta = 175$ to $Re_\theta = 596$. The plots are in order of the following Prandtl numbers: (a) $Pr = 1$, (b) $Pr = 0.71$, (c) $Pr = 0.3$, (d) $Pr = 0.2$, (e) $Pr = 0.0232$, (f) $Pr = 0.0058$.

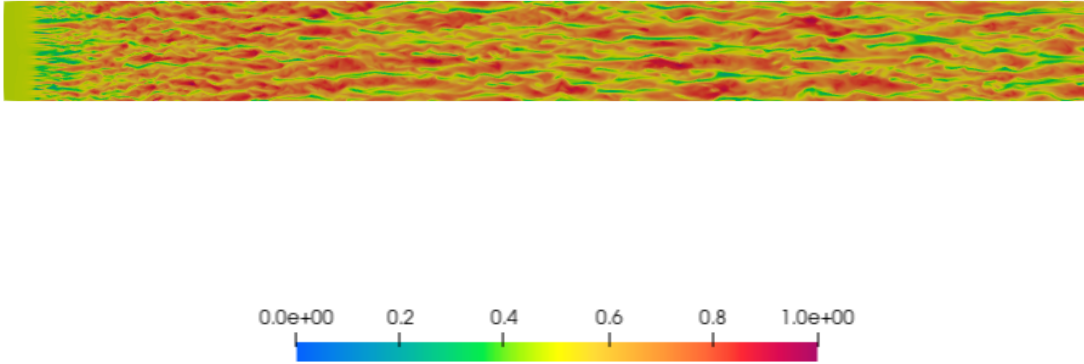
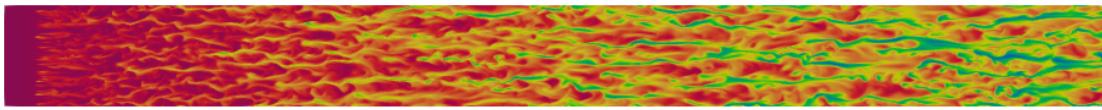


Figure 5.49: Instantaneous contour plot of the flow fields in the x — z plane for $y^+ = 1.57$, starting from $Re_\theta = 175$ to $Re_\theta = 596$.

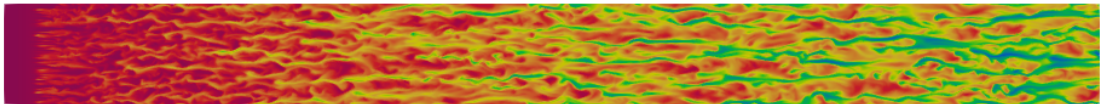
This difference is attributed to the constant heat flux in the isoflux condition, which affects the scalar transport mechanisms as discussed in the previous section and shown in Figure 5.46

5.4.2 Plane x - y

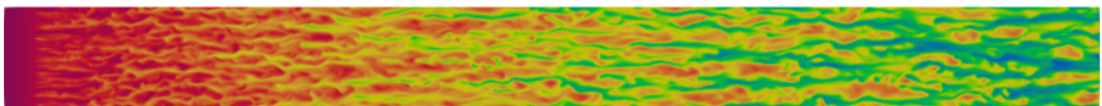
Figures 5.52, 5.51 and 5.53 show the instantaneous streamwise velocity and scalar fluctuations in the x - y plane, in the middle of the computational domain, for both isoscalar and isoflux wall-boundary condition. In this plane, the boundary layer thickness is clearly visible, increasing as the Prandtl number decreases and reaching a maximum for Sodium ($Pr = 0.0058$ 5.51f). The boundary layer itself smoothens out while its thickness increases. This happens because at very low Prandtl numbers, thermal diffusivity dominates over momentum diffusivity, causing heat to spread more quickly through the fluid than momentum, resulting in a thicker and smoother thermal boundary layer because the temperature gradients are less steep. In particular is the reduced influence of viscous forces that leads to a smoother boundary layer profile, as the irregularities caused by viscous effects are less pronounced. A more uniform temperature distribution across the boundary layer can be seen in 5.51f, contributing to a linear-like profile rather than the irregular structures observed at higher Prandtl numbers. The Reynolds analogy is evident when comparing the contour plot of the flow field with that of the scalar field at $Pr = 1$ 5.51a, highlighting the similarity in the transport mechanisms of momentum and heat. Also a comparison within isothermal wall-boundary condition 5.51 and isoflux one 5.53 can be done, since for isothermal boundary conditions, the wall temperature remains constant, leading to zero temperature fluctuations at the wall, instead isoflux boundary conditions maintain a constant heat flux, resulting in nonzero temperature fluctuations at the wall.



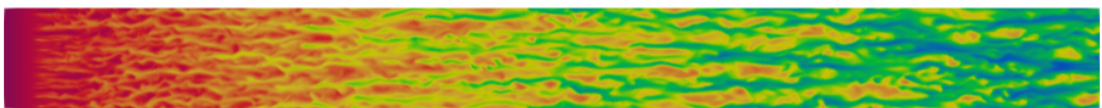
(a)



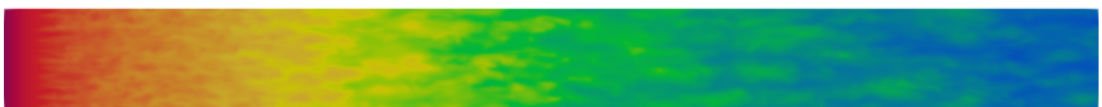
(b)



(c)



(d)



(e)

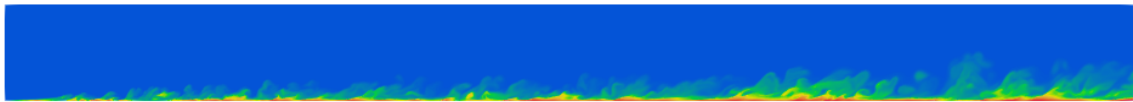


(f)

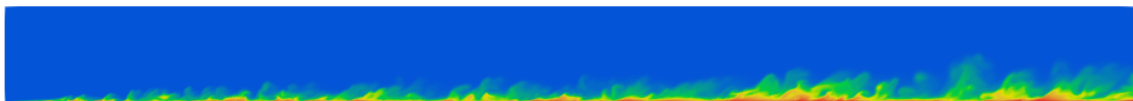
Figure 5.50: Instantaneous contour plot of the fluctuating scalar fields, with isoflux boundary condition at the wall, in the x – z plane at $y^+ = 1.57$, starting from $Re_\theta = 175$ to $Re_\theta = 596$. The plots are in order of the following Prandtl numbers: (a) $Pr = 1$, (b) $Pr = 0.71$, (c) $Pr = 0.3$, (d) $Pr = 0.2$, (e) $Pr = 0.0232$, (f) $Pr = 0.0058$.



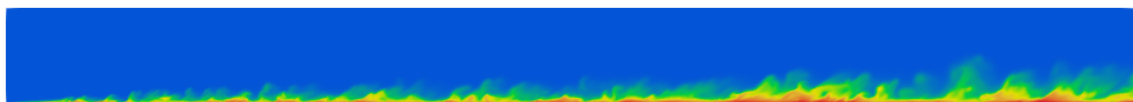
(a)



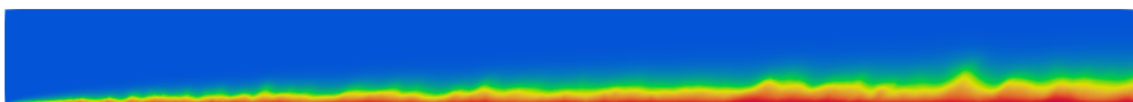
(b)



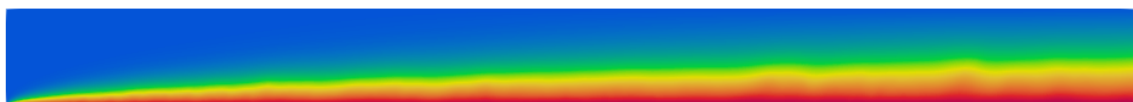
(c)



(d)



(e)



(f)

Figure 5.51: Instantaneous contour plot of the fluctuating scalar fields, with isothermal boundary condition at the wall, in a x – y plane, starting from $Re_\theta = 175$ to $Re_\theta = 596$. The plots are in order of the following Prandtl numbers: (a) $Pr = 1$, (b) $Pr = 0.71$, (c) $Pr = 0.3$, (d) $Pr = 0.2$, (e) $Pr = 0.0232$, (f) $Pr = 0.0058$.

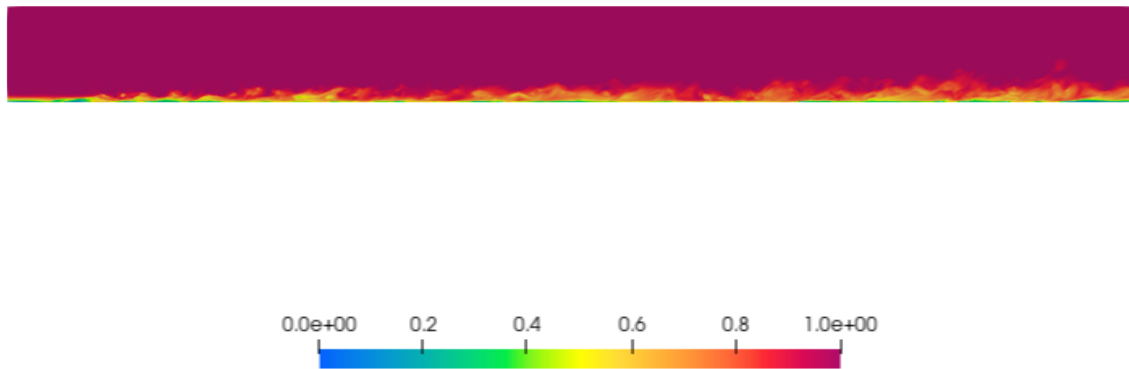


Figure 5.52: Instantaneous contour plot of the flow field in a x — y plane, starting from $Re_\theta = 175$ to $Re_\theta = 596$



(a)



(b)



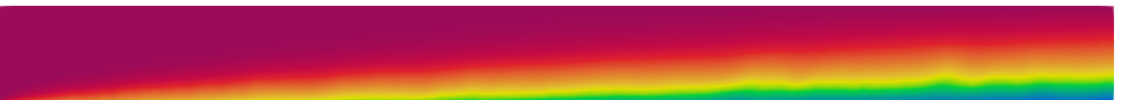
(c)



(d)



(e)



(f)

Figure 5.53: Instantaneous contour plot of the fluctuating scalar fields, with isoflux boundary condition at the wall, in a x – y plane, starting from $Re_\theta = 175$ to $Re_\theta = 596$. The plots are in order of the following Prandtl numbers: (a) $Pr = 1$, (b) $Pr = 0.71$, (c) $Pr = 0.3$, (d) $Pr = 0.2$, (e) $Pr = 0.0232$, (f) $Pr = 0.0058$.

Chapter 6

Conclusion

This thesis presents results of a Direct Numerical Simulation of a heated turbulent boundary layer under forced convection, carried out for 30 scalar fields with varying Prandtl numbers and wall-boundary conditions to better investigate the heat transfer mechanisms, especially as the Prandtl number decreases. As explained in 3.3, the dominance of $\alpha \frac{\partial \langle \theta \rangle}{\partial y}$ in the inner region and $\langle v' \theta' \rangle$ in the outer region can vary significantly with the molecular Prandtl number, which depends on the particular fluid. This variation is crucial for understanding the behavior of scalar transport in turbulent flows.

The statistics and averaged results obtained from the simulation provide valuable insights into the behavior of scalars. Notably, there is a clear change in behavior within the range of $Pr = 0.2-0.3$. This significant change can be observed through the turbulent Prandtl number, which, as shown in Figures 6.1, is often chosen to be close to unity. However, the figure indicates that as the Prandtl number decreases, the turbulent Prandtl number has a drastically lower value near the wall, and the trend towards this change is not continuous but rather abrupt after $Pr = 0.25$. Specifically, for $Pr < 0.25$, the turbulent Prandtl number close to the wall approaches zero and then increases above unity. This behavior is observed only for the isothermal wall-boundary case, as discussed in Chapter 5. Throughout the discussion, particular attention was paid to the range of $Pr = 0.2-0.3$ also in the turbulent statistics, as the mean scalar profiles within this range exhibit a transition where the logarithmic region diminishes.

This abrupt change in behavior suggests that the interaction between molecular diffusion and turbulent transport is significantly altered within this Prandtl number range, affecting the scalar distribution earlier in the boundary layer. The decrease in the turbulent Prandtl number near the wall indicates a shift in the dominant transport mechanism from turbulent to molecular diffusion, which is more pronounced at lower Prandtl numbers.

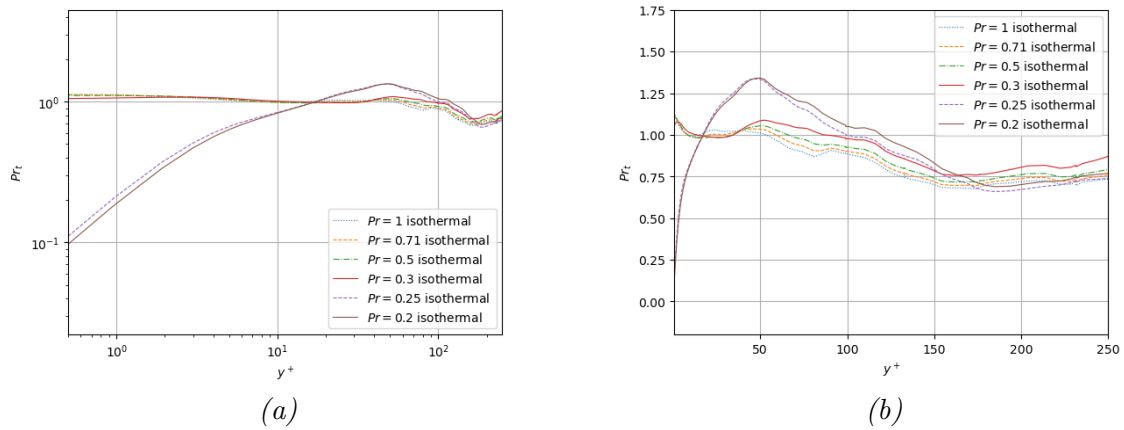


Figure 6.1: Turbulent Pr with isothermal wall-boundary conditions at $Re_\theta = 596$ across a wide range of Prandtl numbers: (a) logarithmic scale, (b) linear scale

Future work on this topic should focus on further exploring the effects of varying Prandtl numbers within this critical range on scalar transport mechanisms. Investigations could include a detailed analysis of the transition behavior and the underlying physical processes driving the change in the turbulent Prandtl number and detailed studies of interactions between molecular diffusion and turbulent transport in both inner and outer regions of the boundary layer. Understanding these interactions will be crucial for developing more accurate models and improving heat transfer predictions.

Appendix A

Accelerator Driven System

The appendix provides an in-depth overview of advantages of ADS. Accelerator Driven Systems (ADS) are innovative nuclear reactors that utilize a particle accelerator to produce a high-energy proton beam, that strikes a heavy metal target, such as lead or bismuth, generating neutrons through a process called spallation.

A.1 Main Process

The main process of an Accelerator Driven System (ADS) begins with the acceleration of protons using a linear accelerator (linac) to achieve high energies, typically in the range of 1-2 GeV. These high-energy protons are then directed towards a heavy metal target, such as lead or bismuth, where they induce a spallation reaction, producing a large number of neutrons. The number of neutrons produced can be estimated using the spallation yield formula:

$$Y = \frac{N_n}{N_p}$$

where Y is the neutron yield, N_n is the number of neutrons produced, and N_p is the number of protons incident on the target (see Pitcher et al. [63]).

These neutrons subsequently enter the sub-critical reactor core, which contains nuclear fuel like thorium or uranium, meaning the multiplication factor k is less than 1. The neutron population in the reactor, a simplified form, can be described by the neutron multiplication equation:

$$N(t) = N_0 e^{(k-1)t/\Lambda}$$

where $N(t)$ is the neutron population at time t , N_0 is the initial neutron population, k is the multiplication factor, and Λ is the neutron generation time. Within the core, the neutrons induce fission reactions in the fuel, generating heat. This heat is transferred to a coolant, which could be a liquid metal or molten salt, and is then used to produce electricity through conventional steam turbines. This process ensures that the reactor remains sub-critical, relying on the external neutron source to sustain the fission reactions, thereby enhancing the safety and control of the system.

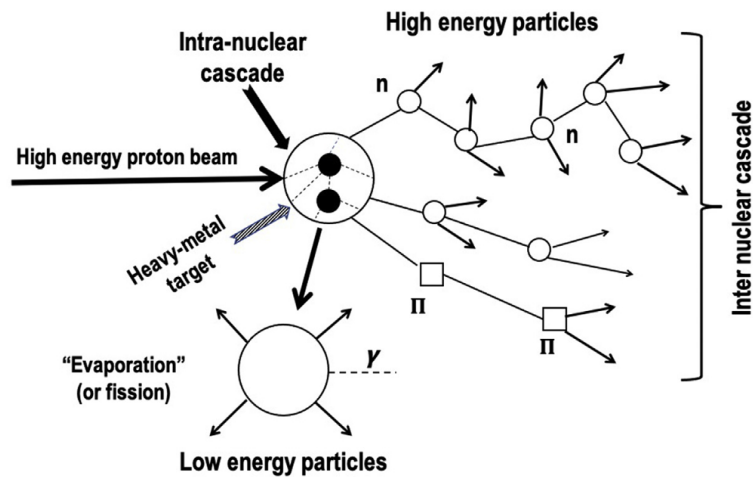


Figure A.1: Schematics of a two-stage spallation reaction from Gnanasekaran [3]

A.1.1 Advantages of ADS

- Enhanced Safety: The subcritical operation of ADS significantly reduces the risk of runaway reactions. The reactor can be quickly and safely shut down by stopping the proton beam.
- Waste Management: ADS can transmute long-lived radioactive waste into shorter-lived isotopes, reducing the long-term radiotoxicity and volume of nuclear waste.

Nuclear Waste Management

To sustainably exploit nuclear energy, managing radioactive waste from the fuel cycle is crucial. High-level nuclear waste (HLW) contains long-lived radioactive nuclides like minor actinides (Np, Am, Cm) and fission products (Cs-135, I-129, Tc-99). Current technology embeds these wastes in glass or ceramic matrices and stores them in monitored underground repositories. Typically, such waste requires over 10,000 years to reach safe radioactivity levels. However, if these nuclides are separated and treated individually, the monitoring period can be reduced to a few hundred years.

Transmutation in ADS

Transmuting minor actinides (MAs) into benign nuclides using high-energy neutrons in Accelerator-Driven Systems (ADS) is being explored. MAs can also be burned in Fast Breeder Reactors (FBRs). ADS is more versatile, capable of transmuting long-lived fission products. When high-energy particles (protons, deuterons, neutrons) with kinetic energies above 100 MeV hit a heavy metal target, spallation reactions occur. These particles, with very short de Broglie wavelengths, interact with individual nucleons in the target nucleus, causing intranuclear cascades that eject nucleons. If particle energy reaches GeV levels, the target nucleus may fragment. The excited nucleus then relaxes by "evaporating" nucleons, mainly neutrons, and may undergo fission in some heavy metal nuclides (see Gnanasekaran [3] and Pitcher et al. [63]).

A.1.2 Materials and Configurations

Candidate targets for Accelerator-Driven Systems (ADS) include mercury, liquid lead, lead-bismuth eutectic (LBE), tungsten, uranium, and tantalum. Liquid metals are preferred for high-power conditions due to their excellent heat transfer and reduced mechanical constraints. Mercury's low boiling point and high volatility pose challenges for confinement and use as a coolant. Lead's high melting point (327.5°C) is a disadvantage compared to LBE (125.5°C), which allows for a larger temperature difference across the core and target zone. However, LBE produces Po-210, a migratory alpha-emitter, which can form volatile polonium hydride upon exposure to moist air, raising safety concerns. Both liquid lead and LBE are highly corrosive to structural materials.

Two configurations for separating the proton beam and the heavy liquid metal target are considered: a metallic window and a windowless setup. The window configuration faces issues with cooling, thermal loading, radiation damage, and corrosion, necessitating frequent replacement. The windowless configuration must ensure compatibility between the heavy liquid metal and the beam transport vacuum to prevent degradation and migration of radioactive spallation products. LBE is currently the reference target material for ADS applications (see Gnanasekaran [3]).

Accelerator Driven Systems represent a promising technology for the future of nuclear energy, offering enhanced safety and waste management capabilities.

Appendix B

Liquid Metals in Nuclear Reactors

The appendix provides an in-depth overview of the liquid metals used in the simulation, detailing their key roles, nuclear reactions, and natural occurrence. At the end, it includes the relevant thermal and nuclear properties for the liquid metals.

B.1 Lithium

Lithium is found in various minerals, such as spodumene, lepidolite, and petalite, as well as in brine deposits. It has two stable isotopes, Li-6 and Li-7, with Li-6. Lithium-6 is used in nuclear reactors for radiation shielding and tritium production. It absorbs neutrons to form tritium, which is essential for fusion reactions. When Li-6 absorbs a neutron, it undergoes the following nuclear reaction:



This reaction produces tritium (${}^3\text{H}$), which then reacts with deuterium (${}^2\text{D}$) in a fusion reaction to release a significant amount of energy:



Lithium-7 is used as a coolant in high-temperature nuclear reactors due to its excellent thermodynamic properties, including a high boiling point (see Table 1.2) and low neutron absorption cross-section. Lithium-7 is involved in the following nuclear reaction for thermal neutron detection:



(see Oliviera [64]). An example of a reactor using lithium is the Princeton Plasma Physics Laboratory's fusion reactor.

B.2 Mercury

Mercury is found in the mineral cinnabar (HgS) and is a single-element liquid metal with the chemical symbol Hg. Due to its high thermal nuclear cross-section, mercury has limited potential as a primary coolant in thermal reactors. However, it was successfully used in the fast reactor Clementine (fueled by plutonium-239), where liquid

mercury was used to cool the reactor core. Mercury remains liquid at room temperature and does not react with water, making it a viable option as a secondary coolant (see Fleitman and Weeks [65]). Despite its historical use, mercury's disadvantages, including high vapor pressure and toxicity, limit its current applications in nuclear reactors.

B.3 Sodium

Sodium is abundant in nature, primarily found in the form of sodium chloride (NaCl) in seawater. Sodium is widely used as a coolant in fast breeder reactors due to its excellent thermal conductivity, high boiling point (see Table 1.2) and low neutron absorption cross-section. These properties make sodium an ideal coolant for maintaining high temperatures and efficient heat transfer in nuclear reactors. In fast breeder reactors ^{23}Na is the primary isotope used and it absorbs a neutron, it undergoes the following reaction:



Sodium-24 ^{24}Na is produced, which is radioactive and decays back to stable magnesium-24 ^{24}Mg . An example of a reactor using sodium is the BN-600 reactor in Russia.

B.4 Sodium-Potassium Alloy (Na-K)

Na-K is an alloy of sodium (Na) and potassium (K), typically in a eutectic mixture of 77% potassium and 23% sodium by weight. The sodium-potassium (Na-K) alloy is preferred over pure sodium in certain nuclear reactor applications due to its lower melting point (see Table 1.2), which simplifies the startup and operation of the reactor. However, the Na-K alloy also presents challenges, such as higher vapor pressure and significant chemical activity, which can lead to spontaneous ignition in air at moderate temperatures. Additionally, the formation of peroxide compounds of potassium in low-temperature zones can pose explosive risks. The presence of potassium in the alloy does not significantly alter the primary neutron capture reaction involving sodium, so it undergoes the same reaction as described previously. An example of a reactor using Na-K is the Experimental Breeder Reactor II (EBR-II) in the United States.

B.5 Lead

Lead is found in minerals such as galena (PbS) and is a single-element metal with the chemical symbol Pb. Lead is used as a coolant in some advanced nuclear reactors, particularly lead-cooled fast reactors (LFRs). Lead's high boiling point (see Table 1.2), excellent gamma radiation shielding properties and low reactivity, unlike Sodium, make it ideal for use in nuclear reactors. However, it is highly corrosive to structural materials, requiring careful management of oxygen levels and the use of protective coatings. In addition lead also serves as a neutron reflector, reducing neutron leakage and increasing the reactor's efficiency (see Sofu [66]). An example of a reactor using lead is the BREST-OD-300 reactor in Russia.

B.6 Lead-Bismuth Eutectic (LBE)

Lead-Bismuth Eutectic (LBE) is an alloy composed of 44.5% lead and 55.5% bismuth by weight, and it shares many properties with pure lead, such as a high boiling point and low neutron absorption. However, the presence of bismuth significantly enhances the alloy's performance as a nuclear reactor coolant. Bismuth lowers the melting point of the alloy (see Table 1.2), which simplifies reactor startup and operation by allowing the coolant to remain liquid at lower temperatures. LBE is used as a coolant and spallation target in accelerator-driven systems (ADS) and other advanced nuclear reactors. An example of a reactor using LBE is the MYRRHA reactor in Belgium.

B.7 Galinstan

Galinstan is a eutectic alloy composed of 68.5% gallium, 21.5% indium, and 10.0% tin by weight. It offers high thermal conductivity and low vapor pressure, similar to mercury, but is non-toxic and less reactive, enhancing safety. However, its use as a coolant in fission-based nuclear reactors is limited due to the high neutron absorption cross-section of indium, which effectively captures thermal neutrons and inhibits the fission process. Conversely, its potential as a coolant for fusion reactors is being explored, because of its low melting point and high thermal conductivity (see Table 1.2). An example of its use is in experimental setups at the Princeton Plasma Physics Laboratory.

Appendix C

Additional Proofs and Demonstrations

In this appendix, supplementary demonstrations are presented that provide further insights and detailed proofs not included in the main chapters. These additional materials are intended to support the understanding of the concepts and enhance the validity of the results.

C.1 Efficiency of Power-of-Two Polynomials in SEM

The spectral element method (SEM) leverages high-degree polynomials to achieve high accuracy and computational efficiency. When using Gauss-Lobatto-Legendre (GLL) points, the integration and differentiation operations become particularly efficient with polynomials of degree 2^n . This efficiency can be attributed to several factors. First, higher-order polynomials generally provide better approximations with fewer elements, leading to faster simulations. Modern computer architectures are optimized for operations involving powers of two, which results in more efficient memory access patterns and faster computations. This is particularly beneficial when performing matrix operations, such as the construction and inversion of mass and stiffness matrices. The GLL quadrature rule is well-suited for polynomials of degree 2^n , as the integration over an element is accomplished using the GLL points, resulting in a diagonal mass matrix. This diagonalization simplifies the algorithm and reduces computational cost because it allows the use of explicit time integration schemes without the need to invert a linear system.

The mass matrix \mathbf{M} and stiffness matrix \mathbf{K} in SEM can be expressed as:

$$\mathbf{M}_{ij} = \int_{\Omega} \phi_i(\mathbf{x})\phi_j(\mathbf{x}) d\Omega \quad (\text{C.1})$$

$$\mathbf{K}_{ij} = \int_{\Omega} \nabla\phi_i(\mathbf{x}) \cdot \nabla\phi_j(\mathbf{x}) d\Omega \quad (\text{C.2})$$

where $\phi_i(\mathbf{x})$ are the Lagrange interpolants at the GLL points. For polynomials of degree 2^n , the matrices \mathbf{M} and \mathbf{K} exhibit sparsity patterns that simplify their construction and inversion. Additionally, the error in SEM decreases exponentially

with the polynomial degree p . For a polynomial of degree 2^n , the error ϵ can be approximated as:

$$\epsilon \approx C \left(\frac{1}{2^n} \right)^p \tag{C.3}$$

where C is a constant. This exponential convergence allows for high accuracy with fewer elements, leading to faster simulations. In addition, SEM demonstrates spectral accuracy with an increasing number of grid points, making it an attractive method for simulating large-scale problems and particularly suitable for Direct Numerical Simulation (see Cheng et al. [67]).

Bibliography

- [1] Hamid Ait Abderrahim. “Realization of a new large research infrastructure in Belgium: MYRRHA contribution for closing the nuclear fuel cycle making nuclear energy sustainable”. In: *EPJ Web of Conferences* 246 (Jan. 1, 2020), p. 00012. DOI: [10.1051/epjconf/202024600012](https://doi.org/10.1051/epjconf/202024600012).
- [2] Peter Baeten et al. “MYRRHA: A multipurpose nuclear research facility”. English. In: *EPJ Web of Conferences*. Vol. 79. Publisher Copyright: © Owned by the authors, published by EDP Sciences, 2014.; 2013 - 3rd European Energy Conference, E2C 2013 ; Conference date: 27-10-2013 Through 30-10-2013. Dec. 2014. DOI: [10.1051/epjconf/20137903001](https://doi.org/10.1051/epjconf/20137903001).
- [3] T. Gnanasekaran. “1 - Thermophysical and nuclear properties of liquid metal coolants”. In: *Science and Technology of Liquid Metal Coolants in Nuclear Engineering*. Ed. by T. Gnanasekaran. Woodhead Publishing Series in Energy. Woodhead Publishing, Jan. 1, 2022, pp. 1–101. ISBN: 978-0-323-95145-6. DOI: [10.1016/B978-0-323-95145-6.00003-2](https://doi.org/10.1016/B978-0-323-95145-6.00003-2). URL: <https://www.sciencedirect.com/science/article/pii/B9780323951456000032>.
- [4] Richard W. Johnson et al. *Processes and Procedures for Application of CFD to Nuclear Reactor Safety Analysis*. INL/EXT-06-11789, 911721. Sept. 1, 2006, INL/EXT-06-11789, 911721. DOI: [10.2172/911721](https://doi.org/10.2172/911721). URL: <http://www.osti.gov/servlets/purl/911721-4eKKx1/>.
- [5] Christopher Boyd. *Computational Fluid Dynamics for Nuclear Systems*.
- [6] Osborne Reynolds. “An Experimental Investigation of the Circumstances Which Determine Whether the Motion of Water Shall Be Direct or Sinuous, and of the Law of Resistance in Parallel Channels”. In: *Philosophical Transactions of the Royal Society of London* 17 (1883), pp. 935–982. URL: <http://www.jstor.org/stable/109431>.
- [7] Ludwig Prandtl. “Über Flüssigkeitsbewegung bei sehr kleiner Reibung” (“On the Motion of Fluids with Very Little Viscosity”). In: *Verhandlungen des III. Internationalen Mathematiker-Kongresses*. Presented at the Third International Mathematical Congress. Heidelberg, 1904. URL: <https://ntrs.nasa.gov/citations/19930090813>.
- [8] Paul A. Libby. *An Introduction to Turbulence*. London: Taylor & Francis, 1996.
- [9] S. Tavoularis and S. Corrsin. “Experiments in nearly homogeneous turbulent shear flow with a uniform mean temperature gradient”. In: *J. Fluid Mech.* 104 (1981), pp. 311–367.

- [10] Z. Warhaft and J. L. Lumley. “An experimental study of the decay of temperature fluctuations in grid-generated turbulence”. In: *J. Fluid Mech.* 88 (1978), pp. 659–685.
- [11] M. Hishida and Y. Nagano. “Structure of turbulent velocity and temperature fluctuations in fully developed pipe flow”. In: *ASME J. Heat Transfer* 101 (1979), pp. 15–22.
- [12] Y. Zhu and R. A. Antonia. “Temperature dissipation measurements in a fully developed turbulent channel flow”. In: *Exps. Fluids* 15.3 (1993), pp. 191–199.
- [13] A. Mosyak, E. Pogrebnyak, and G. Hetsroni. “Effect of constant heat flux boundary condition on wall temperature fluctuations”. In: *ASME J. Heat Transfer* 123.2 (2001), pp. 213–218.
- [14] P. H. Hoffmann and A. E. Perry. “The development of turbulent thermal layers on flat plates”. In: *Int. J. Heat Mass Transfer* 22.1 (1979), pp. 39–46.
- [15] Y. Iritani, N. Kasagi, and M. Hirata. “Heat transfer mechanism and associated turbulence structure in a near wall region of a turbulent boundary layer”. In: *Turbulent Shear Flows 4*. Ed. by L. J. S. Bradburry et al. Springer-Verlag, 1985, pp. 223–234.
- [16] F. Anselmet, H. Djeridi, and L. Fulachier. “Joint statistics of a passive scalar and its dissipation in turbulent flows”. In: *J. Fluid Mech.* 280 (1994), pp. 173–197.
- [17] Iztok Tiselj, Cédric Flageul, and Jure Oder. “Direct Numerical Simulation and Wall-Resolved Large Eddy Simulation in Nuclear Thermal Hydraulics”. In: *Nuclear Technology* (2019), pp. 1–15. DOI: [10.1080/00295450.2019.1614381](https://doi.org/10.1080/00295450.2019.1614381). URL: <https://hal.science/hal-02154872>.
- [18] Pierre Sagaut. *Large Eddy Simulation for Incompressible Flows*. Reference SESAME book. Berlin: Springer, 2006.
- [19] H. Kawamura et al. “DNS of turbulent heat transfer in channel flow with low to medium-high prandtl number fluid”. In: *Int. J. Heat Fluid Flow* 19.5 (1998), pp. 482–491.
- [20] Y. Na and T. J. Hanratty. “Limiting behavior of turbulent scalar transport close to a wall”. In: *Int. J. Heat Mass Transfer* 43.10 (2000), pp. 1749–1758.
- [21] M. Rogers, P. Moin, and W. Reynolds. *The structure and modeling of the hydrodynamic and passive scalar fields in homogeneous turbulent shear flow*. Tech. rep. TF-25. Stanford University, 1986.
- [22] J. Kim and P. Moin. “Transport of passive scalars in a turbulent channel flow”. In: *Turbulent Shear Flows 6*. Ed. by J.-C. André et al. Springer-Verlag, 1989, pp. 85–96.
- [23] S. L. Lyons and T. J. Hanratty. “Direct numerical simulation of passive heat transfer in a turbulent channel flow”. In: *Int. J. Heat Mass Transfer* 34.4–5 (1991), pp. 1149–1161.
- [24] N. Kasagi, Y. Tomita, and A. Kuroda. “Direct numerical simulation of passive scalar field in a turbulent channel flow”. In: *ASME J. Heat Transfer* 114 (1992), pp. 598–606.

- [25] H. Abe, H. Kawamura, and Y. Matsuo. “Surface heat-flux fluctuations in a turbulent channel flow up to $Re = 1024$ with $Pr = 0.025$ and 0.71 ”. In: *Int. J. Heat Fluid Flow* 25.3 (2004), pp. 404–419.
- [26] S. Y. Chung and H. J. Sung. “Direct numerical simulation of turbulent concentric annular pipe flow. Part 2: Heat transfer”. In: *Int. J. Heat Fluid Flow* 24.3 (2003), pp. 399–411.
- [27] H. Kong, H. Choi, and J. S. Lee. “Direct numerical simulation of turbulent thermal boundary layers”. In: *Phys. Fluids* 12.10 (2000), pp. 2555–2568.
- [28] Qiang Li et al. “DNS of a spatially developing turbulent boundary layer with passive scalar transport”. In: *International Journal of Heat and Fluid Flow*. The 3rd International Conference on Heat Transfer and Fluid Flow in Microscale 30.5 (Oct. 1, 2009), pp. 916–929. ISSN: 0142-727X. DOI: [10.1016/j.ijheatfluidflow.2009.06.007](https://doi.org/10.1016/j.ijheatfluidflow.2009.06.007).
- [29] Hiroyuki Abe. “Direct numerical simulation of a turbulent boundary layer with separation and reattachment over a range of Reynolds numbers”. In: *Fluid Dynamics Research* 51.1 (Jan. 2019). Publisher: IOP Publishing, p. 011409. ISSN: 1873-7005. DOI: [10.1088/1873-7005/aac5fc](https://doi.org/10.1088/1873-7005/aac5fc). URL: <https://dx.doi.org/10.1088/1873-7005/aac5fc> (visited on 02/09/2025).
- [30] Jason Appelbaum, Markus Kloker, and Christoph Wenzel. “Buoyancy effects in an unstably stratified turbulent boundary layer flow”. In: *Theoretical and Computational Fluid Dynamics* 39 (2024), p. 10. DOI: [10.1007/s00162-024-00729-7](https://doi.org/10.1007/s00162-024-00729-7).
- [31] Aadhy Parthasarathy and Theresa Saxton-Fox. “A family of adverse pressure gradient turbulent boundary layers with upstream favourable pressure gradients”. In: *Journal of Fluid Mechanics* 966 (2023), A11. DOI: [10.1017/jfm.2023.429](https://doi.org/10.1017/jfm.2023.429).
- [32] Saurabh Pargal et al. “Adverse-pressure-gradient turbulent boundary layer on convex wall”. In: *Physics of Fluids* 34 (2022), p. 035107. DOI: [10.1063/5.0083919](https://doi.org/10.1063/5.0083919).
- [33] Guillermo Araya and Luciano Castillo. “DNS of turbulent thermal boundary layers up to $Re=2300$ ”. In: *International Journal of Heat and Mass Transfer* 55.15 (2012), pp. 4003–4019. ISSN: 0017-9310. DOI: <https://doi.org/10.1016/j.ijheatmasstransfer.2012.03.038>. URL: <https://www.sciencedirect.com/science/article/pii/S0017931012001871>.
- [34] Sergio Pirozzoli et al. “DNS of passive scalars in turbulent pipe flow”. In: *Journal of Fluid Mechanics* 940 (2022), A45. DOI: [10.1017/jfm.2022.265](https://doi.org/10.1017/jfm.2022.265).
- [35] Hoyas Alcántara-Ávila and Pérez-Quiles. “Large-scale channel flow DNS with passive scalars using CHF forcing”. In: *Journal of Fluid Mechanics* 965 (2021), A7. DOI: [10.1017/jfm.2023.387](https://doi.org/10.1017/jfm.2023.387).
- [36] Philippe R. Spalart and Jonathan H. Watmuff. “Experimental and numerical study of a turbulent boundary layer with pressure gradients”. In: *Journal of Fluid Mechanics* 249 (1993), pp. 337–371. DOI: [10.1017/S002211209300120X](https://doi.org/10.1017/S002211209300120X).

- [37] F. P. Bertolotti, Th. Herbert, and P. R. Spalart. “Linear and nonlinear stability of the Blasius boundary layer”. In: *Journal of Fluid Mechanics* 242 (1992), pp. 441–474. DOI: [10.1017/S0022112092002453](https://doi.org/10.1017/S0022112092002453).
- [38] Mattias Chevalier et al. “SIMSON : A Pseudo-Spectral Solver for Incompressible Boundary Layer Flows”. In: 2007. URL: <https://api.semanticscholar.org/CorpusID:118144498>.
- [39] Philipp Schlatter and Ramis Örlü. “Turbulent boundary layers at moderate Reynolds numbers: inflow length and tripping effects”. In: *Journal of Fluid Mechanics* 710 (2012), pp. 5–34. DOI: [10.1017/jfm.2012.324](https://doi.org/10.1017/jfm.2012.324).
- [40] Thomas S. Lund, Xiaohua Wu, and Kyle D. Squires. “Generation of Turbulent Inflow Data for Spatially-Developing Boundary Layer Simulations”. In: *Journal of Computational Physics* 140.2 (1998), pp. 233–258. ISSN: 0021-9991. DOI: <https://doi.org/10.1006/jcph.1998.5882>. URL: <https://www.sciencedirect.com/science/article/pii/S002199919895882X>.
- [41] Hiroyuki Abe, Yasuhiro Mizobuchi, and Yuichi Matsuo. “S0506-2-5 DNS of a turbulent boundary layer using the rescaling-recycling method”. In: *The proceedings of the JSME annual meeting 2010.2* (Sept. 4, 2010), pp. 21–22. DOI: [10.1299/jsmemecjo.2010.2.0_21](https://doi.org/10.1299/jsmemecjo.2010.2.0_21).
- [42] Anirban Garai, Scott M. Murman, and Dirk Ekelschot. “A new recycling method to generate turbulent inflow profiles”. In: *AIAA Aviation 2019 Forum*. AIAA Aviation 2019 Forum. Dallas, Texas: American Institute of Aeronautics and Astronautics, June 17, 2019. ISBN: 978-1-62410-589-0. DOI: [10.2514/6.2019-3420](https://doi.org/10.2514/6.2019-3420). URL: <https://arc.aiaa.org/doi/10.2514/6.2019-3420>.
- [43] Philippe R. Spalart. “Direct numerical study of leading-edge contamination”. In: 1989. URL: <https://api.semanticscholar.org/CorpusID:117355631>.
- [44] S. Dong, G. E. Karniadakis, and C. Chrysosostomidis. “A robust and accurate outflow boundary condition for incompressible flow simulations on severely-truncated unbounded domains”. In: *Journal of Computational Physics* 261 (Mar. 15, 2014), pp. 83–105. ISSN: 0021-9991. DOI: [10.1016/j.jcp.2013.12.042](https://doi.org/10.1016/j.jcp.2013.12.042).
- [45] Kemal Hanjalić and Brian Launder. *Modelling Turbulence in Engineering and the Environment: Second-Moment Routes to Closure*. Cambridge: Cambridge University Press, 2011. DOI: [10.1017/CB09781139013314](https://doi.org/10.1017/CB09781139013314). URL: <https://www.cambridge.org/core/books/modelling-turbulence-in-engineering-and-the-environment/3F63FA3CC3DEC8F7F2921A6403CC6443>.
- [46] Stephen B. Pope. *Turbulent Flows*. Cambridge, UK: Cambridge University Press, 2000. ISBN: 9780521598866.
- [47] Adrian Bejan. *Convection Heat Transfer*. Fourth. Hoboken, NJ: John Wiley & Sons, 2013. ISBN: 9780470900376.
- [48] Tuncer Cebeci and Peter Bradshaw. *Physical and Computational Aspects of Convective Heat Transfer*. Springer Study Edition. Springer New York, NY, 1988. DOI: [10.1007/978-1-4612-3918-5](https://doi.org/10.1007/978-1-4612-3918-5).

- [49] J. C. R. Hunt. “A First Course in Turbulence. By H. TENNEKES and J. L. LUMLEY. M.I.T. Press, 1972”. In: *Journal of Fluid Mechanics* 58.4 (1973), pp. 816–819. DOI: [10.1017/S002211207321251X](https://doi.org/10.1017/S002211207321251X).
- [50] Iztok Tiselj et al. “DNS of Turbulent Heat Transfer in Channel Flow With Heat Conduction in the Solid Wall”. In: *Journal of Heat Transfer* 123.5 (Mar. 2001), pp. 849–857. ISSN: 0022-1481. DOI: [10.1115/1.1389060](https://doi.org/10.1115/1.1389060). eprint: https://asmedigitalcollection.asme.org/heattransfer/article-pdf/123/5/849/5733971/849_1.pdf. URL: <https://doi.org/10.1115/1.1389060>.
- [51] KTH-Nek5000. *KTH Framework for Nek5000*. Accessed: 2025-02-12. 2021. URL: https://github.com/KTH-Nek5000/KTH_Framework.
- [52] D. Massaro et al. “A comprehensive framework to enhance numerical simulations in the spectral-element code Nek5000”. In: *Computer Physics Communications* 302 (2024), p. 109249. DOI: [10.1016/j.cpc.2024.109249](https://doi.org/10.1016/j.cpc.2024.109249).
- [53] A. Perez et al. *Spectral Element Method and Discrete Operators*. Nek5000 Course 2021. 2021. URL: https://media.enccs.se/2021/08/Nek5000_hands_on_1.pdf.
- [54] Saumitra Vinay Joshi and Hamidreza Abedi. *Pn-Pn2 Methods for Incompressible Flows (I): Fractional-step versus LU-decomposition*. Nek5000 Course 2021. 2021. URL: https://media.enccs.se/2021/08/Nek5000_hands_on_2.pdf.
- [55] David Krantz, Masumeh Gholamisheeri, and Martin Karp. *Pn-Pn Formulation and its Implementation in Nek5000*. Nek5000 Course 2021. 2021. URL: https://media.enccs.se/2021/08/Nek5000_hands_on_3.pdf.
- [56] Philippe R. Spalart and Kyung-Soo Yang. “Numerical study of ribbon-induced transition in Blasius flow”. In: *Journal of Fluid Mechanics* 178 (1987), pp. 345–365. DOI: [10.1017/S0022112087001253](https://doi.org/10.1017/S0022112087001253).
- [57] P. E. Roach and D. H. Brierley. “The influence of a turbulent freestream on zero pressure gradient transitional boundary layer development, part I: Test cases T3A and T3B”. In: *Numerical Simulation of Unsteady Flows and Transition to Turbulence*. Cambridge University Press, 1992, pp. 319–347.
- [58] W. M. Kays and M. E. Crawford. *Convective Heat and Mass Transfer*. 3rd. McGraw-Hill, 1993.
- [59] K. E. Schoenherr. “Resistance of flat surfaces moving through a fluid”. In: *Soc. Nav. Archit. Mar. Eng.* 40 (1932), p. 279.
- [60] John L. Lumley and Gary R. Newman. “The return to isotropy of homogeneous turbulence”. In: *Journal of Fluid Mechanics* 82 (1977), pp. 161–178. DOI: [10.1017/S0022112077000585](https://doi.org/10.1017/S0022112077000585).
- [61] Milos Radojkovic Djordje Novkovic and Zoran Radojkovic. “Anisotropy analysis of turbulent swirl flow”. In: *FME Transactions* 42.1 (2014), pp. 19–26. DOI: [10.5937/fmet1401019R](https://doi.org/10.5937/fmet1401019R).
- [62] A. S. Monin and A. M. Yaglom. *Statistical Fluid Mechanics: Mechanics of Turbulence*. Vol. 1. MIT Press, 1971.

- [63] Eric Pitcher et al. “Accelerator and target technology for accelerator driven transmutation and energy production”. In: *DOE white paper on ADS 1* (Jan. 2010).
- [64] G. A. C. de et al. Oliviera. “Applications of lithium in nuclear energy”. In: (2017). URL: <https://inis.iaea.org/records/6cpps-qrs06>.
- [65] A. H. Fleitman and J. R. Weeks. “Mercury as a nuclear coolant”. In: *Nuclear Engineering and Design* 16.3 (1971), pp. 266–278. ISSN: 0029-5493. DOI: [https://doi.org/10.1016/0029-5493\(71\)90015-X](https://doi.org/10.1016/0029-5493(71)90015-X). URL: <https://www.sciencedirect.com/science/article/pii/002954937190015X>.
- [66] Tanju Sofu. *OVERVIEW OF LEAD-COOLED FAST REACTOR (LFR) TECHNOLOGY*. U.S. Nuclear Regulatory Commission. 2019.
- [67] Candong Cheng et al. “Spectral Element Method for the Schrödinger-Poisson System”. In: *Journal of Computational Electronics* 3 (2004), pp. 417–421. DOI: [10.1007/s10825-004-7088-z](https://doi.org/10.1007/s10825-004-7088-z). URL: <https://link.springer.com/article/10.1007/s10825-004-7088-z>.
- [68] A. Lundbladh et al. “An Efficient Spectral Method for Simulation of Incompressible Flow over a Flat Plate”. In: 1999. URL: <https://www.semanticscholar.org/paper/An-Efficient-Spectral-Method-for-Simulation-of-Flow-Lundbladh-Berlin/46ce9baeaa266e57c026ff7e525e2eac1388b57e>.
- [69] B. Weigand, J. R. Ferguson, and M. E. Crawford. “An extended Kays and Crawford turbulent Prandtl number model”. In: *International Journal of Heat and Mass Transfer* 40.17 (Oct. 1, 1997), pp. 4191–4196. ISSN: 0017-9310. DOI: [10.1016/S0017-9310\(97\)00084-7](https://doi.org/10.1016/S0017-9310(97)00084-7).
- [70] Claudio Canuto et al. *Spectral Methods: Fundamentals in Single Domains*. Scientific Computation. Berlin, Heidelberg: Springer, 2006. ISBN: 978-3-540-30725-9 978-3-540-30726-6. DOI: [10.1007/978-3-540-30726-6](https://doi.org/10.1007/978-3-540-30726-6). URL: <http://link.springer.com/10.1007/978-3-540-30726-6> (visited on 03/26/2025).
- [71] G. Khujadze and M. Oberlack. “DNS and scaling laws from new symmetry groups of ZPG turbulent boundary layer flow”. In: *Theoretical and Computational Fluid Dynamics* 18.5 (Nov. 1, 2004), pp. 391–411. ISSN: 1432-2250. DOI: [10.1007/s00162-004-0149-x](https://doi.org/10.1007/s00162-004-0149-x).
- [72] P. Moin and K. Mahesh. “Direct numerical simulation: A tool in turbulence research”. In: *Annu. Rev. Fluid Mech.* 30 (1998), pp. 539–578.
- [73] G. K. Batchelor. “Small-scale variation of convected quantities like temperature in turbulent fluid: Part 1. General discussion and the case of small conductivity”. In: *J. Fluid Mech.* 5 (1959), pp. 113–133.
- [74] Alexey Dragunov et al. “Investigation of Thermophysical and Nuclear Properties of Prospective Coolants for Generation-IV Nuclear Reactors”. In: vol. 4. July 2013. DOI: [10.1115/ICONE21-16020](https://doi.org/10.1115/ICONE21-16020).
- [75] International Atomic Energy Agency IAEA. *Comparative Assessment of Thermophysical and Thermohydraulic Characteristics of Lead, Lead-Bismuth and Sodium Coolants for Fast Reactors*. IAEA-TECDOC-1289. Vienna: IAEA, 2002. ISBN: 92-0-113602-1.

- [76] Cédric Flageul et al. “DNS of turbulent channel flow with conjugate heat transfer: Effect of thermal boundary conditions on the second moments and budgets”. In: *International Journal of Heat and Fluid Flow* 55 (2015). Special Issue devoted to the 10th Int. Symposium on Engineering Turbulence Modelling and Measurements (ETMM10) held in Marbella, Spain on September 17-19, 2014, pp. 34–44. ISSN: 0142-727X. DOI: <https://doi.org/10.1016/j.ijheatfluidflow.2015.07.009>. URL: <https://www.sciencedirect.com/science/article/pii/S0142727X15000910>.
- [77] Kristel C. Meza-Fajardo and Apostolos S. Papageorgiou. “The Spectral Element Method (SEM): Formulation and Implementation of the Method for Engineering Seismology Problems”. In: *14th World Conference on Earthquake Engineering* (2014). URL: https://www.iitk.ac.in/nicee/wcee/article/14_03-03-0003.PDF.